Dissertation

submitted to the

Combined Faculties of the Natural Sciences and Mathematics

of Heidelberg University, Germany

for the degree of

Doctor of Natural Sciences

put forward by

Maitreyi Sangal

born in New Delhi, India

Oral examination: February 10th, 2021

The interaction of Light with Matter and Light with Light

Referees: **Hon. Prof. Dr. Christoph H. Keitel**

Prof. Dr. Jan M. Pawlowski

Zusammenfassung

Diese Arbeit besteht aus zwei Forschungsfeldern, die die Wechselwirkung von Licht mit Materie und Licht mit Licht beinhalten. Der erste Teil untersucht die Wechselwirkung eines superintensiven Laserpulses mit einer ultradünnen Folie mit der Dichte eines Festkörpers. Der vom Laserpuls ausgeübte Strahlungsdruck kann so stark sein, dass prinzipiell die gesamte Folie beschleunigt wird. Dies führt zur Erzeugung von dichten, kollimierten und quasimonoenergetischen Ionenstrahlen mit hoher Flussdichte. Das Einsetzen von transversalen Instabilitäten beschädigt jedoch die Folie, was zu einer ionenspektralen Verbreiterung führt. Die einfache analytische Modellierung wird durch Particle-in-Cell-Simulationen (PIC) unterstützt, um Methoden zur Unterdrückung der Instabilität und zur Verbesserung der Ionenstrahlqualität strategisch zu planen. Im zweiten Teil wird eine Methode zur Detektion des rein quantenelektrodynamischen Prozesses der elastischen Streuung realer Photonen im Vakuum vorgestellt. Monte-Carlo-Simulationen werden verwendet, um die Durchführbarkeit der Detektion dieses bislang unentdeckten Prozesses zu untersuchen. Es wird ein Versuchsaufbau verwendet, der aus einem hochenergetischen Gammastrahl besteht, der mit einem extrem ultravioletten Puls (XUV) oder einem Freie-Elektronen-Laser (FEL) kollidiert. Dieser saubere und kontrollierbare Aufbau nutzt die hohen Gammaphotonenenergien und den großen Laserphotonenfluss, um die Wahrscheinlichkeit von Streuereignissen zu erhöhen.

Abstract

This work consists of two fields of study involving the interaction of light with matter and light with light. The first part explores the interaction of a superintense laser pulse with an ultrathin solid density foil. The radiation pressure exerted by the laser pulse can be so strong that, in principle, the whole foil is accelerated. This results in the generation of dense, high-flux and collimated and quasimonoenergetic ion beams. However, the onset of transverse instabilities damages the foil, thus resulting in ion spectral broadening. Simple analytical modeling is supported by particle-in-cell (PIC) simulations to strategize methods for instability suppression and ion-beam quality improvement. The second part puts forward a method for detecting the purely quantum electrodynamic process of elastic scattering of real photons in vacuum. Monte-Carlo simulations are used to study the feasibility of detection of this yet undetected process. An experimental setup comprising of a high energy gamma-ray beam colliding with an extreme ultraviolet (XUV) pulse or a free-electron laser (FEL) is utilized. This clean and controllable setup exploits the high gamma photon energies and large laser photon flux for enhancing the probability of scattering events.

Within the framework of this thesis, the following articles were submitted for publication in refereed journals:

- Maitreyi Sangal and Matteo Tamburini
  High-Energy and High-Quality Ion beams in Light Sail Acceleration,
  submitted (2020), arXiv:2002.11563.

- Maitreyi Sangal, Christoph H. Keitel, and Matteo Tamburini
  Observing Light-by-Light Scattering in Vacuum with an Asymmetric Photon Collider,
  to be submitted.

Contents

1 Introduction

This thesis comprises of a set of two fields of study, "light" being quintessential in both. Simply put, the interaction of light with matter in the first part, and the interaction of light with light in the second. On account of the "dual nature" of this work, the following introduction, as well as this thesis will focus separately on each part.

1.1 Evolution of the LASER

The popular saying "Necessity is the mother of all invention" holds true to a very large extent for most of the advancements made by humankind. However, this did not seem to be the case when the LASER (Light Amplification by Stimulated Emission of Radiation) was initially invented. It was more of a discovery, waiting to find its necessities so to say. Owing to the multitude of applications and progress in fundamental research in present times, which would not have been possible without the laser first being developed 60 years ago, it is befitting to give a brief account of the evolution of lasers over time. Moreover, it will be an integral part of both the works presented in this thesis.

Max Planck's work on the blackbody radiation spectrum [1] and the introduction of the quantum hypothesis in 1900, followed by Albert Einstein's work on the photoelectric effect : the fact that light delivers its energy to a material in discrete packets (light quanta; now known as photons) in 1905 [2], paved the way for Albert Einstein to propose the concept of stimulated emission of radiation, in 1917 [3]. This sparked off a series of research work dedicated to the realisation of this concept in practice. Stimulated emission was first observed in 1928 by Rudolf Walther Ladenburg [4], however it came into practical use with the conception and development of the MASER (Microwave Amplification by Stimulated Emission of Radiation) by Charles Townes in 1951 [5, 6]. Townes and Schawlow later proposed the optical maser for higher frequencies in 1958 [7], and it was around this time that the term "LASER" was coined. The first operational LASER was finally developed by Theodore Maiman in 1960 [8]. Soon enough, with further development in the field of lasers, they found application in myriad fields ranging from communications, military purposes, surgical practices, probing matter for fundamental research, to mention a few.

A growing interest in using lasers in the context of nuclear fusion (inertial confinement fusion) in the 1970s posed the need for producing lasers with higher peak power. This was

made possible with the development of CO_2 lasers and glass lasers [9–13]. However, the rising intensities and correspondingly shorter pulses were detrimental for the gain medium, or suffered spectral and temporal pulse distortion while propagating through a medium. This problem was overcome only in the late 1980s, with the chirped pulse amplification technique (CPA), developed by D. Strickland and G. Morou [14], wherein a laser pulse is temporally stretched (chirped) by passing it through a dispersive medium (such as diffraction gratings) such that different frequency components in the pulse travel different path lengths. Higher frequency components of the pulse traveling greater lengths or being delayed imply a positive chirp, or a negative chirp if the lower frequency components are delayed. This way the pulse is stretched temporally, thereby reducing the peak power, and is later amplified and compressed, to achieve pulses of high intensity and ultra-short durations. Hence, using the CPA technique, great progress was made in the direction of generating ultra-short pulses ($\sim$ 10 fs) with higher peak powers ($\sim$ TW-PW), using Kerr lens mode locked [15], Ti:Sapphire ($TiAl_2O_3$) tunable lasers [16], which usually operate at a central wavelength of 0.8 μm. Achieving peak intensities of the order of 10^{14} - 10^{15} W/cm^2 opened up the avenue to explore non-linear laser-matter interaction such as high-harmonic generation (HHG), and later with even higher peak intensities $\gtrsim 10^{18}$ W/cm^2, the possibility of laser-driven electron and ion acceleration.

Realising the extraordinary potential of lasers, their evolution in this direction has been almost linear with time. Lasers today play a crucial role in the exploration of newer regimes of laser-matter or laser-plasma interaction, as alternative table-top sources of energetic particles (particle accelerators), for recreating and studying astrophysical conditions in the lab (laboratory astrophysics), generating high-harmonics, in laser spectroscopy, ultrafast imaging, medical applications such as ion beam therapy, and generation of radioactive isotopes for for medical purposes, among several others. Till date the research towards the development of lasers and its applications continues to thrive. With the currently available laser systems across the world [17], such as ELI [18], Apollon [19], XCELS [20], Vulcan [21], ATLAS [22], HERCULES [23], it is possible to achieve intensities of the order of $\sim 10^{22}$ W/cm^2 with the potential of reaching even two orders of magnitude higher intensity, with peak powers up to 10 PW, and pulse durations down to tens of femtoseconds (fs) [24].

1.2 Light-Matter interaction : Lasers as particle accelerators

When an intense laser impinges on matter, the least massive charged particles or the ones with the highest charge to mass ratio, namely the electrons, are the first ones to respond. Therefore, one important parameter which governs the regime of laser-matter interaction is the normalised peak amplitude of the laser defined as $a_0 = |e|E_0/m_e\omega c$, which is essentially the work done by the laser field on the electron over one laser wavelength. Here, e is the electron charge, E_0 is the magnitude of the peak field amplitude, m_e is the electron rest mass, $\omega = 2\pi c/\lambda$ is the laser angular frequency of a laser with peak wavelength λ and c is the speed of light in vacuum. This parameter can also be written in terms of the laser peak intensity I_0 and wavelength as $a_0 = 0.85\sqrt{I_0[\lambda^2/(1\mu m^2)]/10^{18}\mathrm{Wcm}^{-2}}$ for a linearly polarised laser pulse. The value of $a_0 \sim 1$ (corresponding to a peak intensity of $I_0 \sim 10^{18}$ W/cm^2 for a ~ 1 μm laser) is the threshold above which relativistic effects become important, and the magnetic field contribution to the Lorentz force experienced by an electron becomes comparable to the electric one, thus introducing significant non-linearities in the electron's dynamics. Thus, a_0 is also known as the classical non-linearity parameter.

Given that the response of electrons to a laser field govern the dynamics of the interaction, coupled with the fact that even for intensities $I_0 \sim 10^{14}$ W/cm^2 the laser field becomes strong enough to distort the Coulomb potential felt by an electron in an atom, thus leading to ionization, the study of the behaviour of single atoms and single electrons in a strong electromagnetic (EM) plane wave field in vacuum, forms the basis of further investigation of laser-matter interaction. At intensities around $I_0 \sim 10^{14}$ W/cm^2, an atom can be ionized by multiphoton processes such as Multi-Photon Ionization or (MPI) or Above Threshold Ionization (ATI), wherein an electron in an atom can absorb more than 1 photon energy in order to just overcome its binding potential or can absorb more than the required number of photons for it to be released in vacuum with a significant energy gain, respectively. Besides this, there could also be field ionization, wherein the field strength of the EM wave can distort the Coulomb barrier, thereby allowing the electron to tunnel through the barrier (Tunnel Ionization), or spontaneously exit in the case of Barrier Suppression Ionization (BSI) if the barrier height is suppressed even below the binding energy of the electron [25, 26].

Moreover, the behaviour of a single electron to an EM plane wave in vacuum is a well known result. In this case, the electron drifts along the laser propagation direction in the LAB frame or performs a figure-of-eight trajectory in its average rest frame with each oscillation period for a linearly polarised wave (or a helical trajectory in the laboratory

frame, and a circular one in its rest frame for a circularly polarised wave). The average drift and its transverse displacement from the propagation axis depends on the value of a_0. Even though there is a net displacement of the electron from its initial position, with each oscillation period, the electron comes back to rest, however large be the value of a_0 [25, 27]. This is the well-known result of the Lawson-Woodward Theorem [28, 29], that an electron cannot gain energy from a plane EM wave in vacuum.

However, if a realistic laser pulse is taken into consideration, then several of the underlying assumptions of this theorem can be violated, thus the possibility of accelerating the electron using a laser emerges. For instance, this could be possible if the laser is tightly focussed, thereby violating the assumption of a transversally infinite interaction region. Additionally, the ponderomotive force of the laser defined as $\mathbf{f_p} = -e^2\nabla\langle\mathbf{E}^2\rangle/2m_e\omega^2$ [27], also cannot be neglected in this case. Accelerating electrons in a plasma would imply a violation of several assumptions of the above theorem, because of the presence of more surrounding charged particles, and the generation of quasi-static electric or magnetic fields.

Consequently, over the years, several vacuum-based and plasma-based electron acceleration schemes have been studied theoretically and experimentally [30, 31]. Some of the vacuum-based electron acceleration schemes comprise of Vacuum Beat Wave Acceleration (VBWA) [32], using sub-cycle ($\sim$ 5fs) crossed beams to enhance the energy gained by an electron [33], phase-matched acceleration [34], oblique injection in a tightly focussed laser [35], etc. In particular, plasma-based acceleration schemes have been of great interest since a plasma can support very high field gradients ($\sim$ several GV/m). As already mentioned, for such high laser intensities, matter is ionized by the laser, thus forming a plasma. Now, depending on the characteristics of the laser pulse such as its peak intensity and pulse duration, and also the properties of target plasma, the laser energy can be coupled to the plasma electrons by various absorption mechanisms.

Now, a plasma can be broadly categorised in terms of the plasma electron number density n_e as underdense or overdense. This decides the characteristic response time of the plasma electrons or the frequency of electron oscillations, namely the electron plasma frequency $\omega_{pe} = \sqrt{4\pi n_e e^2/m_e}$. Another important parameter which is related to the laser frequency is the critical electron number density $n_c = m_e\omega^2/4\pi e^2 = 1.1 \times 10^{21} cm^{-3}(\lambda/1\mu m)^{-2}$, and this decides the point upto which a laser can penetrate into the plasma (i.e., when $n_e = n_c$ or $\omega = \omega_{pe}$). The plasma would therefore be underdense, if the laser frequency is greater than the plasma frequency ($\omega > \omega_{pe}$), meaning the laser can propagate through the plasma, or overdense if $\omega < \omega_{pe}$, meaning that the laser is reflected within a region of the order of the skin depth ($l_s = c/\omega_{pe}$) of the plasma. In the case of an underdense plasma, as the laser propagates through the target, electrons are

displaced in the forward direction due to the ponderomotive force of the laser at the rising edge of the pulse, leaving behind the ions, thereby creating a charge separation field. The electrons are again pulled back at the falling edge of the pulse, as the ponderomotive force changes its sign, thereby plasma oscillations are triggered in the wake of the pulse. If the electrons are in phase with the wave, then they can "ride" the wave, thus gaining energy. This idea was first proposed by Tajima and Dawson in 1979 [36], by exciting a wake of plasma waves, using two pulses with slightly different frequencies, known as Beat Wave Acceleration (BWA), which later led to several studies on wakefield generation and Laser Wakefield Acceleration (LWFA) schemes [30, 31].

On the other hand, in the case of an overdense plasma, or laser interaction with solid targets, numerous electron heating mechanisms have been studied. In general, the pulse can penetrate the skin layer, and the electrons in this layer are displaced forward due to the ponderomotive push. These can travel beyond the skin layer, thus transporting energy through the target. Depending on the laser intensity and plasma properties, different methods of energy absorption become prominent. For instance, for non-relativistic intensities and for relatively long pulses ($\sim$ ns or ps), collisional absorption mechanisms such as inverse bremsstrahlung or resonance absorption are dominant. Whereas, for relativistic intensities, collisionless absorption mechanisms are more dominant because the electron temperature is much higher in this case, and the electron-ion collision frequency scales as $T_e^{-3/2}$, where T_e is the electron temperature. For a plasma with very sharp density gradients or step-like profiles, Brunel heating, anomalous skin effect, or $\mathbf{j} \times \mathbf{B}$ heating due to the oscillating component of the ponderomotive force (in the case of linear polarisation), and several other absorption mechanisms come into play [25, 27, 37] .

Generation of hot electrons in the plasma leads to the formation of strong charge separation fields, which are in turn responsible for accelerating the slower responding ions. This makes laser-plasma based ion accelerators viable. Depending on how the laser energy is absorbed by the electrons, different ion acceleration mechanisms become dominant. Among the many ion-acceleration mechanisms that have been studied are target normal sheath acceleration (TNSA), which is also the most widely explored one both theoretically and experimentally. Here, the interaction of the laser is usually with a thick target (few μm), and electrons in the target front get pushed to the target rear and into vacuum due to the laser ponderomotive force, which leads to the formation of a strong electrostatic charge separation field or sheath field. This causes the ions in the target rear to be accelerated. This was first observed in 2000, in one of the experiments wherein protons with energies upto $\sim$ 60 MeV were produced [38]. However, the energy spectrum of the generated protons was very broad, thus making it unsuitable for several applications. Nonetheless, this sparked further interest in exploring other laser-driven ion

acceleration schemes.

Some other mechanisms that have been explored over the years are, radiation pressure dominant acceleration (RPDA) schemes like hole-boring (HB-RPA), which occurs mainly in thick targets ($\sim \mu m$). Here, the radiation pressure of the laser is the dominant acceleration mechanism and, as the name suggests, bores a hole through the target, such that the radiation pressure and electrostatic pressure in the frame of the dense plasma interface balance. The ions in the front side of the target keep getting cyclically accelerated in bunches, such that they catch up with the fast electrons. For thin targets ($\sim nm$) the light-sail (LS-RPA) mechanism becomes dominant. Here, the whole target is modeled as a rigid mirror, and can in principle, be accelerated as a whole. Infact, the strong ponderomotive push on the electrons, inturn causes almost all ions to be accelerated and co-move with the electrons, thus gaining much higher energies than the electrons, and almost the whole target then propagates ballistically. The energy scaling of RPDA is linear with intensity and is much more favourable than that of TNSA. Besides the above, there have been studies on numerous other ion acceleration schemes such as collisionless shock acceleration (CSA), relativistically induced transparency (RIT) causing breakout-after-burner (BOA), acceleration due to Coulomb explosion, and many more [37,39,40].

It is imperative to mention here that theory and experiments go hand-in-hand. Not only have all the above mentioned processes been theoretically modeled to provide deeper understanding of the fundamentals of laser-matter interaction, they have also served as explanations of experimental results, or as proposals for performing new experiments. Given the collective behaviour depicted by plasma, it is therefore important to also self-consistently simulate the complex dynamics of the interaction, in order to compare with theoretical models, improve them, and to perform more realistic computational experiments, before performing them in the laboratory. In this context, the Particle-in-Cell (PIC) method [41] for performing kinetic simulations has served as an integral numerical tool, and continues to be so, especially with advancements in computing power.

1.2.1 Light-Sail acceleration : Motivation

Of the above mentioned laser-driven ion acceleration mechanisms, the Light-Sail acceleration mechanism in the radiation pressure dominant (RPD) regime is very promising, owing to its predicted favourable energy scaling with the laser energy, and the possibility of whole-target acceleration, resulting in the production of dense, collimated, quasi-monoenergetic ion beams, that are of specific interest for medical applications such as ion beam therapy (IBT) [42,43]. Ion beam therapy has already proven to be of success for treating tumors. However, it is done only in a few facilities around the world with conventional accelerators. Laser-based ion beam generation to satisfy the requirements

for ion beam therapy, therefore receives considerable interest as it would make laser-based treatment facilities more feasible, cost-effective and accessible to people over the world.

The theoretical model for this mechanism was first given by Prof. G. Marx, as a method for using the radiation pressure of an Earth-based laser to propel an interstellar spacecraft [44]. Even though this has not been possible yet, there are some interesting missions dedicated to this end : LightSail2, which is a spacecraft that raises its orbit using the solar radiation pressure [45] and the Breakthrough Starshot initiative, whose aim is to provide proof of concept by propelling an ultra-light nano-spacecraft to Alpha Centauri using a ground-based laser system [46].

As a consequence of LS-RPA's salient features, detailed theoretical and computational studies have been dedicated towards predicting appropriate laser and target parameters for achieving ion-acceleration via this mechanism. One of the earliest studies proposed a threshold for the peak laser intensity of $I_0 \approx 10^{23}$ Wcm^{-2} for linearly polarised (LP) pulses [47] in order to access this regime. Thereafter, it was realised that the use of circularly polarised (CP) pulses helps reduce this intensity threshold as it suppresses excessive electron heating due to the absence of the oscillating component of the $\mathbf{j} \times \mathbf{B}$ force, [48]. Simulations also showed that radiation reaction (RR) effects are suppressed with the use of CP pulses, thus making CP pulses more favourable [49, 50]. Further important results comprised of a limiting condition for maintaining target opacity ($a_0 \lesssim \zeta$, where $\zeta = \pi n_e \ell / n_c \lambda_l$ is the areal density of the target, n_e is the electron number density, n_c is the critical density for the laser wavelength λ). An optimal target thickness of $a_0 \sim \zeta$ in order to achieve maximal ion energy for a constant intensity [51], and several other pulse-tailoring and target engineering techniques [52, 53].

Despite a significant advancement in the understanding of this mechanism, achieving ions accelerated via LS-RPA as predicted, has proved to be difficult in practice. This is not only due to non-ideal factors like finite laser spot size, laser spatial intensity profile and low temporal pulse contrast ratio, but also significantly due to the triggering of transverse surface instabilities during the laser-foil interaction, that are detrimental to the spectral quality of the target ions. These instabilities manifest as density fluctuations or ripples in the target, that grow during the interaction, thus rendering the target transparent to the laser. Several instability mechanisms have been proposed to be responsible for the formation of these ripples such as Weibel-like instability, two-stream instability, and the Rayleigh-Taylor like surface instability (RTI). Studies showed that RTI is the dominant instability in this case. Here the laser pressure (light fluid) tries to support/push against a heavy fluid (target ions), thereby causing the interface between the two fluids (target surface) to become unstable. The growth rate of RTI is proportional to $\sqrt{ka}$, where k is the wavenumber of the instability and a is the acceleration. [54, 55]. This predicts that

the instability grows fastest for larger wavenumbers (or shorter wavelengths). However, theoretical and simulation studies, and experiments also found that the instability wavelength is limited to be of the order of the laser wavelength ($\lambda_{RT} \sim \lambda$) due to diffraction effects, thus making instability modes of the order of laser wavelength to be the dominant ones [56–59].

Although several ideas have been proposed to overcome the limitations to the ion spectral quality, such as using flattop transverse laser pulse profiles [60], shaped targets [61] to overcome finite spot-size effects, confinement of the laser pulse by the plasma cocoon formed during laser-target interaction [62], using multi-species and double-layered (DL) targets [63–65], high-Z nanofoils as electron charging stations (ECS) for electron replenishment [66], using targets with pre-imposed transverse modulations [67,68], and pulses with a sharp intensity rise [55], the improvements in the ion spectra are yet not as satisfactory as envisioned. Infact, it is observed that these surface instabilities are inevitable even using a laser pulse of infinite width (plane wave) and a flat foil [52,67,69].

Our motivation is thus, to propose optimal conditions to achieve LS-RPA, while being able to mitigate the detrimental effects of transverse instabilities. We show that a connection exists between the attainable average ion energy per nucleon, and the development of the transverse Rayleigh-Taylor like instability, and support analytical modeling with high-resolution 1D and 2D PIC simulations using the SMILEI PIC code [70,71]. We investigate pulse and target tailoring techniques, that would help improve the quality of ion beams via this mechanism. In particular, we demonstrate that substantial improvements of the quasi-monoenergetic features of the ion spectrum are possible either by employing a train of short and intense laser pulses on a thin foil, or by using a single short and intense laser pulse impinging on a double-layered foil. In addition, we discuss realistically achievable laser and target parameters, which are within the reach of currently available laser and target manufacturing technology.

1.3 Light-Light interaction

Till now, we focused on the interaction of light with matter. But what about the interaction of light with light itself? Ponderings about this question can be traced back to the 17th century. The proponents of the wave nature of light like Johannes Kepler [72,73] and Christiaan Huygens [74] observed the property of light to be such that the superposition principle holds true; that when light waves come from different directions they do not cause any hindrance to each other and produce their effect independently of the other. In the opposite case however, for people who supported the corpuscular or particle nature of light, it seemed that collisions between light corpuscles must be observed, which would

arise as a violation of the superposition principle.

In the 1800s however, with the mathematical formulation of electromagnetic phenomena by James Clerk Maxwell, the wave theory and the validity of the superposition principle, as a consequence of the linearity of Maxwell's equations seemed to be the formal explanation for Kepler's and Huygen's observations. However, again in the beginning of the 1900s, the quantum theory came into being after Max Planck's and Albert Einstein's seminal work, which brought about the concept of photons : corpuscles of light. This, once again brought back the need to understand how photons would interact with photons. Several attempts to formalise and understand this process and the idea of violation of the superposition principle were made thereafter, starting from K. N Shaposhnikov [75], Louis De Broglie, Leon Rosenfeld and E. Witmer [76].

It was only in 1933, that Otto Halpern [77] suggested the possible physical mechanism behind the photon-photon scattering process ($\gamma\gamma \rightarrow \gamma\gamma$) in vacuum based on Dirac's hole theory [78], i.e. a photon could fluctuate into a virtual electron-positron pair which would then annihilate. This pointed towards the presence nonlinear electrodynamical phenomena. Thereafter, in 1935 Euler and Kockel, and later Euler and Heisenberg [79, 80] calculated the leading order nonlinear corrections to Maxwell's equations in vacuum, and thus introduced the Euler-Heisenberg Lagrangian density which depends on the electromagnetic field via the two field invariants given by $\mathcal{F} = (\mathbf{E}^2 - \mathbf{B}^2)/2$ and $\mathcal{G} = \mathbf{E} \cdot \mathbf{B}$. This indicated that the presence of background electromagnetic fields in vacuum, would make the vacuum behave as a polarizable medium with a refractive index other than 1. Note that this would not be the case for a single monochromatic plane wave, however strong, because here, both the field invariants vanish, and hence no nonlinear corrections would apply. This would imply alterations to the propagation of light in the presence strong background electromagnetic fields in vacuum. Photon-photon scattering is hence connected to vacuum polarisation effects.

Euler and Kockel also calculated the photon-photon scattering cross-section in the low energy limit ($\omega_{cm} \ll m_e$, where ω_{cm} is the energy of one of the incident photons in the center-of-momentum (CoM) frame) [79, 80]. They found that the cross-section for this process is $\sigma \propto \omega_{cm}^6$, and gave an upper bound for it to be $\sim 10^{-30}$ cm^2. Later Akheizer calculated the photon-photon scattering cross-section in the high energy limit ($\omega_{cm} \gg m_e$) [81], where the cross-section is $\sigma \propto \omega_{cm}^{-2}$. The full cross-section was finally calculated by Karplus and Neuman in 1951 [82, 83], and later also by B. De Tollis and Beretetskii, Lifshitz, Pitaevskii [84–86]. The upper bound of the cross-section as mentioned is extremely low, with a discontinuity at the CoM energy equal to the electron rest mass energy above which it becomes possible to produce real pairs. This extremely low value of the probability of this process, is the main reason for it not being detected

till today. Even before QED was formalised, several attempts were made to observe this effect experimentally primarily in three directions : (i) direct detection of the scattering of photons with photons in vacuum, (ii) attempts consisting of identifying changes in the propagation of photons under the influence of external constant electric or magnetic fields, (iii) some based on astronomical observations [87]. One of the first attempt was already made in 1928 by S.I. Vavilov [88], where he used the radiation from electric sparks, in order to reach high enough radiation densities, to be able to observe the collision of photons. Thereafter, in 1930s a method to detect this process using higher energy photon like X-rays or gamma rays was proposed by A.K Das [89], which was a significant realisation at the time due to the fact that the cross-section for this process is much lower for the visible spectrum. Around this time, some experiments were performed by C.Farr and C.J Banwell [90] to study the effect of a transverse magnetic field in vacuum on the propagation of light. But the magnetic field they could produce in the laboratory was $\sim$ 1 T. Besides, J. Stark made attempts to observe this effect in the presence of a strong electric field. However, this too was also several orders of magnitude smaller, than the now well-known QED critical field strength $E_{cr} = m_e^2 c^3/\hbar|e| \sim 1.3 \times 10^{16}$ V/cm [91], where $\hbar$ is the reduced Planck's constant. Several other efforts in a similar direction in the years following shortly also resulted in no detection of the occurrence of this process [87].

Before proceeding further, it is important to mention another invariant parameter : the quantum non-linearity parameter given as $\chi = \sqrt{-(F_{\mu\nu}k^\nu)^2}/m_e c E_{cr}$ where $F_{\mu\nu}$ is the field tensor k^ν is the photon 4-momentum of the incoming photon. Thus, $\chi \gtrsim 1$ implies non-linear QED effects or the non-perturbative regime which for instance would happen if the photon energies are very high, or if the background fields are of the order of the critical QED field E_{cr}. In this case, the Euler-Heisenberg Lagrangian will not be applicable, and also in the low energy region, the vacuum polarisation effects would not be very prominent. This is also one reason as to why the experiments performed in the past observed no result, as the fields used were significantly smaller than the critical field.

Recently, with progress in laser development and accelerator technology, it became possible to produce high energy photon beams in the laboratory, and also laser intensities $I_0 \sim 10^{23}$ W/cm^2, providing much stronger fields (however, still lower than the critical field). Thus, several other experiments aimed at detection were proposed, most of which correspond to the low photon energy regime, however some also in the high energy or non-perturbative regime. Some proposals using high energy (GeV) γ beams at the Photon Linear Collider (PLC) [92] and SLAC [93] were made in the late 1900s. Over the last two decades, there have been several proposals: using a laser assisted setup consisting of three lasers, two with the same wavelength and a third assisting laser with a different

wavelength [94, 95] in a way that the number of scattering events can be enhanced. Another innovative idea was to perform a "matterless double-slit" experiment, wherein two super-intense parallel laser beams ($\sim 10^{24}$ W/cm^2) counter-propagate with respect to another lower intensity probe beam, which in the course of interacting with one of the strong beams, should get scattered to form an interference pattern [96]. Another suggestion was to impinge a probe beam on a series of several intense parallel beams ($\sim 10^{23}$ W/cm^2), which would enhance the scattering process, if the incidence angle satisfies the Bragg condition [97]. Additionally, some experiments were also proposed to measure changes in the polarisation of an incoming probe beam in the presence of intense laser fields [98–100]. Also, there have been even studies on the possibility of enhancing vacuum polarisation effects in a plasma [101]. An experiment in 2013 and later again in 2016 had been performed to detect this process in the X-ray region using the X-ray Free-Electron laser at SACLA, however no signal was observed in either case [102, 103]. A recent proposal and feasibility study to detect this process using a $\gamma - \gamma$ collider based on the design of the Beijing Electron Positron Collider (BEPC) has also been reported in 2018 [104]. These are just few of the wide variety of proposals made and experiments performed. [105, 106].Furthermore, in the high energy region, other vacuum polarisation effects have been studied and even observed such as Delbrück scattering, where an energetic photon is scattered in the Coulomb field of a nucleus [107–109], and the photon-splitting process [110, 111].

Infact, recently, evidence for the elastic scattering of two virtual photons has been obtained at an experiment at ATLAS detector at the Large Hadron Collider (LHC). This consisted of colliding two lead nuclei (Pb + Pb). When such highly charged (Z = 82) ions collide, then if the impact parameter is greater than the diameter of a nucleus, such an event is termed as ultra-peripheral collision (UPC). In this case, the strong force does not dominate, and the electromagnetic field of the respective nuclei can be approximated as a beam of equivalent virtual photons (equivalent photon approximation). Herein, the flux of these photons is very high because it scales as Z^2. These virtual photons then can lead to the $\gamma\gamma \to \gamma\gamma$ process [112–114]. However, these measurements pertain to an indirect evidence of photon-photon scattering, and the elastic scattering of two real photons has yet not been detected.

Furthermore, in the case when the energy in CoM of the incident photons exceeds the pair production threshold, another process involving the collisions of two photons is possible, i.e. the linear Breit-Wheeler pair creation ($\gamma\gamma \to e^+e^-$) [115], where two high energy photons collide to form an electron-positron pair, with its cross-section several orders of magnitude higher than the elastic photon-photon scattering cross-section. Infact, this is another process that has evaded detection till today. However, the non-linear Breit-

Wheeler pair creation ($\gamma + n\hbar\omega_l \rightarrow e^+e^-$), where 1 high energy photon absorbs many low energy photons from a strong optical laser field, has been observed in the E-144 experiment at SLAC, wherein a 46.6 GeV electron beam and an intense laser beam produced $\sim$ 30 GeV γ photons which in turn interacted with the laser photons to produce pairs via the non-linear or multiphoton Breit-Wheeler process [116, 117]. Several proposals have been made thereafter for detection of the linear Breit-Wheeler process too, observation of this process is not so easy because of the presence of other pair-production processes such as the Trident and Bethe-Heitler pair-production that have even higher cross-sections. Some of the recent proposals aimed to this end have been the interaction of a bremsstrahlung based GeV photon beam with thermal X-rays generated in a vacuum hohlraum [118], using two identical MeV sources produced in the interaction of an intense laser with thin metal targets by various mechanisms such as bremsstrahlung, Compton scattering, synchrotron radiation [119]. However, a clear signature of this process is still missing.

Presently, not only do several sources of high energy photons exist in synchrotron facilities, Compton based sources or free-electron lasers (FELs) with energies ranging upto several MeV [120–123], but there have also been many ingenious ideas proposed for sources with higher photon energies, high photon flux, and increased efficiency. These ideas range from using laser-plasma [124–129], laser-electron beam interaction [130–133], QED cascades produced in the collision of two counter-propagating intense laser pulses [131, 134], plasma instabilities in electron beam-plasma interaction such as filamentation [135], beamstrahlung in beam-beam collisions [136–138] and colliding an ultra-relativistic electron beam with multiple thin (sub-μm) conducting foils [139], to name a few. Moreover, several high-harmonic sources have also been demonstrated using laser-based high-harmonic generation in gases or plasmas, which can produce coherent radiation in the extreme ultraviolet (XUV) region, with a high repetition rate [26, 140–147].

The multitude of available high photon energy sources, in addition to the fact that the elastic scattering of two real photons yet remains to be detected, paves the way to the realisation of photon-photon scattering experiments. We hence, propose an experiment utilising a γ beam with energies ranging up to a few GeV interacting with either a high-harmonic source of radiation or a free-electron laser, all of which are not only practically achievable today, but also have the added advantage of having one source of monoenergetic photons which is tunable and controllable, and is also scalable to fit the requirements for being in the optimal region for detection. This would ensure two things : (i) that the parameters can be carefully chosen such that the energy in the CoM frame of the incoming photons approaches $m_e c^2$, implying an increase in the cross-section of the process, while remaining below the threshold for pair-production such that no other competing processes are present, (ii) the probability of large angle scattering is significant.

To this end, we perform Monte-Carlo simulations with a γ beam and a high-harmonic laser, wherein the γ beam is generated in the interaction of an ultra-relativistic electron beam and an intense laser via nonlinear or linear Compton backscattering. The electron beam parameters are based on those available in accelerator facilities like FACET II [148] and DESY [149]. The γ beam generation is implemented computationally by my supervisor Dr. Matteo Tamburini, which is then input in the Monte-Carlo code, where the full cross-section for the photon-photon scattering process has been included. The spatio-temporal structure of the Gaussian beam fields for the laser have also been implemented in this code, by following the calculation of Y. Salamin [150, 151], which is based on the method of K.T. McDonald [152].

The structure of this thesis is as follows : Chapter 2 contains sections on essential background concepts for laser-plasma interaction, such as the PIC simulation method, a discussion on ion acceleration mechanisms in the radiation pressure dominant regime, with a focus on the light-sail ion acceleration regime. Optimal conditions for obtaining ion beams with enhanced spectral qualtiy will be discussed and supported by multi-dimensional Particle-in-Cell simulations. Chapter 3 contain background sections on the photon-photon scattering cross-section calculations, the modeling of the electromagnetic fields of a Gaussian laser beam beyond the paraxial approximation. These sections will be followed by a description of the structure and implementation of the Monte-Carlo code, along with our estimates and some results. Chapter 4 summarises the work done in the above two fields and provide an outlook for further work.

2 Towards High Energy and High Quality ion beams in the Light-Sail Regime

2.1 Introduction

When a super-intense laser pulse ($\sim I_0 \gtrsim 10^{18}$ W/cm^2) illuminates an ultra-thin ($\sim$ few nm) solid-density foil, the entire foil can in principle be accelerated as whole due to the radiation pressure of the laser pulse. This envisages the possibility to produce dense ion beams with a quasi-monochromatic energy spectrum and a high degree of collimation. Because of these features, radiation pressure acceleration in the light-sail regime (LS-RPA) is a very promising acceleration mechanism, most favourable for applications where dense and monoenergetic beams are needed. However, laser-driven ion beams with such features are yet to be obtained in practice. One major obstacle in obtaining such beams is the occurrence of several instabilities, which deforms the target, thus resulting in a premature termination of the acceleration stage. Here we discuss ways for suppressing the detrimental effects of these instabilities with proper matching of the laser pulse and foil parameters, such that dense, high quality ion beams having a low energy spread and low angular divergence can be produced. We support analytical modeling with high-resolution Particle-in-Cell (PIC) simulations.

This Chapter contains sections which will provide the basic background information necessary as a starting point for our investigations, which will be followed by sections containing our obtained results. The structure is as follows. Section 2.2 will briefly highlight basic properties of a plasma along with the modeling of plasmas under the kinetic description. This will lead to the next Section 2.3 where a basic idea about the Particle-in-Cell method, a powerful numerical tool to simulate the dynamics of plasmas, will be given. Section 2.4 will briefly describe the conditions when radiation pressure is dominant, following which the theoretical models of two ion acceleration mechanisms in the radiation pressure dominant regime, namely hole-boring in Section 2.5 and light-sail in Section 2.6 will be discussed. Under this last section 2.6.1 will contain our inferences and predictions based on the 1D model. Section 2.7 will give an overview of transverse instabilities, with a main focus on the Rayleigh-Taylor-like intability, after which in Section 2.7.1 our further predictions to be used as starting points for our results

will be indicated. Finally, all sections under Section 2.8 will provide our results, and conclusions thereafter. Some parts in Sections 2.6 & 2.7, and major parts in Section 2.8 appear exactly as in our submitted article which was jointly written by M. Tamburini and me [153].

2.2 Basic Plasma properties and Plasma modeling

It was mentioned in Chapter 1 that when an intense laser $\sim 10^{14}$ W/cm^2 impinges on matter, the matter is ionized thereby forming a plasma. It is hence important to define when "ionized matter" can be called a plasma. A plasma comprises of charged and neutral particles which as a whole exhibits the characteristic properties of *collective behaviour* and *quasineutrality* [154, 155].

- Collective behaviour : Consider any two charged particles in a plasma. These would interact with each other via their Coulomb potential, which falls off as the inverse squared of the distance between them ($\propto 1/r^2$). However, now consider, two charged regions in the plasma separated by a distance r. In this case, even though the Coulomb force between these two regions falls off as $\propto 1/r^2$, the volume of one charged region that can affect the other increases as $\propto r^3$. This leads to the long range Coulomb interaction in a plasma, i.e. different volume elements of charge can "*collectively*" interact with other charged particle collections.

- Quasineutrality : This can be understood via the concept of Debye shielding. Due to the collective interaction, the Coulomb field of any "test" charged particle would cause all its nearby charged particles to move and try to neutralise or shield out the field of this charge. The distance over which this electric field is screened is known as the Debye length which is defined as :

$$\lambda_D = \frac{k_B T_e}{4\pi n_e e^2} \tag{2.1}$$

  The above Eq. 2.1 is defined by considering the more massive and slower responding ions to be immobile. The thermal electron motion is responsible for the shielding process. Hence in general, the electron temperature T_e is used to define this shielding length and the ions can be considered as "cold". On a length scale L much larger than the Debye length λ_D ($L \gg \lambda_D$), the bulk of the plasma can therefore be considered as "*quasineutral*", meaning $n_e = Zn_i$, where n_e is the electron number density, n_i is the ion number density of a species with atomic number Z for a fully ionized plasma.

For the above to be valid, the plasma number density must be high such that λ_D is small compared to the plasma scale length L. Moreover, the number of particles in a sphere of radius λ_D, given by $N_D = n_e \lambda_D^3$ must also be very large ($N_D \gg 1$) [154].

Now, because of the above characteristics of a plasma, charged particle motion results in generation of electric and magnetic fields, which in turn affects the motion of these particles. Thus it becomes important to describe the evolution of the system in a self-consistent manner. Based on the properties of a plasma, such as the electron temperature T_e, plasma density n_e, and also on the time scale of the phenomena of interest, a fluid or kinetic description of a plasma is used. The fluid description of a plasma is sufficient under the assumption that particles suffer frequent collisions such that they achieve thermal equilibrium and have a Maxwellian distribution. Under this assumption, the velocity distribution of a species of charged particles can then just be described in terms of its temperature. However, in most cases, this is not valid. For instance, high temperature or low density plasmas are collisionless, and the particles are not in thermal equilibrium. In this case, a fluid picture does not reveal all the information about the system. A kinetic description is more appropriate, wherein the velocity distribution of each charged species is also needed to correctly describe the behaviour [154]. This is especially required in the context of high intensity and short pulse laser-matter interactions.

The kinetic behaviour of a collisionless plasma is therefore described by the Vlasov-Maxwell system of equations which is the most widely used approach and is the starting point for simulations. The distribution function of a given charged particle species s in the plasma is $f_s(\mathbf{r}, \mathbf{p}, t)$ [71]. This is the number density of particles of charge q_s and mass m_s with momenta between $\mathbf{p} + d\mathbf{p}$ at a given position $\mathbf{r}$ and time t. Therefore, the charge and current densities $\rho(\mathbf{r}, t)$ and $\mathbf{J}(\mathbf{r}, t)$, respectively are given as

$$\rho(\mathbf{r}, t) = \sum_s q_s \int f_s(\mathbf{r}, \mathbf{p}, t) d^3p \tag{2.2a}$$

$$\mathbf{J}(\mathbf{r}, t) = \sum_s q_s \int \mathbf{v} f_s(\mathbf{r}, \mathbf{p}, t) d^3p \tag{2.2b}$$

The distribution function $f_s(\mathbf{r}, \mathbf{p}, t)$ satisfies the well known Vlasov equation, which is written in its relativistic form as

$$\frac{\partial f_s}{\partial t} + \frac{\mathbf{p}}{\gamma m_s} \cdot \frac{\partial f_s}{\partial \mathbf{r}} + \mathbf{F_L} \cdot \frac{\partial f_s}{\partial \mathbf{p}} = 0 \tag{2.3}$$

Here $\mathbf{F_L}$ is the Lorentz force experienced by the particles due to their collective electric

$\mathbf{E}(\mathbf{r},t)$ and magnetic fields $\mathbf{B}(\mathbf{r},t)$,

$$\mathbf{F_L} = q_s\left(\mathbf{E} + \frac{\mathbf{p}}{\gamma m_s} \times \mathbf{B}\right) \tag{2.4}$$

where $\gamma = \sqrt{1+\mathbf{p}^2/m_s^2c^2}$ is the relativistic factor. The self-generated electric and magnetic fields satisfy the Maxwell's equations :

$$\nabla \cdot \mathbf{E} = \frac{\rho}{\epsilon_0} \tag{2.5a}$$

$$\nabla \cdot \mathbf{B} = 0 \tag{2.5b}$$

$$\nabla \times \mathbf{E} = -\frac{\partial \mathbf{B}}{\partial t} \tag{2.5c}$$

$$\nabla \times \mathbf{B} = \mu_0\epsilon_0\frac{\partial \mathbf{E}}{\partial t} + \mu_0\mathbf{J} \tag{2.5d}$$

Thus, the electric and magnetic fields $\mathbf{E}(\mathbf{r},t)$ and $\mathbf{B}(\mathbf{r},t)$ are determined form Maxwell's equations Eqs. 2.5 by substituting the charge and current densities $\rho(\mathbf{r},t)$ and $\mathbf{J}(\mathbf{r},t)$ (Eq. 2.2). These fields then determine the Lorentz force in Eq. 2.4, which intern enters the Vlasov equation Eq. 2.3, thereby leading to a self-consistent description of the evolution of the plasma.

2.3 The Particle-in-Cell Method

The Vlasov-Maxwell kinetic description of a collisionless plasma described above is a very powerful model describing the plasma evolution. However, the distribution function $f_s(\mathbf{r},\mathbf{p},t)$ is dependent on seven independent variables. Therefore, integrating the Vlasov equation would require keeping track of the full six dimensional (6D) phase-space. Even in a reduced dimensionality, this proves to be a daunting task, and impractical to solve computationally [156, 157]. How is this issue then circumvented? This is where the Particle-in-Cell (PIC) method comes into play, which was proposed in the 1960s [41]. The idea is to decompose the distribution function into several finite-sized "pseudo-particles", each representing a large number of "real" particles on a discrete spatial grid. This is possible because of the collective behaviour of a plasma. Thus, such finite sized particles can be chosen such that each represents a large number of real particles in approximately one Debye sphere. Refer to Fig. 2.1 for a representation of this idea.

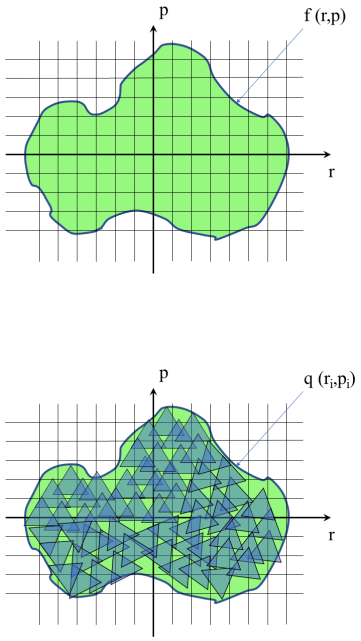

Figure 2.1: :Figure showing the relation between Vlasov (top) and PIC (bottom) codes. The figure is adapted from [156].

The discrete distribution function is represented as [71] :

$$f_s(\mathbf{r},\mathbf{p},t) = \sum_{j=1}^{N_s} w_j S(\mathbf{r}-\mathbf{r}_j(t))\delta(\mathbf{p}-\mathbf{p}_j(t)) \tag{2.6}$$

where w_j is the weight of each pseudo-particle (i.e. the number of real particles represented by a pseudo-particle), N_s is the total number of pseudo-particles for a given species s, $\mathbf{r}_j$ and $\mathbf{p}_j$ is the position and momentum of the j^{th} particle respectively, and $S(\mathbf{r})$ is the shape function describing the effective shape or spatial distribution of each pseudo-particle, δ is the Dirac distribution.

Now, substituting the discrete distribution function Eq. 2.6 in the Vlasov equation Eq. 2.3, multiplying by $\mathbf{p}$, and thereafter integrating over all momenta $\mathbf{p}$ and space $\mathbf{r}$, one finds that each pseudo-particle satisfies the the relativistic equation of motion [71]

$$\frac{d\mathbf{r_j}}{dt} = \frac{\mathbf{p}_j}{\gamma_j m_s} \tag{2.7a}$$

$$\frac{d\mathbf{p}_j}{dt} = q_s\left(\mathbf{E}_j + \frac{\mathbf{p}_j}{\gamma_j m_s}\times\mathbf{B}_j\right) \tag{2.7b}$$

Here the fields $\mathbf{E}_j$ and $\mathbf{B}_j$ at the position of each particle are then found by interpolating

the fields on the discrete spatial grid as

$$\mathbf{E}_j = \int S(\mathbf{r} - \mathbf{r}_j)\mathbf{E}(\mathbf{r})d\mathbf{r} \tag{2.8a}$$

$$\mathbf{B}_j = \int S(\mathbf{r} - \mathbf{r}_j)\mathbf{B}(\mathbf{r})d\mathbf{r} \tag{2.8b}$$

Thus, the problem effectively boils down to two coupled solving schemes in a standard PIC code : (i) Solve a discretised system of Maxwell's equations to obtain the fields. (ii) Use these fields to evolve the particles by solving their relativistic equation of motion. The basic PIC algorithm is the following :

- At t = 0, initialise the pseudo-particles on a discrete spatial grid by specifying their weights w_j, charge q_s, mass m_s, and initial distributions in phase-space.
- Evaluate the charge and current densities $\rho(\mathbf{r}, 0)$ and $\mathbf{J}(\mathbf{r}, 0)$ and project them onto the spatial grid.
- Solve Maxwell's equations to compute the fields $\mathbf{E}(\mathbf{r})$ and $\mathbf{B}(\mathbf{r})$ on the grid. This is typically done using the Finite-Difference-Time-Domain (FDTD) method where the electric and magnetic fields are discretised onto a Yee staggered grid [158].
- Interpolate fields at the positions of each particle to obtain $\mathbf{E}_j$ and $\mathbf{B}_j$.
- Now evolve the particles. This is typically done using the Boris particle pusher based on the leap-frog scheme [159].
- Compute the new fields and deposit the new charge and current densities on the grid.

Over the last few decades, several PIC codes have been developed, some of which are open-source. Moreover, they have been greatly improved in terms of the performance of the code, numerical stability and extra physics modules. In our work, we use the open-source, fully relativistic, high-performance (HPC) PIC code SMILEI [70, 71]. (For more details on the numerical schemes, physics packages and optimization, see paper).

2.4 Radiation Pressure Dominant Ion Acceleration Mechanism

Various laser-plasma based ion acceleration mechanisms were mentioned in Chapter 1, wherein the laser pulse and target parameters govern the dominance of one acceleration

mechanism over the other. The focus of this section is the Radiation Pressure Dominant Acceleration (RPDA) mechanism. In general, a plane electromagnetic (EM) wave, incident normally on the surface of a target with reflectivity R, absorptivity A and transmissivity T, can transfer its momentum to the target. The radiation pressure is thus, the amount of momentum delivered to the target per unit surface and time, and can be found using energy conservation (R + T + A = 1). For an opaque target (T = 0), the radiation pressure is given by the well known result [160]:

$$P_{\text{rad}} = (1 + R)\frac{I}{c} \tag{2.9}$$

For a perfectly reflecting target (R = 1, A = 0), $P_{\text{rad}} = 2I/c$, where I is the intensity of the EM wave and c is the speed of light in vacuum. In the context of a realistic laser pulse, the radiation pressure on the target is nothing but the integral of the ponderomotive force per unit volume $\mathbf{f}_p \equiv$ This force is responsible for the longitudinal displacement of the electrons away from the immobile ions in the target, along the laser propagation direction. This leads to the creation of a strong charge separation electrostatic field $\mathbf{E}_{\text{es}}$ between the ions and electrons. Infact, the ions having a slower response time, respond to this field and are accelerated. At the point when both the ponderomotive force and the electrostatic force per unit volume on electrons balances, i.e. when $\mathbf{f}_p = en_e\mathbf{E}_{\text{es}}$, the electrons are in mechanical equilibrium. Then under the condition of quasineutrality in a plasma $Zn_i = n_e$, the electrostatic force per unit volume on the ions would be $Zen_i\mathbf{E}_{\text{es}} = en_e\mathbf{E}_{\text{es}}$. Therefore, the total radiation pressure on the target P_{rad} is equal to the total electrostatic pressure P_{es}. This circumstance of pressure balance ($P_{\text{rad}} = P_{\text{es}}$) is when radiation pressure is said to be dominant, and P_{rad} can be considered to be responsible for accelerating the target ions. Hence, the name "Radiation Pressure Dominant Acceleration" [161].

Two ion acceleration schemes fall under this regime, the key distinguishing feature being the target thickness. The theoretical models that exist for these two mechanisms will be discussed briefly.

2.5 Hole-Boring (for *thick* targets ∼ few μm)

In the Hole-Boring (HB-RPA), the plasma target is modeled as an overdense semi-infinite slab with perfect reflectivity (R = 1). When a laser pulse is normally incident on the target, it penetrates upto the skin layer $l_s = c/\omega_{pe}$, and the laser ponderomotive force leads to the formation of a dense electron compression layer. This happens till the charge separation field E_{es} balances the ponderomotive force in the rest frame of the dense bending plasma surface. The laser pushes the plasma surface forward into the target, thereby

boring a hole. The velocity of the dense plasma surface is known as the hole-boring velocity v_{HB}. In its rest frame, the plasma surface would "see" ions coming towards it with a velocity $-v_{\mathrm{HB}}$, and under pressure balance conditions, these ions would bounce back from the target with velocity v_{HB}, therefore resulting in a velocity of $2v_{\mathrm{HB}}$ in the laboratory frame. For a constant intensity laser pulse, the hole-boring velocity can be estimated using the pressure balance condition in its rest frame as follows [162] :

$$P_{\mathrm{rad}} = P_{\mathrm{es}} \tag{2.10a}$$

$$\frac{2I}{c}\left(\frac{1-\beta_{\mathrm{HB}}}{1+\beta_{\mathrm{HB}}}\right) = (\gamma n_i)(\gamma m_i 2\beta_{\mathrm{HB}}^2 c^2) \tag{2.10b}$$

where $\beta_{\mathrm{HB}} = v_{\mathrm{HB}}/c$ is the hole-boring velocity in units of c, the ion number density n_i in surface rest frame is $\gamma_{\mathrm{HB}} n_i$, $\gamma = 1/\sqrt{1-\beta_{\mathrm{HB}}^2}$ being the Lorentz factor, and m_i is the ion mass.

Solving Eq. 2.10 for β_{HB} gives :

$$\beta_{\mathrm{HB}} = \frac{\sqrt{B}}{1+\sqrt{B}} \tag{2.11}$$

where $B = I/\rho c^3$ is the so-called dimensionless pistoning parameter, where $\rho = m_i n_i$. Thus the maximum energy gained by ions per nucleon in the lab frame is then given as :

$$\varepsilon_{\mathrm{max}} = m_u c^2 \left(\frac{2B}{1+2\sqrt{B}}\right) \tag{2.12}$$

where m_u is the atomic mass unit.

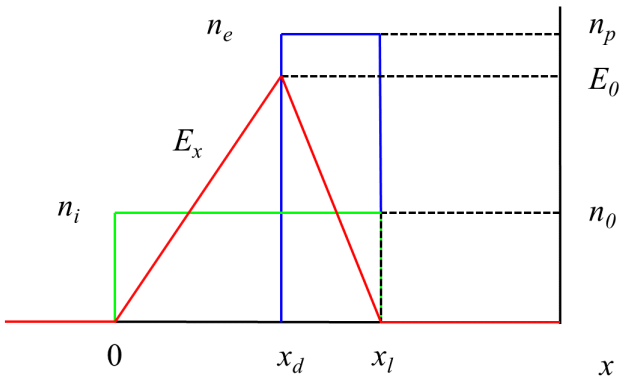

Figure 2.2: :Figure adapted from [163].The regions $x_d < x < x_l$ and $0 < x < x_d$ correspond to the density compression and charge depletion layer respectively. The figure depicts the initial stage of establishment of equilibrium where the electrostatic field E_x balances out the radiation pressure.

A more indepth understanding of the dynamics can be understood by the explanation provided in [27, 163]. According to this, at the initial stage, the laser penetrates upto the

skin layer causing electrons to pile up in a dense compression region which is of the order of the skin depth $l_s = c/\omega_{pe}$ until quasi-equilibrium condition is established ($P_{\rm rad} = P_{\rm es}$). Only the ions initially present within this compression region are accelerated with the lab frame velocity $2v_{\rm HB}$ and cross into the bulk of the plasma (refer to Fig. 2.2). The ions present in the region before the compression layer, which is the charge depletion layer, do not catch up with the ones in the compression layer, and are further accelerated as a second energetic bunch when quasi-equilibrium is re-established. Therefore, the hole-boring acceleration mechanism consists of a "cyclic acceleration" of several ion bunches, and results in a broad energy spectrum. From the above, it follows that the ion energy scales linearly with intensity $\propto B = I/\rho c^3$. Therefore, this regime is not very favourable for attaining relativistic ion energies. For very solid density targets with $n_e > 100 n_c$, where n_c is the critical plasma density, this would require very high intensities. However, this regime works well for lower density targets, and lighter ions such as protons. However, the energy spectrum obtained in this regime is quite broad, with a cutoff at $\varepsilon_{\rm max}$.

2.6 Light-Sail (for *thin* targets ∼ sub-μm or few nm)

The Light-Sail acceleration mechanism (LS-RPA) is dominant for thin targets. In this case, if the target thickness is of the order of the compression layer ($\ell \sim l_s$) that forms in the case of HB-RPA, then in principle the laser pulse bores through the whole target, i.e. LS-RPA is a special case of HB-RPA, wherein the hole-boring is complete even before the pulse ends, thereby accelerating almost all the ions to the same velocity. In this case, the plasma foil is modeled as a flat rigid 'mirror' (T = 0), with mass density $\rho = m_i n_i$ and thickness ℓ accelerated by the radiation pressure of an intense plane-wave-like laser pulse with frequency ω (see Fig. 2.3). For a laser pulse, normally incident on the foil, the equation of motion of the thin target (light sail) in the laboratory frame is given by ([47, 51, 164])

$$\frac{d}{dt}(\gamma\beta_{\rm LS}) = \frac{2I(t')}{\rho\ell c^2} R(\omega') \left(\frac{1-\beta_{\rm LS}}{1+\beta_{\rm LS}}\right), \tag{2.13}$$

where $\beta_{\rm LS} = v_{\rm LS}/c$ is the foil velocity in units of the speed of light in vacuum c, $\gamma = 1/\sqrt{(1-\beta_{\rm LS}^2)}$ is the relativistic factor of the foil, $I(t')$ is the laser intensity at the foil position as a function of the retarded time $t' = t - X(t)/c$, where $X(t)$ is the instantaneous foil position, and $R(\omega')$ is reflectivity of the foil as function of the laser frequency in the rest frame of the foil $\omega' = D\omega$, with $D = \sqrt{(1-\beta_{\rm LS})/(1+\beta_{\rm LS})}$ being the Doppler factor. Considering a constant intensity pulse and assuming perfect reflectivity $R(\omega') \approx 1$, the above equation can be solved analytically and in the asymptotic limit, the foil relativistic factor as a function of time is expressed in terms of the laser and target parameters as

$\gamma(t) \simeq (6It/\rho\ell c^2)^{1/3}$ [27].

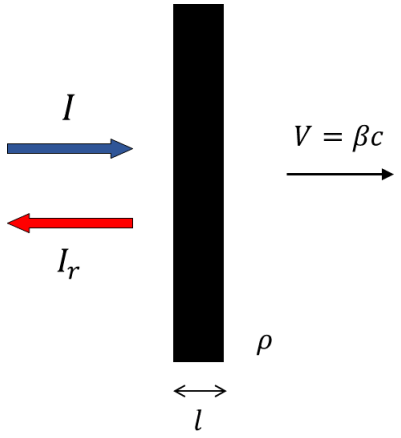

Figure 2.3: :Schematic of a rigid, opaque and thin slab being accelerated as a whole by the radiation pressure of the incident laser pulse. (adapted from [27].)

Moreover, by changing from time t to the retarded time t', Eq. (2.13) can be solved exactly for an arbitrary laser pulse temporal profile. The light-sail velocity β_{LS} and predicted energy per nucleon ε_u is then [51]

$$\beta_{\mathrm{LS}} = \frac{(1+\mathcal{E})^2 - 1}{(1+\mathcal{E})^2 + 1} \tag{2.14}$$

$$\varepsilon_u = \frac{\mathcal{E}^2}{2(1+\mathcal{E})} m_u c^2, \tag{2.15}$$

where m_u is the atomic mass unit and $\mathcal{E} = 2\mathcal{F}/\rho\ell c^2$ is essentially the ratio between the laser pulse fluence $\mathcal{F} = \int I(t')dt'$, i.e., the laser pulse energy per unit surface, and the foil surface density $\rho\ell$.

Eq. 2.15 implies that arbitrarily high ion energies can be obtained by increasing the laser pulse fluence. It should be noted that the simple LS model assumes perfect target reflectivity, and predicts a monoenergetic acceleration for the "whole" foil.

However, what would be the case when a realistic high-intensity pulse is incident on a thin target? The key point is that the above can be true only as long as the target maintains its reflectivity $R(\omega') \approx 1$. This can be clearly understood by using normalized units, i.e., by rewriting $\mathcal{E}$ as a function of the normalized laser field amplitude $a(\phi) = \sqrt{I(\phi)/I^*}$ and the normalized surface density $\zeta = \pi n_e \ell / n_c \lambda$, where $I^* = m_e^2\omega^2 c^3/4\pi e^2$, $\phi = [t/T - X(t)/\lambda]$ is the laser phase at the foil position, and $n_c = m_e\omega^2/4\pi e^2$ is the

critical plasma density. Here n_e is the electron number density, e and m_e are the electron charge and rest mass, while $T = 2\pi/\omega$ and $\lambda = cT$ are the laser period and wavelength, respectively. For simplicity, consider a foil with a single fully ionized atomic species, subject to a constant intensity laser pulse then $\mathcal{E}$ is written as

$$\mathcal{E} = \frac{2\pi Z m_e \int a^2(\phi)\, d\phi}{A m_u \zeta} = \frac{2\pi Z m_e a_0^2 \tau}{A m_u \zeta} \tag{2.16}$$

where Z (A) is the atomic number (mass), and a_0 is the peak value of $a(\phi)$. and τ the total pulse duration in units of the laser period. For the foil to be opaque to the laser, the most intuitive inference from Eq. 2.16 is that the laser peak amplitude must be less than the normalized foil surface density ($a_0 < \zeta$). This is true, however, 1D simulations pointed towards the presence of an optimal target thickness for which maximal energy gain is obtained in accordance with the LS equation, for a given ionized species with a fixed electron number density n_e [164]. The optimal thickness condition for this was found to be such that $a_0 \approx \zeta$ is satisfied. This led to a further improvement of the LS model by taking into account the effects of a foil with partial reflectivity (R < 1) [51]. Arising due to the oscillations of electrons in the foil at relativistic laser intensities ($a_0 > 1$), the expression for this non-linear reflectivity of the foil in its rest frame, is given within the thin foil approximation ($n_e \gg a_0 n_c$ and $\ell \ll \lambda$) as :

$$R(\omega') = \frac{1}{1 + \zeta'(\phi)^{-2}\Gamma^2(\phi)}, \tag{2.17}$$

where Γ is the 'transverse' relativistic factor associated with the transverse relativistic oscillations of the electrons in the foil and $\zeta'(\phi) = \zeta/D(\phi)$ is the Doppler increased normalized foil surface density [51].

$$\begin{aligned}\Gamma^2(\phi) =& \big\{1 + a^2(\phi) - \zeta'^2(\phi) + \big[(1 + a^2(\phi) - \zeta'^2(\phi))^2 \\ &+ 4\zeta'^2(\phi)\big]^{1/2}\big\}/2\end{aligned} \tag{2.18}$$

Now, the foil reflectivity $R(\omega')$ is approximately unity when $a(\phi) < \zeta'(\phi)$ [1] which is automatically satisfied when $a_0 \lesssim \zeta$ (see Ref. [51]). The above threshold condition means that $\Gamma \approx 1$ when $a_0 \ll \zeta$, implying a suppressed foil transmissivity, and $\Gamma \approx \sqrt{a_0}$ when $a_0 \approx \zeta \gg 1$ implying increased foil transmissivity. Thus the condition $a_0 \approx \zeta \gg 1$ sets a threshold for achieving maximal radiation pressure on the target and hence maximal energy gain for a given laser pulse intensity.

[1] Note that in the ultra-relativistic case the relation $a(\phi) < \zeta'(\phi)$ allows to increase the laser intensity or decrease the foil areal density maintaining $R \approx 1$, which, in principle, allows to attain ion energies well beyond those attainable with the bound $a_0 \lesssim \zeta$.

It is also important to restate here, that a circularly polarised pulse (CP) is more favourable for RPA dominance. This is attributed to the fact that for a CP pulse, the oscillating component of the $\mathbf{j} \times \mathbf{B}$ force is absent, thus suppressing the generation of hot electrons [48, 51–53, 162, 163]. Therefore, with the use of CP pulses, RPA can in principle be dominant at any laser intensity.

2.6.1 Model-based predictions 1D

The above model of LS-RPA thus brings us to a starting point for our 1D simulations, the results of which will be discussed in Section 2.8. In our investigation we use a laser pulse with a $\sin^2$ temporal envelope (i.e., $\sin^4$ temporal profile for intensity). Thus $\mathcal{E}$ in Eq. 2.16 is obtained as

$$\mathcal{E} = \frac{3\pi Z m_e a_0^2 \tau}{4 A m_u \zeta} \tag{2.19}$$

Now, employing the above mentioned threshold condition for optimal LS-RPA ($a_0 \approx \zeta$) in Eq. 2.16 leads to

$$\mathcal{E} = \frac{2\pi Z m_e a_0 \tau}{A m_u} \tag{2.20}$$

Since the ion energy per nucleon ε_u in LS-RPA scales as the laser pulse fluence $\mathcal{F} \propto a_0^2 \tau$, then for a fixed laser fluence, the above implies that reducing the laser intensity a_0 and correspondingly increasing the laser pulse duration τ ensures that target reflectivity is maintained. Moreover, this leads to a greater fraction of the target ions attaining the same energy, thereby improving the monoenergeticity of the spectrum. In addition, a lower laser intensity with longer laser pulse duration also results into (i) a more adiabatic foil acceleration, which maintains the plasma foil compact during the acceleration phase. (ii) a reduced foil heating and, consequently, a suppressed expansion of the foil driven by energetic electrons.

2.7 Instabilities

The above 1D models for RPA ion acceleration mechanisms have not only served as a starting point for investigation of each process by numerical simulations, but also provide a deeper understanding of the underlying dynamics of the acceleration mechanisms. Moreover, the model predictions have been in good agreement with simulation results.

However, in a more realistic multi-dimensional geometry, the scenario completely changes, which is why LS-RPA has been difficult to achieve in practice. One of the major issues is the onset of transverse instabilities that manifest as density perturbations in the plasma foil, which grow over time and eventually render the foil transparent to the laser. This

is highly undesirable for achieving the promising features of a dense monochromatic ion energy spectrum predicted by LS-RPA. Infact, this is observed even when plane-wave laser pulses and flat foils are employed (see in Section 2.8), such that finite size effects are absent.

The accelerated foil is subject to a number of instabilities such as Weibel-like instability [165], two-stream-like instability [166], and Rayleigh-Taylor-like (RT) instability [55, 56]. In the context of RPA with thin foils, the most widely explored instability is the Rayleigh-Taylor-like instability. This is on account of the fact that the target can be modeled as a compressible (heavy) fluid, which is pushed by the radiation pressure of the laser (the photons of the laser being the light fluid). The pressure difference on both sides of the foil thus causes the interface of these two 'fluids' to be unstable, just like what happens in the standard Rayleigh-Taylor instability [54]. In this case the instability grows as $\sqrt{2\pi a/\lambda_m}$ where a is the acceleration and λ_m is the perturbation mode wavelength. This predicts that the instability grows indefinitely for smaller wavelength modes.

Numerous theoretical instability analyses have been performed for obtaining the growth rate of the instability in laser-thin foil interaction. Some of these involve a linear stability analysis wherein the length scale of the transverse density modulations in the thin foil can be considered much larger than the laser wavelength and a constant pressure force can be assumed [55]. Additionally, further investigation has been done which takes into account also the finiteness of the laser wavelength and the fact that a realistic short laser pulse is not monochromatic [57]. This is responsible for scattering of the EM waves off the periodic density structures. This leads to a modification of the growth rate of the standard RT instability for $\lambda_m < \lambda$, however corresponds to the standard RT predictions where $\lambda_m \gtrsim \lambda$, with a dominant mode at $\lambda_m \sim \lambda$. Additionally, even a kinetic description of the plasma foil has been investigated, which takes into account the finite thickness of the foil [167], and suggests that the small scale perturbations $\lambda_m < \lambda$ arise due to transverse electron oscillations. [166].

However, relatively small perturbations $\lambda_m \ll \lambda$ tend to be 'smoothed' in the laser pulse-foil interaction, whereas longer wavelength modes $\lambda_m \gtrsim \lambda$ are amplified [56]. The linear theory of RT instability predicts that the shorter wavelength mode compatible with diffraction effects should dominate [55], which is indeed confirmed by experiments where $\lambda_m \sim \lambda$ was shown to be the dominant wavelength of density modulations [56]. Thus, the dominant $\lambda_m \sim \lambda$ mode of RT instability is a key quantity for assessing the importance of transverse effects. In its linear stage, the RT instability grows exponentially, with its exponent rising linearly with time in the non-relativistic regime. On the contrary, the RT exponent grows proportionally to the cubic root of time in the ultra-relativistic regime [55]. The drastically different scaling in the non-relativistic and ultra-relativistic

regime suggested that a rapid acceleration of the foil to ultra-relativistic velocity could effectively stop the growth of the instability [55].

2.7.1 Model-based predictions 2D

This brings us in a position to make inferences and predictions for our 2D simulations, the results of which will follow in Section 2.8.

The starting point is the above mentioned point on the scaling of the RT instability growth in the ultra-relativistic regime ($\propto t^{1/3}$) to be much slower than in the non-relativistic case ($\propto t$) [55]. However, in the ultra-relativistic case the duration of the laser-foil interaction is also considerably longer, because the laser pulse and the foil basically move with the same velocity, such that the interaction lasts for a time considerably longer than the laser pulse duration. Thus, the net effect of the growth of the RT instability is more appropriately analyzed as a function of the laser phase at the foil position ϕ instead of time t.

For the above-considered fully ionized single species foil accelerated by a $\sin^2$ laser field temporal profile, the RT instability grows as $\exp[\Phi]$ with [55]

$$\Phi = 2\pi \int d\phi \left[\frac{Zm_e a^2(\phi)\lambda}{Am_u \zeta \lambda_m}\right]^{1/2} = \frac{\pi a_0 \tau}{\sqrt{\zeta}} \sqrt{\frac{Zm_e \lambda}{Am_u \lambda_m}}, \tag{2.21}$$

which implies $\Phi \lesssim \pi\sqrt{\zeta}\tau\sqrt{Zm_e/Am_u}$ for $a_0 \lesssim \zeta$ and $\lambda_m \sim \lambda$. By comparing Eqs. (2.15)-(2.19) with Eq. (2.21), it immediately follows that :

(i) an increase of ion energy per nucleon is necessarily accompanied by an increase of the growth of the RT instability.
(ii) attaining larger ion energy with minimal RT instability development favors a larger Z/A ratio which is attained, e.g., by employing hydrogen instead of carbon.
(iii) for fixed laser fluence and foil parameters, a simultaneous increase of the laser intensity and decrease of the laser pulse duration mitigates RT instability.

The above dependence on the laser pulse intensity and duration is opposite to what has been predicted above for the 1D dynamics in Section 2.6.1, i.e., when no transverse effect exists. On one hand, this prediction in 2D suggests that an optimal region of laser pulse intensity and duration exists, where the foil acceleration is sufficiently adiabatic and transverse instabilities are sufficiently mitigated to maintain uniform RPA of the foil. On the other hand, it suggests that one needs to relax the relation between $\mathcal{E}$ and Φ in order to simultaneously increase the final ion energy while preserving the monochromatic spectral features of ideal LSA. This can be done by going beyond the simple LS model and by allowing more complex laser pulse and foil parameters.

2.8 PIC Simulation results

2.8.1 Laser Pulse Duration-Intensity Relation

In order to test the above predictions on the relation between the laser pulse intensity and the laser pulse duration, we carried out 1D and 2D PIC simulations with the fully relativistic and fully parallel PIC code Smilei [71]. In all our simulations, the laser pulse is circularly polarized with $\sin^2$ temporal field envelope and $\lambda = 0.8\,\mu$m wavelength. The considered duration of laser pulses is $\Delta_\tau = 5$, 10, 20, 30 fs full width at half maximum (FWHM) of the pulse intensity with normalized laser amplitude $a_0 \approx 71$, 50, 35, 29, respectively. The above-mentioned laser pulse duration and field amplitude are chosen such that the laser pulse fluence is the same in all considered cases. The foil is initially composed of neutral carbon with thickness $\ell = 0.056\lambda$. The foil is fully ionized by the laser pulse field at the beginning of the interaction, where its electron density reaches the maximum value of 400 n_c. Note that the foil thickness is chosen to satisfy the optimal LSA condition $a_0 \approx \zeta$ for $a_0 \approx 71$, such that $a_0 \lesssim \zeta$ and the reflectivity is approximately unity in all considered cases.

In our 2D simulations the foil is initially flat, and the laser pulse is modeled as a plane wave. Thus, no finite size effect is present, and a direct comparison with 1D results is possible. To accurately resolve the plasma dynamics, in 2D the simulation box is $16\lambda(x) \times 16\lambda(y)$ with $16000(x) \times 16000(y)$ grid points, and 66 (400) particles-per-cell are used for ions (electrons when full ionization is reached). The same spatial resolution and particles-per-cell are used in the corresponding 1D simulations.

Figure 2.4(a) and Fig. 2.4(b) report the results obtained with 1D and 2D simulations, respectively. Figure 2.4(a) shows that the ion spectrum qualitatively improves with increasing laser pulse duration, with the ion energy per nucleon being in good agreement with the LS model prediction $\varepsilon_u \approx 21$ MeV. This occurs because the acceleration process is increasingly more adiabatic for longer duration and lower intensity. In fact, during the acceleration process the equilibrium between electrostatic force and radiation pressure leads to the cyclic acceleration of ion populations at the front surface of the foil, which results into the formation of loops in the ion phase space [163, 168]. For long and less intense pulses the momentum difference of these populations is small with the foil remaining compact. By contrast, for short and intense pulses the populations at the foil front are violently pushed forward and may even overshoot the foil consequently forming distinct separated energy populations as show in Fig. 2.4(a) for the 5 fs case. In addition, the larger a_0 for shorter pulses increases the laser pulse penetration into the foil resulting into increased electron heating, and also into a stronger effect of Coulomb explosion associated to the larger electron-ion spatial separation during acceleration.

Although the above 1D effects are still present in 2D simulations, in this case the foil is also subject to instabilities that result in transverse density modulations. Notably, these density modulations depend on the temporal envelope of the laser pulse (see below). Inspite of the initial planar symmetry of the laser pulse and of the foil, Fig. 2.4(b) shows that 2D spectra are noticeably broader than the corresponding 1D spectra. In addition, in consistence with the expectation of stronger RT instability for longer duration pulses, a moderate improvement of the ion spectrum quality with decreasing laser pulse duration is visible for all cases. Remarkably, for the 5 fs duration case the ion spectrum is markedly improved and its features are much closer to those of the corresponding 1D simulation [see Fig. 2.4(b)]. This can be explained by noting that in almost all cases but the shorter duration pulse, Φ is well above unity ($\Phi > 3$), which implies that RT is saturated and fully in the nonlinear regime (see Tab. 2.1). Thus, strong transverse foil modulations with dense clumps separated by lower density regions have already formed, with the laser pulse penetrating and heating the electrons of the lower density regions [see Fig. 2.6(a)]. In this case, no compact foil is still present, such that the exact value of Φ is no longer decisive for assessing the quality of the ion spectrum.

The above results on the relation between the laser pulse intensity and its duration imply that attaining relativistic energy per nucleon and high-quality ion beams in LSA requires smart techniques to suppress transverse instabilities and also non-adiabatic acceleration effects, simultaneously. In the following we consider two possible strategies, one based on laser pulse modulation, and the other one on optimal laser pulse-foil parameter matching.

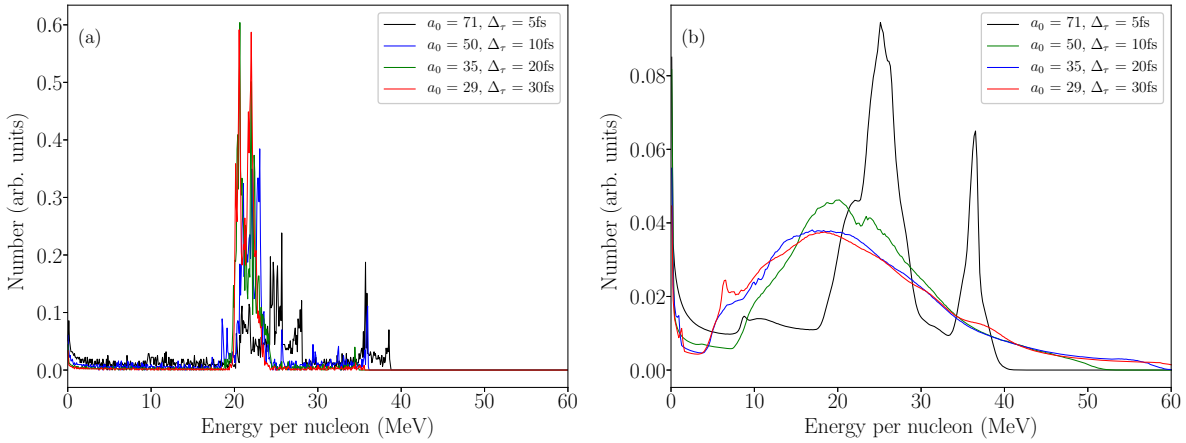

Figure 2.4: Ion energy spectrum per nucleon for an initially neutral carbon foil with thickness $\ell = 0.056\lambda$ accelerated by a superintense laser pulse with duration $\Delta_\tau = 5$, 10, 20, 30 fs and normalized amplitude $a_0 \approx 71$, 50, 35, 29, respectively. (a) 1D PIC results, (b) 2D PIC results.

a_0	Δ_τ (fs)	Φ	ε_p (MeV)	$\Delta\varepsilon_p$ (MeV)	$\Delta\varepsilon_p/\varepsilon_p$
71	5	2.3	25.2	4.4	0.17
50	10	3.2	21.0	18.6	0.89
35	20	4.5	20.0	23.2	1.20
	2×10	$2.3(1^{st})$	15.3	2.6	0.17
29	30	5.5	19.0	26.0	1.37
	3×10	$1.8(1^{st})$	20.4	4.1	0.20

Table 2.1: Average ion energy per nucleon ε_p within one FWHM energy range around the peak, FWHM of the ion peak $\Delta\varepsilon_p$ and relative energy spread $\Delta\varepsilon_p/\varepsilon_p$ from 2D PIC simulations of the interaction of a plane-wave laser pulse (train of 2 or 3 laser pulses) normalized amplitude a_0 and duration Δ_τ with a flat carbon foil with thickness $\ell = 0.056\lambda$. The LS prediction of the ion energy per nucleon is 21 MeV, while the exponent of the RT instability growth Φ is given by Eq. 2.21.

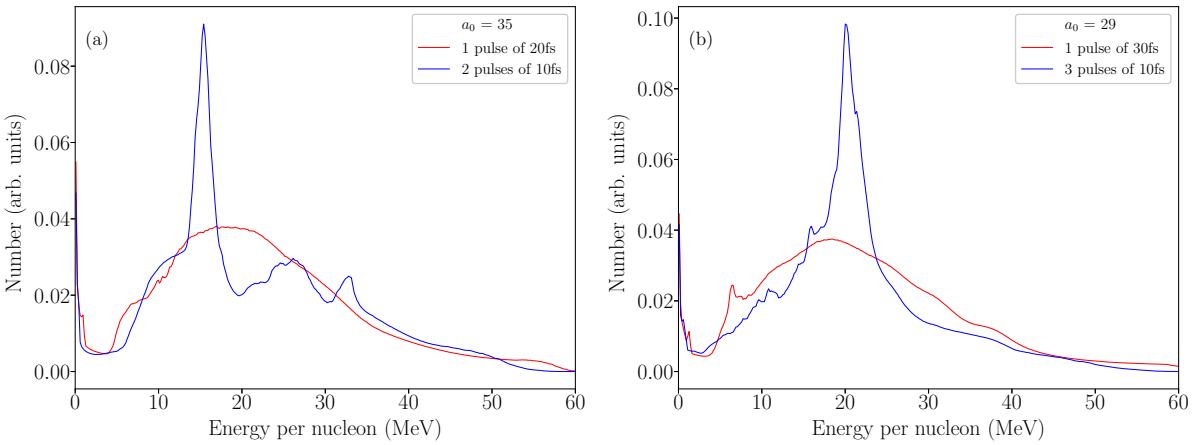

Figure 2.5: Ion energy spectrum per nucleon for an initially neutral carbon foil with thickness $\ell = 0.056\lambda$ accelerated by (a) a single 20 fs (red line) and two 10 fs (blue line) laser pulses all with $a_0 \approx 35$, (b) a single 30 fs (red line) and three 10 fs (blue line) laser pulses all with $a_0 \approx 29$.

2.8.2 Train of short pulses

The first strategy consists in accelerating the foil with a train of short and intense laser pulses where, ideally, each single laser pulse of the train is such that $\Phi \ll 1$ for the considered foil parameters and, also, longitudinal non-adiabatic effects are subdominant. The rationale is that, in this case, foil density modulations induced by each laser pulse during RPA are sufficiently small that the electrons and ions of the foil can reorganize to re-establish quasi-neutrality and diffuse from the higher density regions to the lower density regions. This may result into foil 'smoothing', i.e., the density modulations induced during

the acceleration phase are suppressed before the following laser pulse interacts with the foil. In practice, it might be difficult to obtain all the above conditions simultaneously. However, here we show that even when each laser pulse of the train is such that $\Phi \approx 2$ a substantial improvement of the ion energy spectrum is attainable compared to the single pulse case. We mention that ion acceleration with a train of two short and intense laser pulses has been already experimentally realized in the context of target normal sheath acceleration, where a significant spectral enhancement compared to the case of a single laser pulse with the same total energy was observed [169].

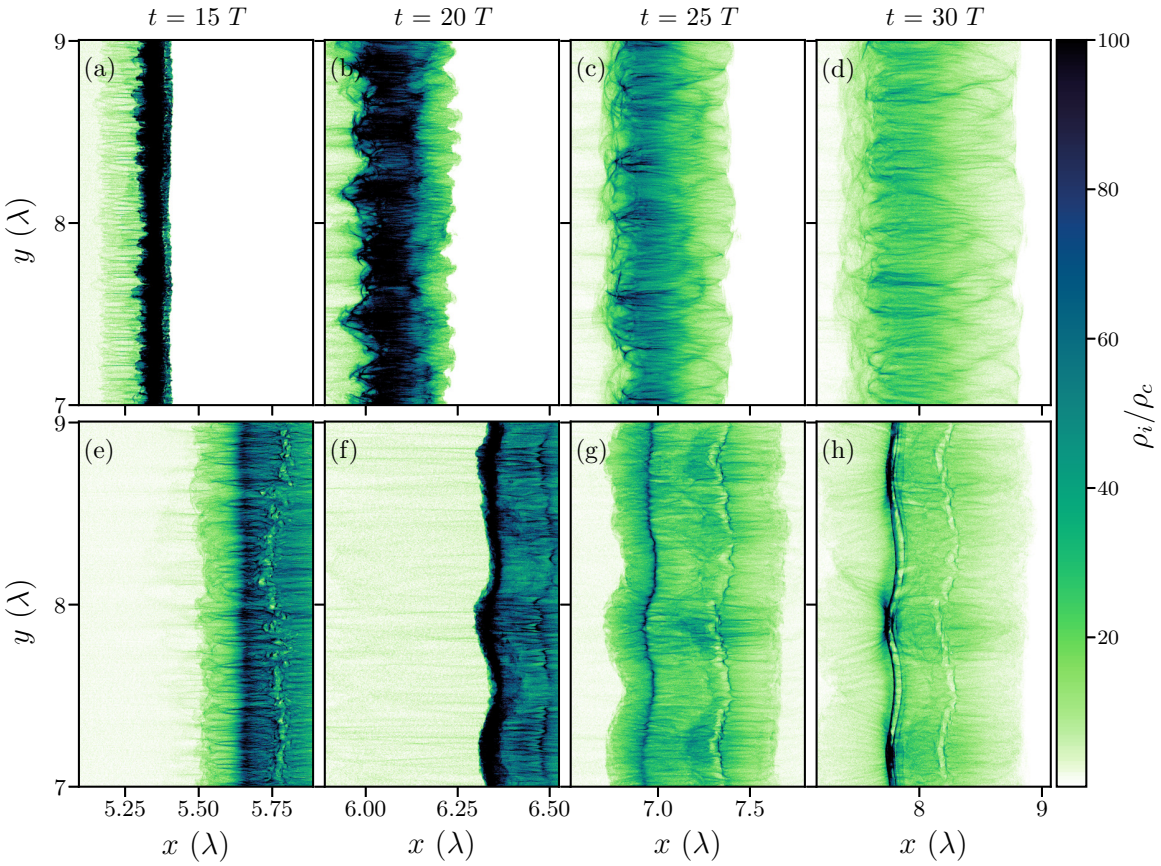

Figure 2.6: Snapshots of the ion charge density ρ_i during the laser pulse-foil interaction, which starts at $t = 0$. Snapshots are taken at 15 T, 20 T, 25 T and near the end of the laser pulse-foil interaction at 30 T. (a)-(d) single 30 fs pulse, (e)-(h) three 10 fs pulses.

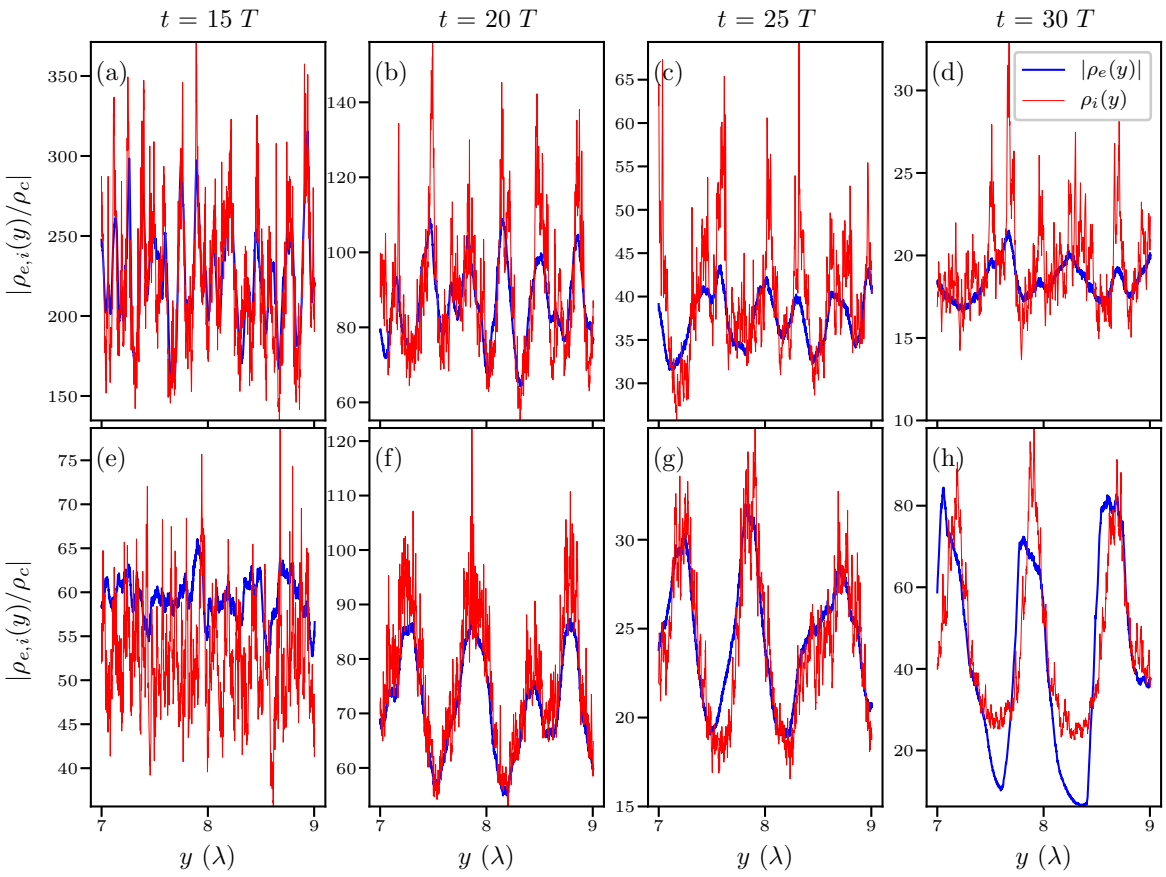

Figure 2.7: Transverse electron $|\rho_e|$ (blue line) and ion ρ_i (red line) charge density averaged over the higher density ion layer (see Fig. 2.6) in units of $\rho_c = |e|n_c$. (a)-(d) single 30 fs pulse, (e)-(h) three 10 fs pulses.

In the following we report the results of 2D simulations for a 'train' of two and three identical 10 fs laser pulses and compare these results with those of a single 20 fs and 30 fs laser pulse, respectively. For each simulation, the $\sin^2$ shape, plane-wave transverse profile, total fluence and total duration as well as the peak intensity, or equivalently a_0, is the same for the train of pulses and for the single pulse. The foil and numerical parameters are the same as in previous simulations.

Figure 2.5(a) [Figure 2.5(b)] shows the ion spectra obtained with a single 20 fs (30 fs) pulse and with a train of two (three) 10 fs laser pulses. The average ion energy per nucleon is in all cases in agreement with the LS model prediction, but the quality of the spectrum is markedly improved in the case of a train of laser pulses. In particular, a sharp peak is present in the case of multiple pulses. The relative spectral width $\Delta\varepsilon_p/\varepsilon_p \approx 0.17$ (0.20) of the peak in the spectrum for the case of two (three) pulses of 10 fs is significantly smaller

compared to $\Delta\varepsilon_p/\varepsilon_p \approx 1.20$ (1.37) for a single 20 fs (30 fs) laser pulse, as summarized in Table 2.1. The fraction of accelerated ions is also larger for the case of a pulse train, where less ions are present at lower energies (see Fig. 2.5). Here $\Delta\varepsilon_p$ is the FWHM of the peak in the ion spectrum and ε_p is the average ion energy per nucleon obtained averaging over $\pm\Delta\varepsilon_p/2$ around the peak.

More insights can be gained by considering the ion and electron dynamics during acceleration. Figure 2.6 displays snapshots of the carbon ion charge density both for a single 30 fs pulse [Figs. 2.6(a)-2.6(d)] and a train of three 10 fs pulses [Figs. 2.6(e)-2.6(h)] at intervals of 5 T starting from 15 T after the laser-foil interaction begins. Note that the peak intensity of the single 30 fs pulse reaches the foil at approximately 15 T, while for the train of pulses this occurs three times at approximately 5 T, 15 T, and 25 T. Figure 2.6 shows that, both for the single and for the train of pulses, at 15 T small scale filamentary structures followed by a denser modulated layer are present at the front of the foil. The presence of small scale modulations is further confirmed by considering the mean transverse electron $|\rho_e(y)|$ and ion $\rho_i(y)$ charge densities, which are obtained by averaging the charge distribution over a length corresponding to the thickness of the ion layer displayed in Fig. 2.6. Figure 2.7 displays $|\rho_e(y)|$ (blue line) and $\rho_i(y)$ (red line), while Fig. 2.8 reports the modulus of the Fourier transform of $\rho_i(y)$.

The formation of structures with scale λ_m much smaller than the laser wavelength λ indicates that kinetic instabilities dominate during the initial stage of acceleration [165, 166]. However, small scale modulations are later suppressed and smoothed as the laser is insensitive to structures much smaller than its wavelength due to diffraction. In fact, at later stages ($t > 25T$), modulations with scale comparable with λ clearly dominate (see Fig. 2.8) as expected from RT instability [55, 56]. Note that the suppression of small scale structures with the dominance of $\lambda_m \sim \lambda$ modes occurs earlier in the case of a train of pulses than in the case of a single pulse and is also much more pronounced (see Figs. 2.6-2.8 for $t \geq 20T$). In fact, each of the pulses of the train accelerates the foil therefore creating an electron-ion charge separation and triggering instabilities. However, the induced foil modulations are relatively small for each pulse of the train compared to the single pulse case and, as the interaction with each pulse of the train finishes, the electrons and ions of the foil diffuse longitudinally and transversely to restore local charge neutrality. This diffusion process tends to suppress most of the previously generated small scale structures, while long scale modulations are less affected. Thus, the following pulse of the train interacts with a relatively homogeneous and quasi-neutral foil, which is effectively further accelerated by radiation pressure. This sequential acceleration process is effective provided that no long scale pre-plasma has formed before each pulse interacts with the foil, such that the foil is sufficiently compact and its reflectivity remains nearly

unity.

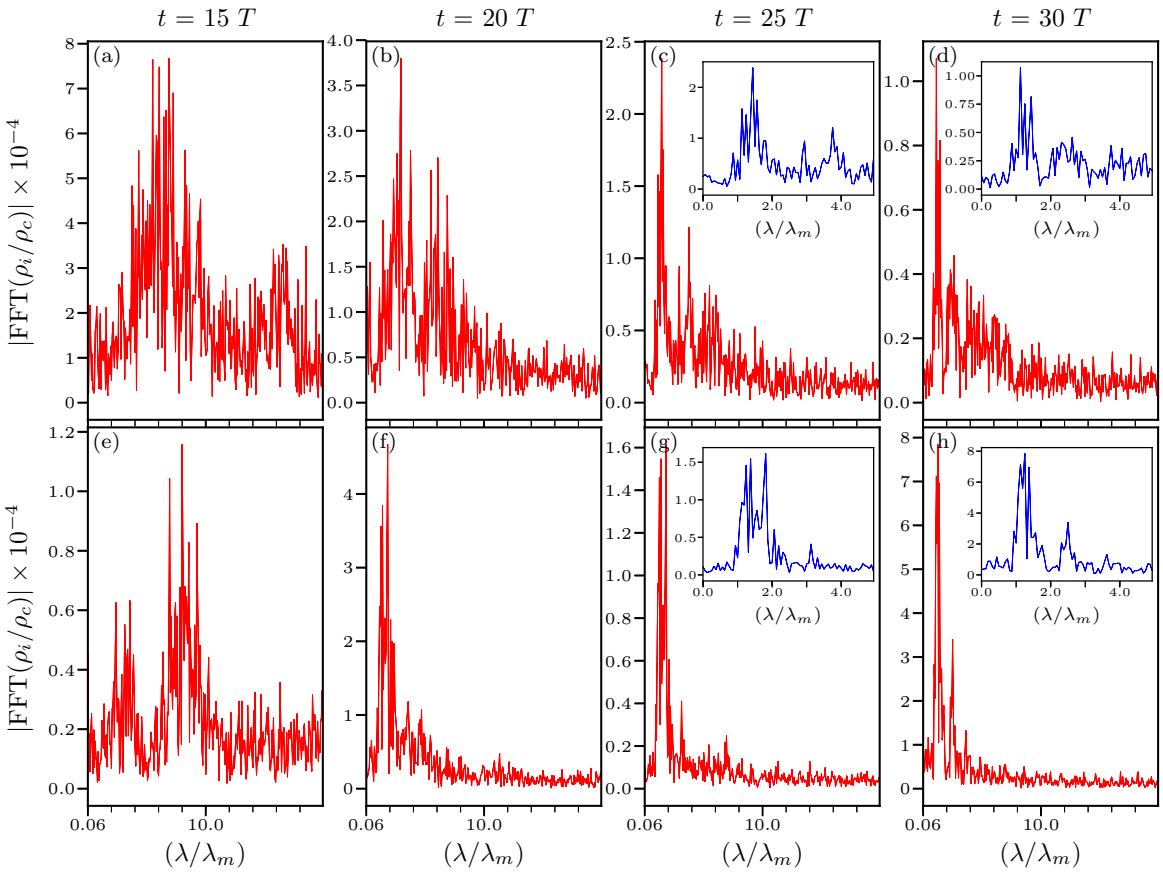

Figure 2.8: Fourier transform of the normalized transverse ion charge density $|\mathrm{FFT}(\rho_i/\rho_c)|$ averaged over the higher density ion layer taken at 15 T, 20 T, 25 T and 30 T (see Fig. 2.7). (a)-(d) single 30 fs pulse, (e)-(f)] a train of three 10 fs pulses. The insets in panels (c)-(d) and (g)-(h) (blue lines) report a zoom of the longer wavelength mode λ_m region, where λ is the laser wavelength.

Finally, we consider the effect of increasing the number of laser pulses of the train with fixed total fluence and total duration. In this case each laser pulse of the train has the same peak amplitude a_0 as in previous simulations but smaller duration, such that Φ of each pulse decreases and transverse instabilities should be relatively suppressed. However, as discussed above, a sharp rise of the laser pulse intensity renders the acceleration process increasingly less adiabatic with the possible formation of multiple ion populations with different energies and increased electron heating. Figure 2.9 shows the ion energy spectrum per nucleon for a single 30 fs pulse (black line) and a train of three 10 fs pulses (blue line), four 7.5 fs pulses (green line), and six 5 fs pulses (red line) all with the same total fluence,

peak intensity and total duration. Fig. 2.9 shows that increasing the number of laser pulses of the train reduces the number of ions at low energies and increases the total number of ions in the peak. However, the width of the peak does not reduce, and for the four 7.5 fs pulses the formation of a double peak is also observed, which is a signature of non-adiabatic acceleration. These results further confirm that high-quality spectral features are obtained when both transverse effects and non-adiabatic processes leading to the formation of multiple ion populations are suppressed.

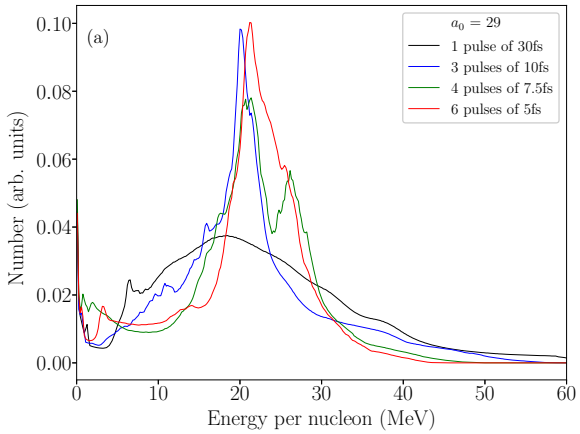

Figure 2.9: Ion energy spectrum per nucleon for an initially neutral carbon foil with thickness $\ell = 0.056\lambda$ accelerated by a single 30 fs (black line) laser pulse, a train of three 10 fs (blue line), four 7.5 fs (green line), and six 5 fs (red line) laser pulses. The normalized amplitude of each pulse is $a_0 \approx 29$.

2.8.3 Radiation Reaction effects

It has already been established with fully 3D simulations that radiation reaction (RR) effects in RPA would be more important in the case of linear polarization. For a circularly polarised pulse, the electron heating is already significantly quenched because the oscillating component of the $\mathbf{j} \times \mathbf{B}$ force is absent in this case [50]. Moreover, in this case the electrons are pushed forward along the laser-propagation direction, as opposed to them colliding with the laser pulse. Thus radiation reaction effects are greatly suppressed with the use of CP pulses. Infact the peak intensity values used in this work are much lower than the intensities at which these effects would become important [170]. This is exactly what is observed in the Fig. 2.10 which shows the ion energy spectra for a single 30 fs pulse and a train of three pulses of 10 fs with and without radiation reaction (RR) effects included in our PIC simulations. No significant difference is observed in the obtained energy spectrum.

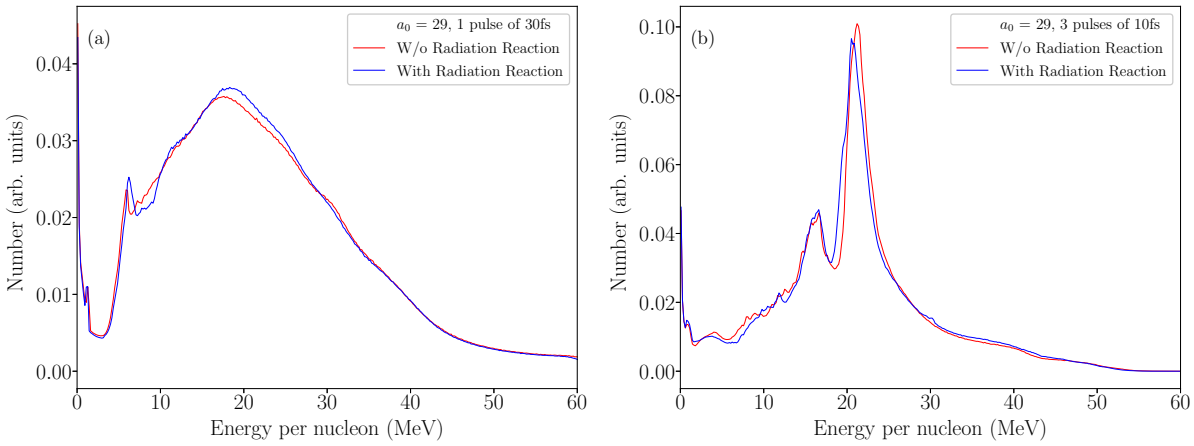

Figure 2.10: Ion energy spectrum per nucleon for an initially neutral carbon foil with thickness $\ell = 0.056\lambda$ accelerated by (a) a single 30 fs laser pulse and (b) three 10 fs laser pulses all with $a_0 \approx 29$ with (blue line) and without (red line) radiation reaction (RR) effects included.

2.8.3.1 Finite spot size effects

So far we have investigated the influence of transverse effects, mainly focusing on the dominant mode of RT instability, and of strong longitudinal gradients associated with non-adiabatic ion acceleration in the interaction of plane-wave laser pulses with flat foils. Naturally, in practice the laser pulse focal radius is of the order of a few micrometers, such that it is important to ascertain that the above findings also hold when finite spot size effects are present.

It is known that the finite size of the focal spot may result into foil deformation, and that this can be prevented either using more transversely uniform super-Gaussian profiles [171] or transversely modulated foils [61]. Here we show that by employing transversely fourth order super-Gaussian profiles, similar results as the plane-wave pulse can be obtained, such that our previous conclusions can be readily extended also to realistic finite spot size laser pulses. In our simulations, the laser has $8\,\lambda$ diameter FWHM of the intensity, while all the other laser, foil as well as numerical parameters are the same as in previous simulations but the computational box size, which was increased to $20\lambda(x) \times 16\lambda(y)$.

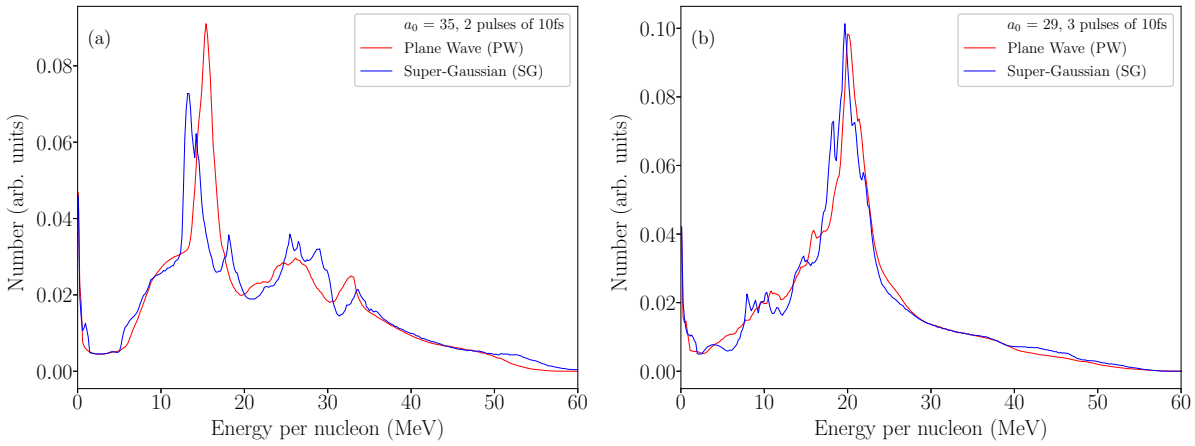

Figure 2.11: Ion energy spectrum per nucleon for an initially neutral carbon foil with thickness $\ell = 0.056\lambda$ accelerated by a train of plane-wave (PW) laser pulses (red line) and by a train of super-Gaussian (SG) laser pulses (blue line) with $8\,\lambda$ diameter. For the supergaussian case the reported spectrum corresponds to ions within $2\,\lambda$ diameter around the laser axis. (a) two 10 fs laser pulses, (b) three 10 fs laser pulses.

Figure 2.11(a)-2.11(b) display the ion spectrum per nucleon for the train of two 10 fs pulses [Figure 2.11(a)] and three 10 fs pulses [Figure 2.11(b)] both for a plane-wave pulse (red line) and for a super-Gaussian pulse (blue line), where only ions within $2\,\lambda$ diameter around the laser axis are considered. A similar spectrum is observed both for the plane-wave and for the super-Gaussian laser pulses, therefore confirming that for sufficiently uniform transverse laser profiles, finite spot size effects do not significantly affect the spectral features.

Besides a low energy spread, another important characteristic that defines the quality of the beam is the angular beam divergence. A low angular beam divergence is also essential for instance, to exploit such monoenergetic ion beams for medical applications such as ion beam therapy in particular. Figure 2.12(a)- 2.12(d) display contour maps of the distribution $f(\theta, \varepsilon_u)$ of ions as a function of angle of emission θ of the ions with respect to the target normal versus the ion energy per nucleon ε_p, for a single 30 fs pulse [Figure 2.12(a), Figure 2.12(c)] and a train of three 10 fs pulses [Figure 2.12(b), Figure 2.12(d)] with a super-Gaussian temporal profile (Note that Figure 2.12(c) and Figure 2.12(d) correspond to only the ions within $2\,\lambda$ diameter around laser axis in Figure 2.12(a) and Figure 2.12(b)). For both the cases of a single pulse and a train of pulses, the angular divergence of ions within a $2\,\lambda$ diameter around the laser axis is confined to a $\sim 10^\circ$ cone. However, in the case of a train of three pulses of 10 fs, all these ions not only have a small angular beam divergence, but a dense quasi-monoenergetic bunch is clearly seen, thus providing evidence of the good quality of the beam having a low energy and

angular spread simultaneously.

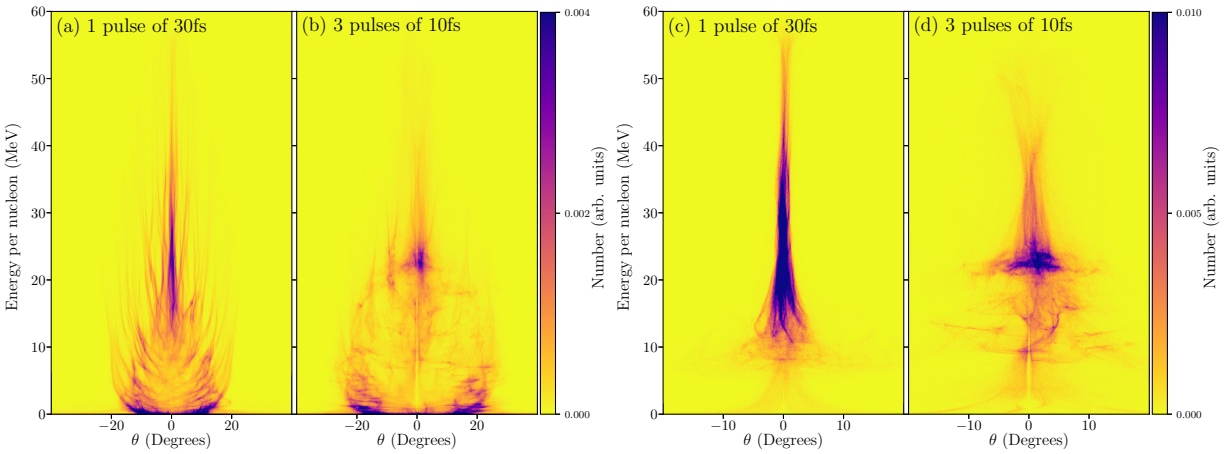

Figure 2.12: Distribution of ions as a function of energy per nucleon versus divergence angle $f(\theta, \varepsilon_u)$ for an initially neutral carbon foil with thickness $\ell = 0.056\lambda$ accelerated by a single 30 fs ((a) & (c)) and a train of three 10 fs ((b) & (d)) super-Gaussian (SG) laser pulses with $8\,\lambda$ diameter. (a)-(b) correspond to the distribution of ions $f(\theta, \varepsilon_u)$ for the full target. (c)-(d) correspond to only the ions within $2\,\lambda$ diameter around the laser axis.

2.8.4 Optimal laser pulse-foil parameter matching

In the first part of our work we have shown that RPA with relatively long duration and low intensity laser pulses favors the suppression of longitudinal non-adiabatic effects. In sharp contrast, RPA with short duration and high intensity laser pulses favors the suppression of transverse effects. This opposite tendency has been confirmed by performing high-resolution 1D and 2D PIC simulations. In fact, for example, for the shorter considered duration $\Delta_\tau \approx 5$ fs and higher intensity $a_0 \approx 71$ laser pulse, the obtained 1D and 2D spectra show nearly the same features [see the black line in Fig. 2.4(a) and Fig. 2.4(b)]. On one hand, the similarity between 1D and 2D spectra indicates that transverse effects are strongly suppressed. On the other hand, the presence of two distinct and well-separated peaks in the ion spectrum indicates that the sharp growth of the laser intensity resulted into a stronger acceleration of the front part of the foil than its rear part. In fact, the front region of the foil undergoes hole-boring acceleration with normalized velocity [172]

$$\beta_{\mathrm{HB}}(t) = \frac{v(t)_{\mathrm{HB}}}{c} = \frac{\sqrt{B(t)}}{1+\sqrt{B(t)}} \tag{2.22}$$

where $B(t) = I(t)/\rho c^3$ (here 2.10 has been written as a function of time for a realistic temporal profile). By contrast, at the beginning of the interaction $\beta_{\mathrm{LS}}(t) \approx \mathcal{E}(t) = 2\int_0^t I(t')dt'/\rho\ell c^2$, where $\beta_{\mathrm{LS}}(t)$ is the normalized light sail velocity. Thus, at the beginning

of the interaction $\beta_{\mathrm{HB}}(t) > \beta_{\mathrm{LS}}(t)$ and the front part of the foil necessarily moves earlier and faster than the rear part of the foil until the condition $\beta_{\mathrm{LS}}(t) \gtrsim \beta_{\mathrm{HB}}(t)$ is reached. Thus, a sharp rise of the laser pulse intensity creates a first ion population originating from the foil front with significantly larger energy than that of the remaining part of the foil.

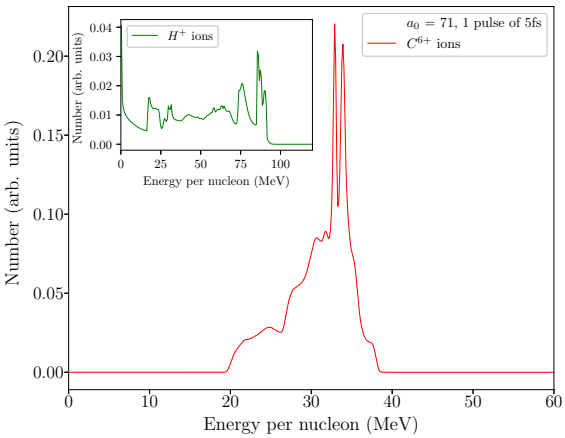

Figure 2.13: Ion energy spectrum per nucleon for carbon (red line) and hydrogen (inset, green line) in the interaction of a single 5 fs laser pulse with normalized amplitude $a_0 \approx 71$ with a double-layer foil. The foil initially consists of a first layer of hydrogen with thickness $0.64\,\lambda$ and 20 n_c electron density and a second layer of carbon with thickness $0.025\,\lambda$ and $400\,n_c$ electron density.

In order to attain high-energy and high-quality ion beams, it is therefore critical to retain the suppression of transverse effects while simultaneously reducing non-adiabatic effects that lead to the generation of distinct ion populations with noticeably different energies. Here we propose to employ short and intense laser pulses for RPA of a double-layer foil made of two distinct ion species with parameters chosen to both suppress transverse effects and achieve a smooth transition from the hole-boring to the light-sail stage. The laser pulse is the same as above, with a plane-wave transverse spatial profile, $\sin^2$ temporal field envelope, $a_0 \approx 71$ and $\Delta_\tau \approx 5$ fs. The numerical parameters are also the same as in the above-considered simulations. The foil has two layers, the first layer is made of initially neutral hydrogen with electron number density $n_{e_H} \approx 20\,n_c$ (when ionized) and $\ell_H = 0.64\,\lambda$ thickness, while the second layer is made of initially neutral carbon with electron number density $n_{e_C} \approx 400\,n_c$ (when fully ionized) and $\ell_C = 0.025\,\lambda$ thickness. For choosing the thickness of the first layer of the foil, the time t_m at which $\beta_{\mathrm{LS}}(t_m) \approx \beta_{\mathrm{HB}}(t_m)$ was first determined assuming a hydrogen foil with normalized surface density $\zeta = a_0$ and solving Eq. (2.13) numerically. Then, the thickness of the foil was chosen to match the distance traveled by the hole-boring front in a time t_m, i.e., $\ell_H \approx c\int_0^{t_m} \beta_{\mathrm{HB}}(t)\,dt$. Finally, the thickness of the second layer ℓ_C was chosen such that $\zeta = \pi(n_{e_H}\ell_H + n_{e_C}\ell_C)/n_c\lambda \approx a_0$.

The above-mentioned conditions are such that the first layer undergoes non-adiabatic effects with the formation of multiple ion populations whereas the second layer is nearly uniformly accelerated via the LS mechanism since $\beta_{\mathrm{HB}} \lesssim \beta_{\mathrm{LS}}$ when the hole-boring front starts to interact with the second layer, also due to the fact that the second layer is denser than the first one.

Figure 2.13 reports the obtained carbon (red line, main panel) and hydrogen (green line, inset) spectrum from our 2D PIC simulations. Whereas the hydrogen spectrum is very broad with multiple separated peaks corresponding to multiple ion populations, the carbon spectrum is much more narrow than in the case of a single species foil [compare with the black line in Fig. 2.4(b)] therefore indicating a strong suppression both of transverse and of longitudinal non-adiabatic effects. For carbon, the average ion energy per nucleon is $\varepsilon_p \approx 33.5$ MeV and the relative energy spread is $\Delta\varepsilon_p/\varepsilon_p \approx 0.06$. Notably, in addition to a substantial improvement of the quality of the carbon ion spectrum with respect to the single species foil case, here the obtained carbon energy per nucleon is larger than the prediction of the LS model ($\varepsilon_u \approx 21$ MeV). This occurs because, due to relativistic transparency, the laser pulse partially penetrates into the first layer, and consequently the mass of the foil that undergoes RPA acceleration is effectively smaller than that of the whole foil.

Note that foils made of two distinct but intermingled ion species were proposed to suppress RT instability, with the heavy ion species lagging behind and absorbing most of the effect of RT instability [173]. This is distinct from the case considered here, where suppression of transverse effects is essentially obtained by choosing short and intense laser pulses, and the two ions species are spatially separated, the first layer quenching longitudinal non-adiabatic effects and reducing the effective mass of the foil.

2.8.5 Pre-pulse or pre-plasma effects

In Section 2.8.2 we mentioned that the sequential acceleration process observed by employing a train of short pulses is effective "provided that no long scale pre-plasma has formed" before each pulse. Our analysis takes into account only the interaction of the foil with the main pulse. It is important to briefly talk about pre-plasma or pre-pulse effects in general, in order to get an idea regarding the limitations of these effects and the feasibility of experimentally investigating this process.

In an experimental scenario, the main pulse is always preceded by prepulses and a much longer ($\sim$ 1 ns or ps) amplified spontaneous emission (ASE) induced pedestal, which can already interact with the target, ionizing it, and thereby forming an underdense plasma expanding into vacuum much before the main pulse arrives at the target front. Thus due to the presence of already hot electrons, and expansion of the target front, the interaction

with the main pulse can be significantly different. For thinner targets, this effect can be much more pronounced, and the target can even be destroyed much before the main pulse.

However, the temporal contrast of the pulse which is the ratio of the peak intensity of the main pulse to that of the ASE pedestal is an important measure which can decide the effect of the prepulse or ASE pedestal on the interaction.

For ultra-thin targets ($\sim$ few nm) irradiated by high intensity laser pulses, the temporal contrast needs to be ultra-high ($\sim 10^{10}$ or above). Indeed, such high contrast pulses do exist in several facilities, thanks to several techniques such as using a double-plasma mirror (DPM) to improve the temporal contrast of high intensity pulses upto 10^{10} [174]. Infact, in present times it is possible to achieve even higher temporal contrasts $\sim 10^{14}$. [175] Some experiments employing high-temporal contrast pulses (10^{10}) over a wide range of target thickness reported that for thinner (sub-μm) targets, such high contrasts help with energy enhancement of ions, without disturbing the rear of the target [176, 177] and that in such conditions either a very small scale-length or no pre-plasma is formed [178]. Moreover, simulations for LS-RPA using CP pulses exploring the effect of the pre-plasma scale length on the energy conversion efficiency have also revealed that an optimal pre-plasma scale-length exists for maximum conversion efficiency [48]. It has also been found that using shorter pulses (few tens of fs) would also limit the formation of pre-plasma to shorter scale-lengths [179]. Besides, the use of CP pulses also significantly reduces the generation of hot electrons, which pose an added advantage to the availability of high pulse temporal contrasts specially in the context of LS-RPA. This has also been investigated experimentally to observe RPA of carbon C^{6+} ions for intensities of $\sim 10^{19}$ W/cm^2 for ultra-thin foils ($\sim$ few tens of nm), using temporal contrasts 10^{11} [180].

From all of the above, we are led to understand that given the current possibility of super-intense $\sim 10^{21}$ W/cm^2 short pulses (few fs), with ultra-high temporal contrasts (10^{10} - 10^{14}), it is possible to suppress the pre-plasma effects in laser-target interaction. Moreover, as suggested above, optimal control of laser and target parameters may also limit the formation of long scale pre-plasma, and may not necessarily be detrimental to the laser-foil interaction. Nevertheless, these are important factors that should be taken into account while simulating laser-plasma interaction. There are some ways of doing so, such as using hydrodynamical codes, to simulate the interaction of such a long duration ASE pedestal, in order to estimate the density evolution of the pre-plasma, and use this density distribution to initialise the target in the PIC simulation (for the main interaction). Besides this, using a power-law type density profile, or initialising the simulation with some initial charge state of the ions in order to account for ionization due to the pedestal or pre-pulse are some methods to take this into account. However, based

on the above mentioned experimental and simulation studies, specifically for LS-RPA, it would not be too unrealistic to expect that the effects of pre-pulse can be suppressed to a certain extent.

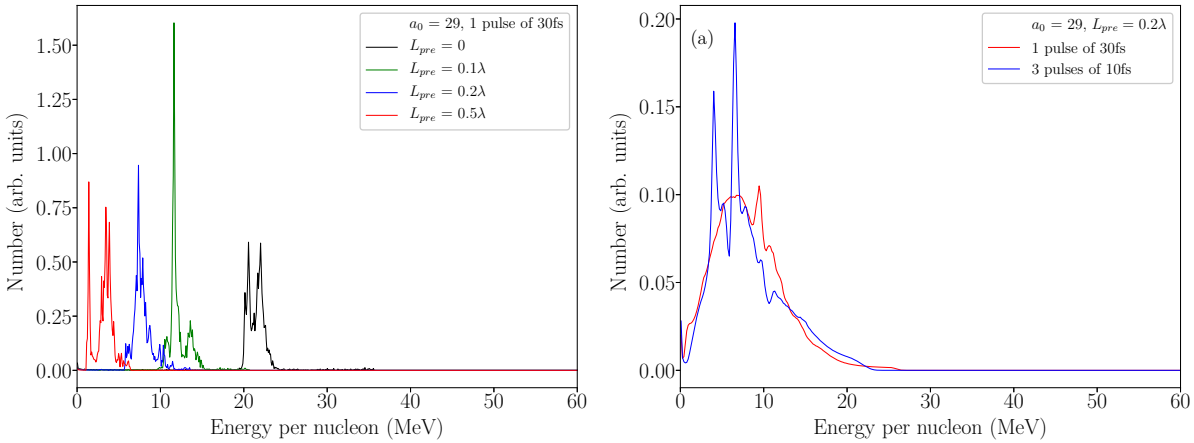

Figure 2.14: (a) : Ion energy spectrum per nucleon (1D) for a fully ionized carbon foil with a power-law type density profile $n_e(x) = n_0(x - x_0)^4/L_{\text{pre}}^4$ with thickness $L_{\text{pre}} + \ell$ accelerated by a single 30 fs laser pulse with $L_{\text{pre}} = 0, 0.1\,\lambda, 0.2\,\lambda, 0.5\,\lambda$. (b) : Ion energy spectrum per nucleon (2D) for the same fully ionized carbon foil but with $L_{\text{pre}} = 0.2\,\lambda$, accelerated by a single 30 fs pulse (red line) and three pulses of 10 fs (blue line) all with $a_0 \approx 29$.

In order to investigate the effect of pre-plasma formation on our proposed method to suppress instabilities and improve spectral quality, we performed 1D simulations with a single 30fs pulse with $a_0 = 29$, and 2D simulations with a single 30 fs pulse and three pulses of 10 fs with a plane-wave profile and with the same numerical parameters as all our previous simulations. However, now the target parameters are different. In all cases, a fully ionized carbon target was considered (ofcourse, the initial charge state would depend on the intensity of the ASE pedestal). However, for simplicity, a fully ionized target is considered, corresponding to a peak density of $n_0 = 400\ n_c$. The preplasma had a power-law type density profile $n_e(x) = n_0(x - x_0)^4/L_{\text{pre}}^4$. Here x_0 is the initial position of the target. The density rises till the peak n_0 (i.e. when $x - x_0 = L_{\text{pre}}$), and then remains constant for the thickness of the target that we have reported above $\ell = 0.056\lambda$. Therefore, now the total target thickness is $L_{\text{pre}} + \ell$. Thus, in this case the target opacity condition is still satisfied ($a_0 < \zeta$). In Fig. 2.14(a), we report 1D simulations by varying the pre-plasma scale-length. Ofcourse the highest energy gain is that for the case with no pre-plasma, and very long pre-plasma scale lengths result in very low or almost no energy gain, which is expected since the mass of the foil is increased. The spectrum however, still is quasi-monoenergetic for short enough pre-plasma scale lengths. For our 2D simulations, we chose a pre-plasma scale length = 0.2 λ and report the ion energy

spectrum in Figure 2.14(b) and density snapshots in Figure 2.15 as before for the case of a single 30 fs pulse and three pulses of 10 fs. In this case too, we clearly see the formation of a dense, quasi-neutral layer even at later stages of the interaction with the use of a train of pulses.

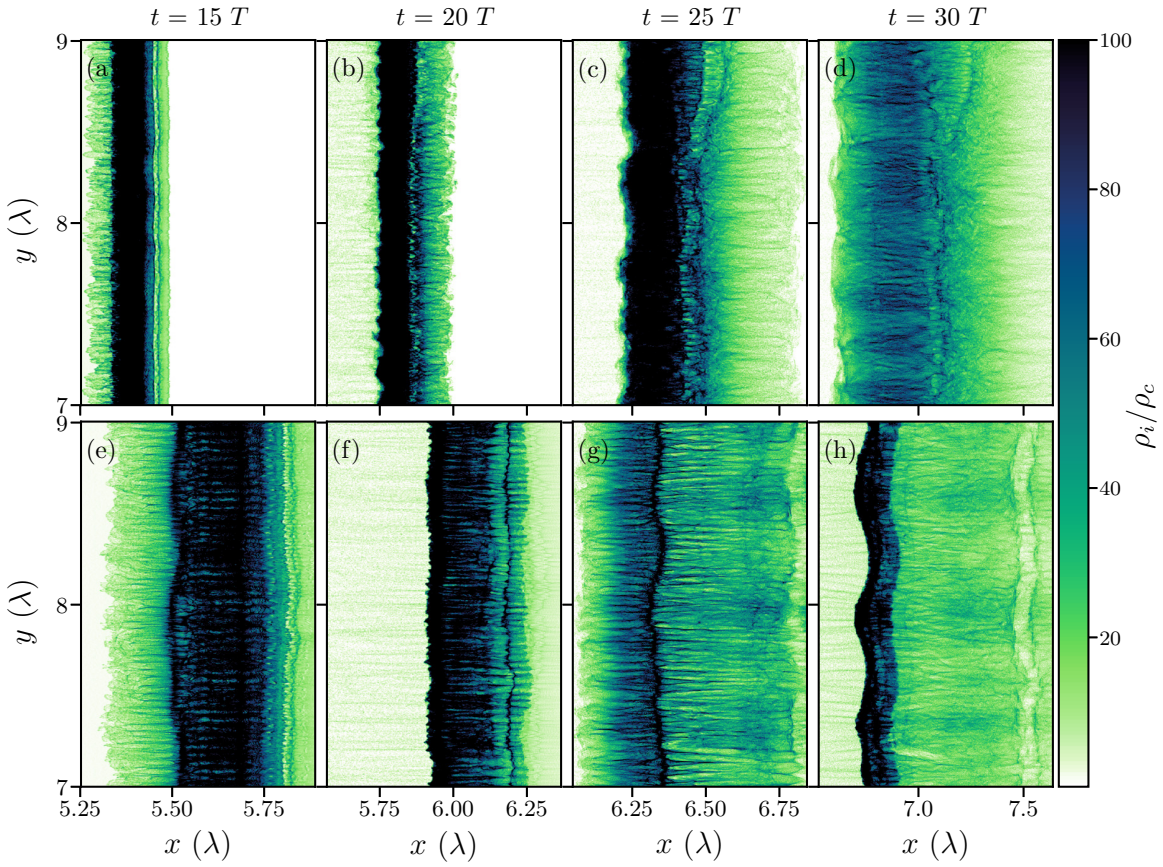

Figure 2.15: Snapshots of the ion charge density ρ_i during the laser pulse-foil interaction, which starts at $t = 0$. Snapshots are taken at 15 T, 20 T, 25 T and near the end of the laser pulse-foil interaction at 30 T. (a)-(d) single 30 fs pulse, (e)-(h) three 10 fs pulses.

Here, we would like to mention regarding why just 1D and 2D simulations are sufficient for this study. 1D simulations are important to compare with the theoretical predictions of the LS-RPA regime. In order to study transverse effects, 2D simulations are important. Comparing 2D results with the theoretical predictions of the RTI for laser interaction with thin targets, helps us understand the dynamics and propose ways to mitigate the detrimental effects of the transverse instabilities. This is what our work suggests; that shorter pulses with a sharp intensity rise improve the desired spectral features for a single laser pulse. It further proposes the use of a train of such short pulses, to improve this effect further, whilst being in a more realistic parameter regime. Hence, a 2D study is significant

as a primary step to compare with theory, understand the transverse dynamics, and at the same time suggest improvements for the given dimensionality, before performing 3D simulations. Ofcourse for a complete picture of the dynamics involved, towards a more realistic design setup, fully 3D simulations are important. Some of the differences that would arise in 3D would be that the energy gain with time predicted by the LS model would be different. Infact in 3D, a faster energy gain with time is predicted ($\sim t^{3/5}$ as opposed to $t^{1/3}$ for 1D) [181]. The transverse target deformation leads to the decrease in the areal density of the foil thereby causing a lesser number of ions to gain higher energies at an earlier stage. In 3D, there would also be the issue of angular momentum conservation and its transfer from the laser to the target, indicating non-adiabatic effects, which has been investigated in some previous studies [48, 50, 182]. Additionally, in 3D hexagonal structures are observed as predicted by the 3D theory of RTI as opposed to 2D surface ripples of the order of the laser wavelength [58, 183, 184]. However, our suggested improvements for pulse tailoring can in principle be extended also to the 3D case. Ofcourse, for a complete study, 3D simulations become inevitable, however this was not possible with our current resources.

2.9 Conclusion

In conclusion, we have provided a method to suppress detrimental effects such as transverse instabilities and multiple ion population formation by employing short and intense laser pulses together with parameter matched double-layer foils. This allows the generation of ion beams that simultaneously exhibit high-energy per nucleon and a high-quality quasi-monochromatic spectrum. Finally, we mention that further increase of the ion energy per nucleon and simultaneous improvement of the monochromatic features of the ion spectrum are attainable with hybrid schemes where the first RPA stage is followed by a second stage of energy selection and eventually further acceleration with a compact linac [185].

3 Light by Light Scattering

3.1 Introduction

The elastic scattering of two real photons ($\gamma\gamma \longrightarrow \gamma\gamma$) in vacuum is a purely quantum electrodynamic process which arises as a consequence of the non-linearity of Maxwell's equations. This is one of the predictions of quantum electrodynamics (QED) that is yet to be tested and validated. The last several decades have involved attempts aimed towards the detection of this process, some of which were mentioned in Chapter 1. However, the extreme rarity of this process on account of its very small cross-section ($\sigma_{\max} \sim 10^{-34}\, m^2$, where $\sigma_{\max}$ is the maximum probability of occurrence), has been the reason for this process having eluded detection.

Given the advances in laser development and the availability of high energy photon sources, it is timely to revisit and strive towards the possibility of detecting this process. To this end, we perform a feasibility study and propose an experiment utilising an asymmetric photon-photon collider, which involves a γ beam and a high-harmonic or a free-electron laser. This comes with the added advantage of having one source of monoenergetic photons which is tunable and controllable, and is also scalable to fit the requirements for being in the optimal region for detection. This would ensure two things : (i) that the parameters can be carefully chosen such that the energy in the CoM frame of the incoming photons is relatively higher, implying an increase in the cross-section of the process, however simultaneously still remain in the low energy region, below the threshold for pair-production such that no other competing processes are present. (ii) the probability of large angle scattering is significantly large. To this end, we perform Monte-Carlo simulations with a γ beam and an XUV laser, wherein the γ beam is generated in the interaction of an ultra-relativistic electron beam and an intense laser via nonlinear or linear Compton backscattering. The electron beam parameters are based on those available in accelerator facilities like FACET II [148] and DESY [149]. The γ beam generation is implemented computationally by my supervisor Dr. Matteo Tamburini, which is then input in the Monte-Carlo code, where the full cross-section for the photon-photon scattering process has been included.

This Chapter is organised as follows. Section 3.2 provides a background on the photon-photon scattering process and the expressions for its scattering amplitudes which are

essential also for implementing the full cross-section in our code. Section 3.3 provide the background information and expression for the electromagnetic field components of a Gaussian laser beam beyond the paraxial approximation, which is also an important requirement for our code. The following Section 3.4 will comprise of an explanation of the basic structure of the code, along with a description about each component. Finally, our proposed setup along with some simulation results will follow in Section 3.5.

3.2 Photon-Photon scattering cross-section

The cross-section for this process is a well established result, with its expressions in the low energy and high energy region first calculated by Euler [79, 80] and Acheizer [81], respectively. Thereafter, the full cross-section was calculated after the formalisation of QED by Karplus and Neuman [82,83]. Later, more simplified calculations of the scattering amplitudes which exploits the use of double-dispersion relations was presented by B. De Tollis [84, 85]. Furthermore, this approach was also used by Beretetskii, Lifshitz and Pitaevskii [86]. In the implementation of our Monte-Carlo code, we implement the full-cross section in the low energy region, i.e. below pair production threshold, where the energy in the centre-of-momentum frame (CoM) of one of the incident photons is $\omega_{\mathrm{cm}} < m_e c^2$ ($\omega_{\mathrm{cm}} < 0.511$ MeV). In this region the scattering amplitudes are real, implying no production of real electron-positron ($e^- - e^+$) pairs. Thus, in the following, we provide the key expressions for the scattering amplitudes, as presented in Ref. [86] Section 127 (with more or less the same notation for clarity), and the definition of some functions will be presented as given in Ref. [83], which are necessary for our numerical calculation for the full-cross section.

In the leading order, the following six "box" or "loop" Feynman diagrams pertain to the amplitudes of the photon-photon scattering process :

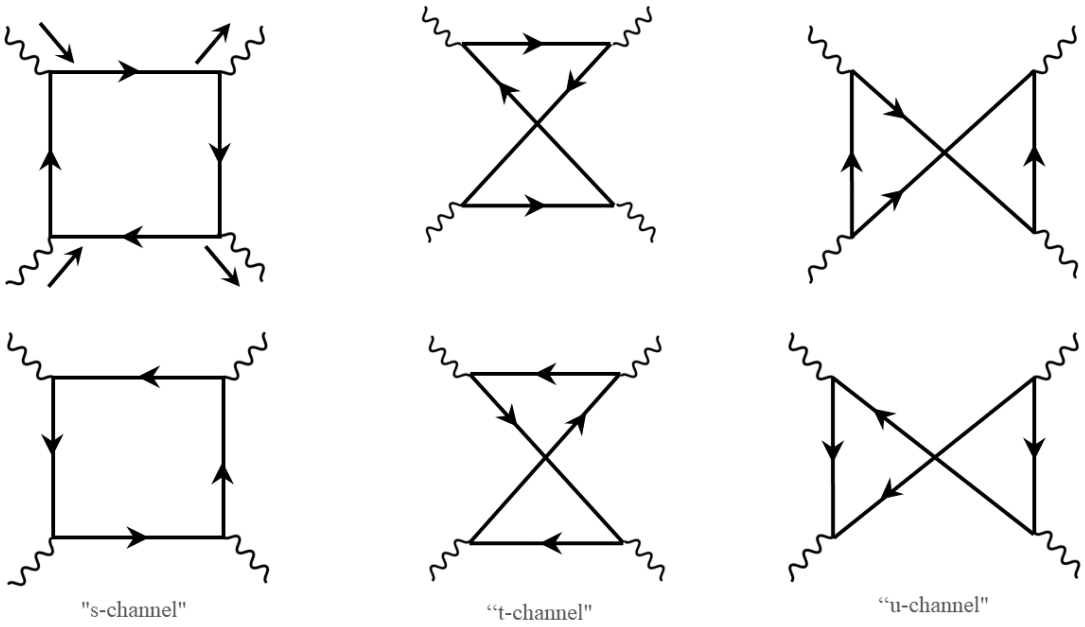

where each pair of diagrams is specified by the different possible positions of the four external photons. Thus, the above diagrams correspond to the s-channel, t-channel and u-channel respectively, with the only difference between the two diagrams in each channel being the direction of traversal of the internal electron loop. Due to charge conjugation invariance, the contribution is exactly the same for two different directions of internal electron lines in each channel. Thus, the total invariant scattering amplitude $\mathcal{M}$ is given by summing the contribution of each diagram as (denoting each channel as (a), (b), (c) in the equation below)

$$\mathcal{M} = 2\left(\mathcal{M}_a + \mathcal{M}_b + \mathcal{M}_c\right) \tag{3.1}$$

The invariant amplitudes $\mathcal{M}$ can be expressed as scalar functions of the 4-momenta (k_1, k_2, k_3, k_4) of the "real" photons (i.e. the on-shell condition $k_1^2 = k_2^2 = k_3^2 = k_4^2 = 0$ is satisfied) if their dependence on polarization of photons is written separately. Thus, $\mathcal{M}$ are expressed in terms of the Mandelstam scalar variables s, t and u, which are invariant quantities defined as

$$s = (k_1 + k_2)^2 \tag{3.2a}$$

$$t = (k_1 - k_3)^2 \tag{3.2b}$$

$$u = (k_1 - k_4)^2 \tag{3.2c}$$

which satisfy the condition $s+t+u = 0$. Now, the calculation of the invariant amplitudes is done in the centre-of-momentum (CoM) frame where the CoM energies of photons

remains the same before and after scattering, and so the momenta of the incoming and outgoing photons are defined as

$$k_1 = (\omega_{\mathrm{cm}}, \mathbf{k}) \tag{3.3a}$$
$$k_2 = (\omega_{\mathrm{cm}}, -\mathbf{k}) \tag{3.3b}$$
$$k_3 = (\omega_{\mathrm{cm}}, \mathbf{k}') \tag{3.3c}$$
$$k_4 = (\omega_{\mathrm{cm}}, -\mathbf{k}') \tag{3.3d}$$

In this frame the Mandelstam variables in Eq. 3.2 written in terms of the incoming and outgoing photon 4-momenta in Eq. 3.3 are

$$s = (\mathbf{k} - \mathbf{k})^2 = 4\,\omega_{\mathrm{cm}}^2 \tag{3.4a}$$
$$t = -(\mathbf{k} - \mathbf{k}')^2 = -4\,\omega_{\mathrm{cm}}^2 \sin^2(\theta/2) \tag{3.4b}$$
$$u = -(\mathbf{k} + \mathbf{k}')^2 = -4\,\omega_{\mathrm{cm}}^2 \cos^2(\theta/2) \tag{3.4c}$$

where θ is the scattering angle in the CoM frame between the initial incoming and final outgoing photon.

Now, the amplitude $\mathcal{M}$ written with the polarization vectors $e_1^\lambda, e_2^\mu, e_3^\nu, e_4^\rho$ of the four photons is

$$\mathcal{M} = e_1^\lambda e_2^\mu e_3^{\nu *} e_4^{\rho *} \mathcal{M}_{\lambda\mu\nu\rho} \tag{3.5}$$

where $\mathcal{M}_{\lambda\mu\nu\rho}$ is the four-dimensional photon-photon scattering tensor. With the choice of gauge where the time component of the polarization vectors vanishes, i.e., (such that the condition $\mathbf{e} \cdot \mathbf{k}$ is satisfied)

$$e_1^\mu = (0, \mathbf{e_1})\,, e_2^\mu = (0, \mathbf{e_2})\,, e_3^\mu = (0, \mathbf{e_3})\,, e_4^\mu = (0, \mathbf{e_4}) \tag{3.6}$$

the above amplitude in Eq. 3.5 is then written in terms of a three-dimensional tensor $\mathcal{M}_{iklm}$

$$\mathcal{M} = \mathcal{M}_{iklm} e_{1i} e_{2k} e_{3l}^* e_{4m}^* \tag{3.7}$$

Considering circular polarization for each photon with opposite helicities $\lambda = \pm 1$ (i.e. right and left circular polarization) $\mathcal{M}_{iklm}$ is written in terms of sixteen invariant amplitudes $\mathcal{M}_{\lambda_1\lambda_2\lambda_3\lambda_4}$

$$\mathcal{M}_{iklm} = \sum_{\lambda_1\lambda_2\lambda_3\lambda_4} \mathcal{M}_{\lambda_1\lambda_2\lambda_3\lambda_4} e_{1i}^{(\lambda_1)*} e_{2k}^{(\lambda_2)*} e_{3l}^{(\lambda_3)} e_{4m}^{(\lambda_4)} \tag{3.8}$$

Now, the sixteen $\mathcal{M}_{\lambda_1\lambda_2\lambda_3\lambda_4}$ are all three-dimensional scalar quantities, which are functions of the invariant scalar variables s, t, and u as mentioned above. However, due to the symmetry properties of this process, there are only five independent invariant amplitudes, which is made clear by parity and time invariance as follows. The rotation of each photon

or the sign of helicity would change in the case of spatial inversion. However, the invariant variables s, t and u would remain unaffected. In this case, parity invariance would imply

$$\mathcal{M}_{\lambda_1\lambda_2\lambda_3\lambda_4}(s,t,u) = \mathcal{M}_{-\lambda_1-\lambda_2-\lambda_3-\lambda_4}(s,t,u) \tag{3.9}$$

The initial and final photons would be interchanged under time reversal, wherein the helicities and the Mandelstam variables remain unchanged. Thus due to time invariance

$$\mathcal{M}_{\lambda_1\lambda_2\lambda_3\lambda_4}(s,t,u) = \mathcal{M}_{\lambda_3\lambda_4\lambda_1\lambda_2}(s,t,u) \tag{3.10}$$

Now, also because of the symmetry of the diagrams, it is found that

$$\mathcal{M}_{\lambda_1\lambda_2\lambda_3\lambda_4}(s,t,u) = \mathcal{M}_{\lambda_2\lambda_1\lambda_4\lambda_3}(s,t,u) \tag{3.11}$$

if the two initial and two final photons are interchanged (i.e. $k_1 \leftrightarrow k_2$ and $k_3 \leftrightarrow k_4$), such that the helicities are interchanged ($\lambda_1 \leftrightarrow \lambda_2$ and $\lambda_3 \leftrightarrow \lambda_4$).

Thus due to the above properties in Eqs. 3.9, 3.10, 3.11, the five independent invariant amplitudes for the case of circular polarization can then be chosen as $\mathcal{M}_{++++}$, $\mathcal{M}_{++--}$, $\mathcal{M}_{+-+-}$, $\mathcal{M}_{+--+}$, $\mathcal{M}_{+++-}$ where the helicities are now denoted as $+$ when $\lambda = 1$ and $-$ when $\lambda = -1$.

Infact, out of these five amplitudes, it is sufficient only to calculate the three amplitudes given by $\mathcal{M}_{++++}(s,t,u)$, $\mathcal{M}_{++--}(s,t,u)$ and $\mathcal{M}_{+++-}(s,t,u)$. The other two can be easily obtained due to crossing invariance since the amplitude $\mathcal{M}$ essentially corresponds to the same process in each channel. Thus, the s-channel diagram is simply converted to the t-channel by interchanging the variables $s \leftrightarrow t$ which corresponds to interchanging the four momenta $k_2 \leftrightarrow -k_3$ and the helicities $\lambda_2 \leftrightarrow -\lambda_3$. Similarly u-channel is obtained by replacing $s \leftrightarrow u$ which corresponds to the interchanges $k_2 \leftrightarrow -k_4$ and $\lambda_2 \leftrightarrow -\lambda_4$ in four momenta and helicities respectively. Therefore, using this property, the remaining two amplitudes are calculated as

$$\mathcal{M}_{+--+}(s,t,u) = \mathcal{M}_{++++}(t,s,u) \tag{3.12a}$$
$$\mathcal{M}_{+-+-}(s,t,u) = \mathcal{M}_{++++}(u,t,s) \tag{3.12b}$$

The final result of the calculation of these amplitudes as functions of the variable s, t

and u is then

$$\begin{aligned}
\mathcal{M}_{++++} &= 8\alpha^2\Bigg\{-1-\left(2+\frac{4t}{s}\right)B(t)-\left(2+\frac{4u}{s}\right)B(u)-\left[\frac{2(t^2+u^2)}{s^2}-\frac{8m^2}{s}\right][T(t)+T(u)]\\
&\quad+\frac{4m^2}{t}\left(1-\frac{2m^2}{s}\right)I(s,t)+\frac{4m^2}{u}\left(1-\frac{2m^2}{s}\right)I(s,u)\\
&\quad+\left[\frac{2(t^2+u^2)}{s^2}-\frac{16m^2}{s}-\frac{4m^2}{t}-\frac{4m^2}{u}-\frac{8m^4}{tu}\right]I(t,u)\Bigg\}\\
\mathcal{M}_{+++-} &= 8\alpha^2\Bigg\{1+4m^2\left(\frac{1}{s}+\frac{1}{t}+\frac{1}{u}\right)[T(s)+T(t)+T(u)]\\
&\quad-4\left(\frac{m^2}{u}+\frac{2m^4}{st}\right)I(s,t)-4\left(\frac{m^2}{t}+\frac{2m^4}{su}\right)I(s,u)-4\left(\frac{m^2}{s}+\frac{2m^4}{tu}\right)I(t,u)\Bigg\}\\
\mathcal{M}_{++--} &= 8\alpha^2\Bigg\{1-\frac{8m^4}{st}I(s,t)-\frac{8m^4}{su}I(s,u)-\frac{8m^4}{tu}I(t,u)\Bigg\}\\
\mathcal{M}_{+--+} &= 8\alpha^2\Bigg\{-1-\left(2+\frac{4s}{t}\right)B(s)-\left(2+\frac{4u}{t}\right)B(u)-\left[\frac{2(s^2+u^2)}{t^2}-\frac{8m^2}{t}\right][T(s)+T(u)]\\
&\quad+\frac{4m^2}{s}\left(1-\frac{2m^2}{t}\right)I(t,s)+\frac{4m^2}{u}\left(1-\frac{2m^2}{t}\right)I(t,u)\\
&\quad+\left[\frac{2(s^2+u^2)}{t^2}-\frac{16m^2}{t}-\frac{4m^2}{s}-\frac{4m^2}{u}-\frac{8m^4}{su}\right]I(s,u)\Bigg\}\\
\mathcal{M}_{+-+-} &= 8\alpha^2\Bigg\{-1-\left(2+\frac{4t}{u}\right)B(t)-\left(2+\frac{4s}{u}\right)B(s)-\left[\frac{2(t^2+s^2)}{u^2}-\frac{8m^2}{u}\right][T(t)+T(s)]\\
&\quad+\frac{4m^2}{t}\left(1-\frac{2m^2}{u}\right)I(u,t)+\frac{4m^2}{s}\left(1-\frac{2m^2}{u}\right)I(u,s)\\
&\quad+\left[\frac{2(t^2+s^2)}{u^2}-\frac{16m^2}{u}-\frac{4m^2}{t}-\frac{4m^2}{s}-\frac{8m^4}{ts}\right]I(t,s)\Bigg\}
\end{aligned} \tag{3.13}$$

where $\alpha = 1/137$ is the fine structure constant and m is the electron mass. By substituting the definitions of the Mandelstam variables in the above equation, the amplitudes are expressed as functions of energies and angles $\mathcal{M}(\omega_{\mathrm{cm}}, \theta)$ In the above, the transcendental functions B, T and I will be defined below. The differential scattering cross-section

is then obtained as

$$d\sigma = \frac{1}{256\pi^2\omega_{\rm cm}^2}|\mathcal{M}|^2 d\Omega \tag{3.14}$$

where $d\Omega = \sin\theta d\theta d\phi$ is the solid angle with θ being the scattering angle and ϕ being the azimuthal angle.

In Eq. 3.14, the scattering cross section is obtained by subsituting $|\mathcal{M}|^2$ with any of the amplitudes in Eqs. 3.13 for a given initial and final photon polarizations. However, the differential cross-section for unpolarized radiation is obtained by summing over the final polarizations and averaging over the initial polarizations. This is given as (in the case of circular polarization)

$$|\mathcal{M}|^2 = \frac{1}{4}\{2|\mathcal{M}_{++++}|^2 + 2|\mathcal{M}_{++--}|^2 + 2|\mathcal{M}_{+-+-}|^2 + 2|\mathcal{M}_{+--+}|^2 + 8|\mathcal{M}_{+++-}|^2\} \tag{3.15}$$

For very low energies where $\omega_{\rm cm} \ll m$, the expressions for the amplitudes in Eqs. 3.13 reduce to

$$\begin{aligned}
\mathcal{M}_{++++} &\approx \frac{11\alpha^2 s^2}{45m^4} \\
\mathcal{M}_{+--+} &\approx \frac{11\alpha^2 t^2}{45m^4} \\
\mathcal{M}_{+-+-} &\approx \frac{11\alpha^2 u^2}{45m^4} \\
\mathcal{M}_{++--} &\approx \frac{-\alpha^2(s^2+t^2+u^2)}{15m^4} \\
\mathcal{M}_{+++-} &\approx 0
\end{aligned} \tag{3.16}$$

Substituting the approximate expressions for amplitudes appearing in Eqs. 3.16 for low energies in Eq. 3.15, and further in Eq. 3.14, the differential cross-section for unpolarised radiation can be obtained. This is given by converting to SI units by multiplying the expression in Eq. 3.14 by the factor $m^2c^2r_e^2/\alpha^2$, and changing $\omega_{\rm cm} \to \hbar\omega_{\rm cm}$ where r_e is the classical electron radius and $\hbar$ is the reduced Planck's constant and c is the speed of light in vacuum. The asymptotic expression for differential cross-section for very low energies is then

$$d\sigma = \frac{139}{2(4\pi^2)(90)^2}\alpha^2 r_e^2 \left(\frac{\hbar\omega_{\rm cm}}{mc^2}\right)^6 (3+\cos\,\theta)^2 \sin\theta d\theta d\phi) \tag{3.17}$$

Now the full cross-section is obtained by integrating over all azimuthal angles, i.e. $\int d\phi = 2\pi$ and over θ from 0 to pi. The final result is however divided by a factor of 2 in order to take into account the identity of the final two photons. This would then correspond to the cross-section for the number of scattering events and not number of scattered particles. The full cross-section for very low energies is then

$$\sigma = \frac{973}{10125\pi}\alpha^2 r_e^2 \left(\frac{\hbar\omega_{\rm cm}}{mc^2}\right)^6 \tag{3.18}$$

Moreover, in the opposite case for very high energies $\omega_{\rm cm} \gg m$, the full cross-section is obtained as

$$\sigma = 4.7\alpha^4 \left(\frac{c}{\omega_{\rm cm}}\right)^2 \tag{3.19}$$

It can thus be noted that in the low energy region, the cross-section increases $\propto \omega_{\rm cm}^6$ whereas in the ultra-relativistic case it falls as $\propto \omega_{\rm cm}^-2$. The discontinuity $\omega_{\rm cm} = m$ corresponds to the threshold condition for pair-production. Beyond this point the scattering amplitudes in Eqs. 3.13 are complex, with the imaginary parts corresponding to the possibility of producing real electron-positron ($e^- - e^+$) pairs. In our work, the relevant region of interest is to be below the pair-production threshold in order to avoid any other background processes. Hence, our numerical calculation of the full cross-section pertains only to the low energy region. Brief details regarding this will be given later.

Before proceeding further, it is important to also give the definitions of the transcendental functions B, T, I appearing in Eqs. 3.13, since these are essential for calculating the full cross-section when the low energy approximate expression cannot be used. The definitions of these functions are taken from Ref. [83], however they will be written below in the system of units and the definitions of the Mandelstam variables s, t, and u as in Ref. [86]. The definitions are as follows. The function $B(k)$, where k could be any of the Mandelstam variables s, t and u is

$$\begin{aligned}
B(k) &= \frac{1}{2}\int_0^1 dy\, \log\left[1 - i\epsilon - \frac{k}{m^2}y(1-y)\right] \\
&= \sqrt{1 - \frac{4m^2}{k}}\, \sinh^{-1}\left(\sqrt{-\frac{k}{4m^2}}\right) - 1 && k < 0 \\
&= \sqrt{\frac{4m^2}{k} - 1}\, \sin^{-1}\left(\sqrt{\frac{k}{4m^2}}\right) - 1 && 0 < k < 4m^2 \\
&= \sqrt{1 - \frac{4m^2}{k}}\, \cosh^{-1}\left(\sqrt{\frac{k}{4m^2}}\right) - 1 - \left(\frac{\pi i}{2}\right)\sqrt{1 - \frac{4m^2}{k}} && k > 4m^2
\end{aligned} \tag{3.20}$$

Similarly, the function $T(k)$ is defined as

$$\begin{aligned} T(k) &= \int_0^1 \frac{dy}{4y(1-y)} \log\left[1 - i\epsilon - \frac{ky}{m^2}(1-y)\right] \\ &= \left(\sinh^{-1}\left(\sqrt{\frac{-k}{4m^2}}\right)\right)^2 && k < 0 \\ &= -\left(\sin^{-1}\left(\sqrt{\frac{k}{4m^2}}\right)\right)^2 && 0 < k < 4m^2 \\ &= \left(\cosh^{-1}\left(\sqrt{\frac{k}{4m^2}}\right)\right)^2 - \frac{\pi^2}{4} - i\pi \cosh^{-1}\left(\sqrt{\frac{k}{4m^2}}\right) && k > 4m^2 \end{aligned} \tag{3.21}$$

The symmetric functions $I(k,j) = I(j,k)$ where k and j are two different Mandelstam variables are defined as

$$\begin{aligned} I(k,j) = I(j,k) = \int_0^1 \frac{dy}{4y(1-y) - (4m^2(k+j))/kj} \times \\ \left(\log\left[1 - i\epsilon - \frac{k}{m^2}y(1-y)\right] + \log\left[1 - i\epsilon - \frac{j}{m^2}y(1-y)\right]\right) \end{aligned} \tag{3.22}$$

The real part of the above functions I is written in terms of the polylogarithmic Spence functions $\varphi(z) = \int_0^z dt\, \log(1-t)$ as

$$\begin{aligned} \mathrm{Re}[I(k,j)] = \frac{1}{2a}\mathrm{Re}\left[\varphi\left(\frac{a+1}{a+b(k)}\right) + \varphi\left(\frac{a+1}{a-b(k)}\right) - \varphi\left(\frac{a-1}{a+b(k)}\right) - \varphi\left(\frac{a-1}{a-b(k)}\right)\right] \\ + \frac{1}{2a}\mathrm{Re}\left[\varphi\left(\frac{a+1}{a+b(j)}\right) + \varphi\left(\frac{a+1}{a-b(j)}\right) - \varphi\left(\frac{a-1}{a+b(j)}\right) - \varphi\left(\frac{a-1}{a+b(j)}\right)\right] \end{aligned} \tag{3.23}$$

where a and b are given by

$$\begin{aligned} a &= \sqrt{1 - \frac{4m^2(k+j)}{kj}} \\ b(k) &= \sqrt{1 - \frac{4m^2}{k}} && k < 0 \text{ or } k > 4m^2 \\ &= i\sqrt{\frac{4m^2}{k} - 1} && 0 < k < 4m^2 \end{aligned} \tag{3.24}$$

When k or j is greater than $4m^2$, this would correspond to also the fact that the scattering amplitudes are complex. The imaginary part of the functions I is

$$\begin{aligned} \mathrm{Im}[I(k,j)] &= -\frac{\pi}{2a}\log\left[\frac{j}{4m^2}(a+b(k))^2\right] && k \geq 4m^2 \\ \mathrm{Im}[I(k,j)] &= -\frac{\pi}{2a}\log\left[\frac{k}{4m^2}(a+b(j))^2\right] && j \geq 4m^2 \end{aligned} \tag{3.25}$$

3.3 Fields of a Gaussian laser beam

In this section the analytical expressions for the fields of a Gaussian laser beam will be presented following the derivation in Ref. [150, 151] which is based on the method in Ref. [152]. The analytical expressions for the electric and magnetic fields of a Gaussian laser beam beyond the paraxial approximation will be presented with terms upto third order ϵ^3 in the diffraction angle ϵ. The diffraction angle $\epsilon = \lambda/\pi w_0$, where λ is the laser wavelength and w_0 the laser waist radius at the focus of the beam, is the expansion parameter used in modeling the fields. Even though in the Refs. [150, 151], higher order corrections appear (i.e. upto fifth order or even higher upto eleventh order), for our purpose in this work, only the terms upto third order in the diffraction angle will be sufficient. This will be clear below.

As has been pointed out in the work in Ref. [150] (see their discussions on Fig. 8 and Fig. 9) that for a laser with central wavelength $\lambda \approx 1\mu$m, retaining terms upto ϵ are sufficient only when the beam waist radius $w_0 > 15\mu$m. Thus the paraxial approximation is suitable only if the waist radius is much larger than the laser wavelength or if the region of interest is very close to the beam axis. However, for a laser beam focussed to a spot radius ranging from $7\mu\text{m} < w_0 < 15\mu$m, atleast terms upto ϵ^3 are required to correctly model the fields. This is because, for instance, for a beam with $w_0 = 8\mu$m, if only terms upto ϵ are retained, then ϵ is not really small if it is considered as an expansion parameter. Moreover, even the power and intensity of the beam also need to be correctly calculated for smaller beam spot sizes by taking into account higher order terms in ϵ. Ofcourse, even higher order corrections are needed for very tightly focussed beams. Infact, in the discussion in [150], for a spot size in the range 7μ m $< w_0 < 15\mu$m, introducing terms also upto fifth order do not differ significantly from the results obtained with only the third order terms. Hence, for the purpose of this work, retaining only terms upto ϵ^3 would be necessary and sufficient, since the minimum waist radius we implement corresponding to a $\lambda \sim 1\mu$m laser, would be $w_0 \sim 8\mu$m. The derivation and expressions for field components of a linearly polarized Gaussian beam [150] with a temporal pulse profile, essential for our work are reported below. The convention and notation is as used in this reference for the sake of clarity.

The direction of propagation of the beam is considered to be along z-axis. A Cartesian coordinate system is considered, with its origin $(0, 0, 0)$ being the (stationary) focus of the beam (refer to Fig. 3.1). The beam fields have linear polarzation along x, with a harmonic time dependence of the form $e^{i\omega t}$, where ω is the angular frequency. The temporal envelope function associated with the pulse is $g(\eta)$ where $\eta = \omega t - kz$ being the phase and $k = \omega/c$ being the wavenumber of the beam fields.

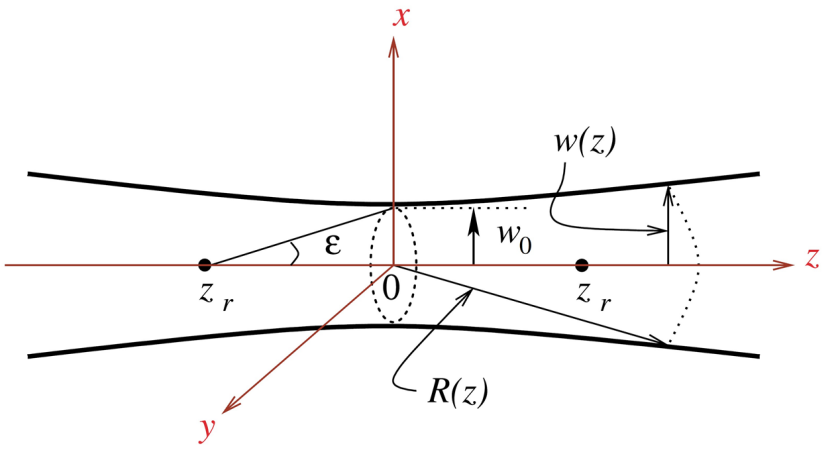

Figure 3.1: : Schematic representation of the Gaussian beam geometry. Figure taken from [150].

The fields are then derived from a vector potential $\mathbf{A}$ and scalar potential Φ. The vector potential expressed in terms of its spatial and temporal parts as

$$\mathbf{A} = \hat{\mathbf{x}} A_0 g(\eta)\psi(\mathbf{r})e^{i\eta} \tag{3.26}$$

The wave equation satisfied by the vector potential is then

$$\nabla^2 \mathbf{A} = \frac{1}{c^2}\frac{\partial^2 \mathbf{A}}{\partial t^2} \tag{3.27}$$

such that the Lorentz condition is also satisfied, which connects the vector potential $\mathbf{A}$ to the scalar potential Φ as (Gaussian units)

$$\nabla \cdot \mathbf{A} + \frac{1}{c^2}\frac{\partial \Phi}{\partial t} = 0 \tag{3.28}$$

The wave equation Eq. 3.27 can be solved by substituting the vector potential $\mathbf{A}$ given in Eq. 3.26, which results in

$$\nabla^2 \Psi - 2ik\frac{\partial \Psi}{\partial z}\left(1 - i\frac{g'}{g}\right) = 0 \tag{3.29}$$

In the above, $g' = dg(\eta)/d\eta$ corresponds to the derivative of the temporal envelope function with respect to its phase. Now, based on the discussion in Ref. [152], the above Eq. 3.29 in general cannot be satisfied since the dependence of Ψ is on the spatial coordinates $\mathbf{r}$ and that of g is on the phase η. Thus, the temporal pulse profile must be subject to the condition

$$g' \ll g \tag{3.30}$$

Infact, in the Ref. [152], it is also shown that the hyperbolic secant temporal profile $g(\eta) = \mathrm{sech}(\eta/\eta_0)$ best satisfies the condition 3.30 as opposed to the Gaussian or $\sin^2$

temporal profiles. For a 'sech' profile this condition is easily satisfied everywhere for $\eta_0 \gg 1$ as

$$\frac{g'}{g} = -\left(\frac{1}{\eta_0}\right)\tanh\left(\frac{\eta}{\eta_0}\right) \tag{3.31}$$

For proceeding further with the derivation, it is convenient to employ coordinates scaled in terms of beam parameters such as the waist radius w_0 and the Rayleigh length $z_r = kw_0^2/2$ as follows.

$$\begin{aligned} \xi &= \frac{x}{w_0} \\ \upsilon &= \frac{y}{w_0} \\ \zeta &= \frac{z}{z_r} \end{aligned} \tag{3.32}$$

Now, the above solution to the wave equation Eq. 3.29, in the new scaled coordinates becomes

$$\nabla_\perp^2 \Psi - 4i\frac{\partial \Psi}{\partial \zeta} + \epsilon^2 \frac{\partial^2 \Psi}{\partial \zeta^2} = 0 \tag{3.33}$$

where the transverse Laplacian operator $\nabla_\perp$ and the diffraction angle have been introduced ϵ, and are defined as

$$\begin{aligned} \nabla_\perp^2 &= \frac{\partial^2}{\partial \xi^2} + \frac{\partial^2}{\partial \upsilon^2} \\ \epsilon &= \frac{w_0}{z_r} = \frac{\lambda}{\pi w_0} \end{aligned} \tag{3.34}$$

In Eq. 3.33, the parameter ϵ^2 is used as an expansion parameter as it is small. Therefore, $\psi(\xi, \upsilon, \zeta)$ can be given as a series expansion of the form

$$\Psi = \Psi_0 + \epsilon^2 \Psi_2 + \epsilon^4 \Psi_4 + ... \tag{3.35}$$

Thus, using the above in Eq. 3.33, one obtains

$$\begin{aligned} \nabla_\perp^2 \Psi_n - 4i\frac{\partial \Psi_n}{\partial \zeta} &= 0 \qquad n = 0 \\ \nabla_\perp^2 \Psi_{2n} - 4i\frac{\partial \Psi_{2n}}{\partial \zeta} + \frac{\partial^2 \Psi_{(2n-2)}}{\partial \zeta^2} &= 0 \qquad n \geq 1 \end{aligned} \tag{3.36}$$

Here, Ψ_0 corresponding to $n = 0$, gives the fields of a Gaussian beam in the leading order (the so-called paraxial approximation), and Ψ_{2n} for $n \geq 1$ give the higher order corrections to the fields. The above equations have exact solutions, derived in detail in the Refs. [150, 151]. In the following, the solution for the electric and magnetic fields including terms upto third order in ϵ will be reported.

After solving Eqs. 3.36, and substituting in the vector potential $\mathbf{A}$, the fields can be obtained then from the vector and scalar potentials. Under the assumption that the scalar

potential Φ also has a form similar to the vector potential, it can be written in terms of the spatial and temporal parts as

$$\Phi \sim g(\eta)\Phi(\mathbf{r})e^{i\eta} \tag{3.37}$$

Then it follows from the Lorentz gauge condition in Eq. 3.28 that

$$\begin{aligned} \frac{\partial \Phi}{\partial t} &= i\omega\Phi\left(1 - \frac{g'}{g}\right) \\ &\approx i\omega\Phi \end{aligned} \tag{3.38}$$

where the condition 3.30 has been applied. The scalar potential is obtained as

$$\Phi = \frac{i}{k}\nabla \cdot \mathbf{A} \tag{3.39}$$

Knowing the vector and scalar potentials the electric and magnetic fields then follow.

$$\begin{aligned} \mathbf{E} &= -ik\mathbf{A} - \frac{i}{k}\nabla(\nabla \cdot \mathbf{A}) \\ \mathbf{B} &= \nabla \times \mathbf{A} \end{aligned} \tag{3.40}$$

Using all the above, the analytical expressions for the 'real' electric and magnetic field components respectively, are [150] (retaining terms upto ϵ^3)

$$\begin{aligned} E_x &= E\left\{S_0 + \epsilon^2\left[\xi^2 S_2 - \frac{\rho^4 S_3}{4}\right]\right\} \\ E_y &= E\xi\upsilon\{\epsilon^2 S_2\} \\ E_z &= E\xi\left\{\epsilon\, C_1 + \epsilon^3\left[-\frac{C_2}{2} + \rho^2 C_3 - \frac{\rho^4 C_4}{4}\right]\right\} \end{aligned} \tag{3.41}$$

$$\begin{aligned} B_x &= 0 \\ B_y &= E\left\{S_0 + \epsilon^2\left[\frac{\rho^2 S_2}{2} - \frac{\rho^4 S_3}{4}\right]\right\} \\ B_z &= E\upsilon\left\{\epsilon\, C_1 + \epsilon^3\left[\frac{C_2}{2} + \frac{\rho^2 C_3}{2} - \frac{\rho^4 C_4}{4}\right]\right\} \end{aligned} \tag{3.42}$$

where E, S_n and C_n are defined as

$$\begin{aligned} E &= E_0\frac{w_0}{w}g(\eta)\exp\left[\frac{-r^2}{w^2}\right] \\ S_n &= \left(\frac{w_0}{w}\right)^n \sin(\psi + n\,\psi_G) \\ C_n &= \left(\frac{w_0}{w}\right)^n \cos(\psi + n\,\psi_G) \qquad \text{with} \\ E_0 &= kA_0\,, \qquad r^2 = x^2 + y^2\,, \qquad \rho = \frac{r}{w_0} \end{aligned} \tag{3.43}$$

In the above, ψ is defined as

$$\begin{aligned} \psi &= \psi_0 + \psi_P - \psi_R + \psi_G \qquad \text{where} \\ \psi_0 &\quad \text{is a constant} \\ \psi_P &= \eta = \omega t - kz \\ \psi_G &= \tan^{-1}\zeta \\ \psi_R &= \frac{kr^2}{2R} \end{aligned} \tag{3.44}$$

In the above, ψ_P is the plane wave phase, ψ_G is the Guoy phase associated with the phase change of π when z changes from $-\infty$ to $+\infty$, ψ_R is the phase related with the wavefront curvature, where the radius of curvature of a wavefront at an arbitrary z along the beam axis is given by

$$R(z) = z + \frac{z_r^2}{z} \tag{3.45}$$

Moreover, the average power of the laser, which is a more practical parameter, is also obtained correctly in terms of the laser waist and diffraction angle, neglecting terms of ϵ^4 and above, as [150]

$$P[\mathrm{TW}] = \frac{\pi w_0^2}{2} I_0 \left[1 + \frac{\epsilon^2}{4}\right] \tag{3.46}$$

where I_0 is the laser peak intensity. Thus for a fixed power, the beam has to be focussed to a smaller spot radius w_0 in order to increase the peak intensity. These fields have been implemented in the Monte-Carlo code, brief details of which will follow.

3.4 Monte-Carlo code

Introduction

The background information provided in the Sections 3.2, 3.3 serve as the starting point for implementation of the Monte-Carlo code for performing realistic simulations in order to estimate and optimize the feasibility of detection of the photon-photon scattering process. As already mentioned, the idea is to employ an asymmetric photon-photon collider, wherein a high energy γ beam collides with a laser beam, and to directly detect scattering events. Thus, the key points required for building a Monte-Carlo code for this probabilistic process are : (i) a realistic γ beam which can be produced in the laboratory in present times, (ii) a realistic laser beam, and ofcourse (iii) the cross-section for the occurrence of

this process. The following sub-sections will therefore consist of the basic structure of the code, some details on the implementation of different modules along with tests to validate the implementation, following with a proposed experimental setup, and some key results. It is important to mention here that the γ beam generation has been implemented by my supervisor Matteo Tamburini, which will act as the input source for my Monte-Carlo code. A brief description on the generation of the γ beam will also be presented, along with the rest of my modules.

3.4.1 Structure of the Monte-Carlo code

The code has been written in modern Fortran, and performs all basic operations in normalised units where all lengths are specified in units of $2\pi/\lambda$ and time in units of $2\pi/T$, where λ and T are the laser wavelength and time period, respectively. Energy and momentum of the photons are specified in units of $m_e c^2$ and $m_e c$ respectively, where m_e is the electron rest mass and c is the speed of light in vacuum. The electric and magnetic fields are in units of $m_e \omega c/e$ and $m_e \omega/e$, respectively, where $\omega = 2\pi/T$. However, some quantities are returned after conversion to SI units, which will be needed for some calculations. In the following, all quantities pertaining to the γ beam will be denoted with the subscript 1, and all laser photon quantitites with the subscript 2. Thus, $k_1 = (\omega_1, \mathbf{k}_1)$ and $k_2 = (\omega_2, \mathbf{k}_2)$ will be the four-momenta of the γ and laser photons in the laboratory frame respectively.

The basic flow of logic for a γ beam counter-propagating to a laser is as follows :

- Load the initial position $\mathbf{r_1}$ and momentum $\mathbf{k}_1$ of all the photons in the γ beam at $t = 0$.
- Initialize the laser, i.e. at $t = 0$ specify the initial position of the peak of a laser beam with a Gaussian spatial profile and a sech temporal envelope, with its focus at the origin.
- Start the time loop.
- At each time-step dt, loop over all the photons in the γ beam.
- At the current time t and position $\mathbf{r_{1i}}$ of the γ photon, calculate the local electric $\mathbf{E}(\mathbf{r}_{1i}, t)$ and magnetic $\mathbf{B}(\mathbf{r}_{1i}, t)$ fields of the laser beam.
- With the local values of the fields, calculate the local energy density u_2 and hence number density n_2 of the laser photons 'seen' by the current γ photon. The energy density and number density are finally computed in SI units as

$$u_{\text{laser}} = \frac{1}{2}\epsilon_0(E^2 + c^2B^2) \tag{3.47}$$

The number density (in m^{-3}) of the laser photons is then calculated by dividing the laser energy density by the energy of a single laser photon $n_2 = u_2/\omega_2$ (where ω_2 is converted to SI units).

- With the local values of the laser fields, also calculate the local Poynting vector $\mathbf{S} = \mathbf{E} \times \mathbf{B}$. The unit Poynting vector $\mathbf{S}/|\mathbf{S}|$ then gives the direction of momentum of the laser photon $\mathbf{k_2}$.
- Now, knowing the momenta of the γ and laser photons, calculate the energy in the centre-of-momentum (CoM) frame ω_{cm} of each photon, which will be needed for the calculation of the scattering cross-section in this frame.
- If $\omega_{\text{cm}} < 0.1$, calculate total cross-section σ using the low energy approximation in Eq. 3.18. Otherwise, calculate the total cross-section by numerically integrating the differential cross-section $d\sigma/d\Omega$ in Eq. 3.14, after substituting the exact scattering amplitudes 3.13 in Eq. 3.15.
- Now calculate the number of collisions N *'per γ beam photon'* using the above obtained (invariant cross-section) [186]

$$N = \sigma\, v_{\text{rel}}\, n_2\, dt \tag{3.48}$$

where v_{rel} is the invariant velocity (the velocity of one photon in the rest frame of the other photon).

- Now roll the dice. Generate a pseudo-random number r_a uniformly distributed in the range $0 \leq r_a < 1$.
- If $N > r_a$, then scattering event occurs.
- Perform scattering in the CoM frame since the differential cross-section is known in this frame. This is done by first calculating the scattering angle in CoM frame θ_{s}, by finding the root of the sampling equation using the Brent-Dekker method.

$$\int_0^{\theta_{\text{s}}} \pi \sin\theta d\theta \frac{d\sigma(\theta)}{d\theta} = r_b\, \sigma \tag{3.49}$$

where $d\Omega = 2\pi \sin\theta d\theta$ (however, as mentioned in Sec. 3.2, the factor of 2 is dropped in order to account for the identity of both photons). Here, r_b is another independent pseudo-random number uniformly distributed in the range $0 \leq r_b < 1$.

- Now obtain scattered momenta in CoM frame of the two photons by rotating them by the scattering angle θ_s. The azimuthal angle ϕ_s is chosen at random from a uniform distribution between 0 and 2π. Transform to laboratory frame and obtain $\mathbf{k}_1'$ and $\mathbf{k}_2'$.
- If $N < r_a$, nothing happens.
- Propagate the γ photon and update its position.

$$\begin{aligned} \mathbf{r}_i &= \mathbf{r_i} + d\mathbf{r}_i \\ d\mathbf{r} &= \frac{\mathbf{k}_1}{\omega_1} dt \end{aligned} \tag{3.50}$$

- End particle loop.
- End time loop.

The above is the basic flow of the code. In the following, brief discussion about the implementation of the required modules will follow.

3.4.2 Generation of the γ beam

As mentioned above, the γ beam is not generated by me. Brief discussion on the implementation of stochastic photon emission from an electron in the interaction of a relativistic electron beam with an intense, tightly focussed laser pulse (non-linear Compton scattering) will follow.

Now strong field QED effects are governed by the quantum nonlinearity parameter χ (introduced in Chapter 1). Thus, single photon emission is important when $\chi \gtrsim 1$. Moreover, for an intense laser pulse with $a_0 \gg 1$, such that the formation length for photons $\ell_f \approx \lambda/a_0$ remains much smaller than the external field temporal scale, then the locally constant field approximation (LCFA) holds. The Monte-Carlo implementation of single photon emission is based on calculating the total probability for an electron or positron to emit a photon $W_{\mathrm{rade}/p}$. A photon emission occurs if the condition $r_1 < W_{\mathrm{rade}/p} dt$ is satisfied, where r_1 is a uniformly distributed pseudo-random number between 0 and 1. If the condition is satisfied, then the energy of the emitted photon ε_γ is found as the root of the sampling equation

$$\int_0^{\varepsilon_\gamma} d\varepsilon_\gamma \frac{dW_{\mathrm{rade}/p}(\varepsilon_\gamma)}{d\varepsilon_\gamma} = r_2 W_{\mathrm{rade}/p} \tag{3.51}$$

The direction of the emitted photon is assumed to be parallel to the direction of momentum of the emitting electron or positron. For the sake of brevity, the expressions for the

total and differential probability are not provided here (see Ref. [187]). The interested reader is urged to see Ref. [134], where further details of implementation are provided.

However, the above implementation has been further improved in order to also account for the finite emission angle of the photons which is of the order $\theta \sim 1/\gamma_e$. This was done by my supervisor based on the Refs. [187, 188]. The method is to sample the triple differential spectrum of photons, where the differential probability of emission is now written per unit energy ε_γ, polar and azimuthal angles θ_γ and $\phi\gamma$ [188]. The finite angle of emission, even in the quantum regime is quite small, but it is important for our purpose. This would act as a comparison measure for us to simulate more realistically if a photon-photon scattering event can be detected, i.e. if the scattering angle is larger than this finite emission angle of the initial γ beam, then this scattering event can be distinguished as a signal.

3.4.3 Calculation of cross-section in the code

The relevant region of interest for us is to stay below the pair-production threshold. Thus, the cross-section has been implemented in the code for only $\omega_{\rm cm} < 1$. The differential cross-section using the scattering amplitudes in Eq. 3.13 was calculated in Mathematica, with the total cross-section being obtained after numerical integration. Since the relative error of the low energy approximation (Eqs. 3.60, 3.18) with respect to the exact cross-section is $\lesssim 1\%$ for $\omega_{\rm cm} < 0.1$, it is suitable to use the analytical expression in this range. For $\omega_{\rm cm} \geq 1$, it is appropriate to calculate the exact cross-section.

For the purpose of the code, this was done by tabulating the values of the cumulative cross-section $\int_0^{\theta_i} d\theta (d\sigma/d\theta)$ for discrete values of energies and upper limits of scattering angles θ_i. The total cross-section integrated from 0 to π for the same range of energies was also tabulated. This is required for solving the above sampling equation 3.49. At every bisection, the sampling equation requires both these values, which are obtained by quadratic and linear interpolation respectively. The tabulated values had equally spaced intervals with a size sufficiently small i.e. 0.001 for energies and angles in order to generate accurate results. Fig. 3.2 shows a plot of the total cross-section in the low energy region. The plot is in good agreement with the exact result [86], and implies that the calculation and tabulation of the cross-section along with the interpolation routines work fine.

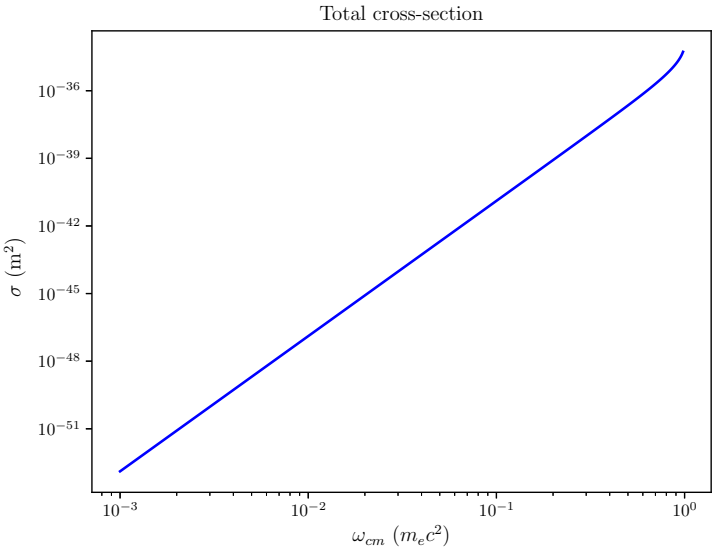

Figure 3.2: : Plot of the total photon-photon scattering cross-section in the low energy region ($\omega_{\mathrm{cm}} < 1$)

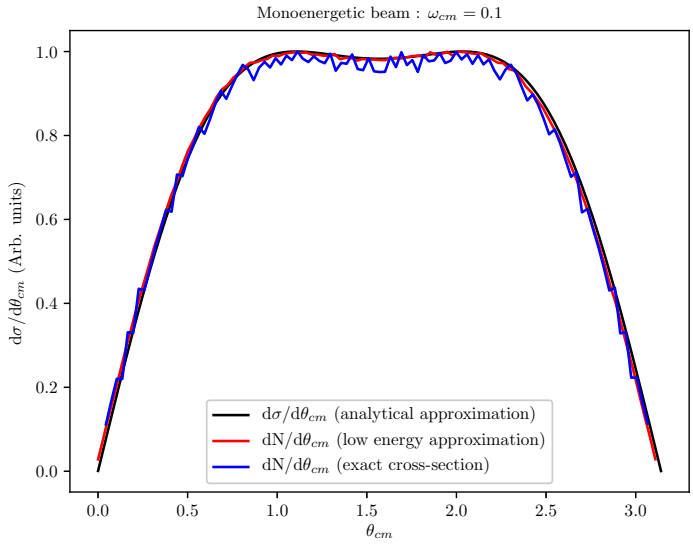

Figure 3.3: : Plots of the differential scattering cross-section (black line), and the angular distribution of scattered photons in the CoM frame,for 10^7 photons with energy $\omega_{\mathrm{cm}} = 0.1$, obtained after sampling the analytical expression for the cross-section in the low energy limit (red), and from the numerically calculated, tabulated values of the exact cross-section (blue). The value of $\omega_{\mathrm{cm}} = 0.1$ is chosen here such that both the cases of the low energy approximate expression and the exact expression can be tested, since they agree with each other within 1% relative error.

It can be verified from the Fig. 3.3 that the root finding method works as expected both for the case of the low energy approximate expression and the tabulated values of the exact cross-section.

3.4.4 Gaussian beam fields in the code

The fields of a Gaussian laser beam with a 'sech' temporal envelope function were implemented beyond the paraxial approximation based on the method described in Sec. 3.3, with terms upto ϵ^3 as in Eqs. 3.41 and 3.42. Now, these fields are required for the calculation of the local number density n_2 of the laser photons and the direction of momentum of the photons as described in the above section 3.4. This method is valid if the laser pulse is long enough ($\tau \gg T$) and is not very tightly focussed ($w_0 \gg \lambda$), such that it has a well defined frequency, which will be the case for us. Moreover, if the laser pulse is sufficiently long, the above method of employing local field values instead of cycle-averaged values is valid, as the final values of energy density u_2 over the course of interaction will be smoothed out.

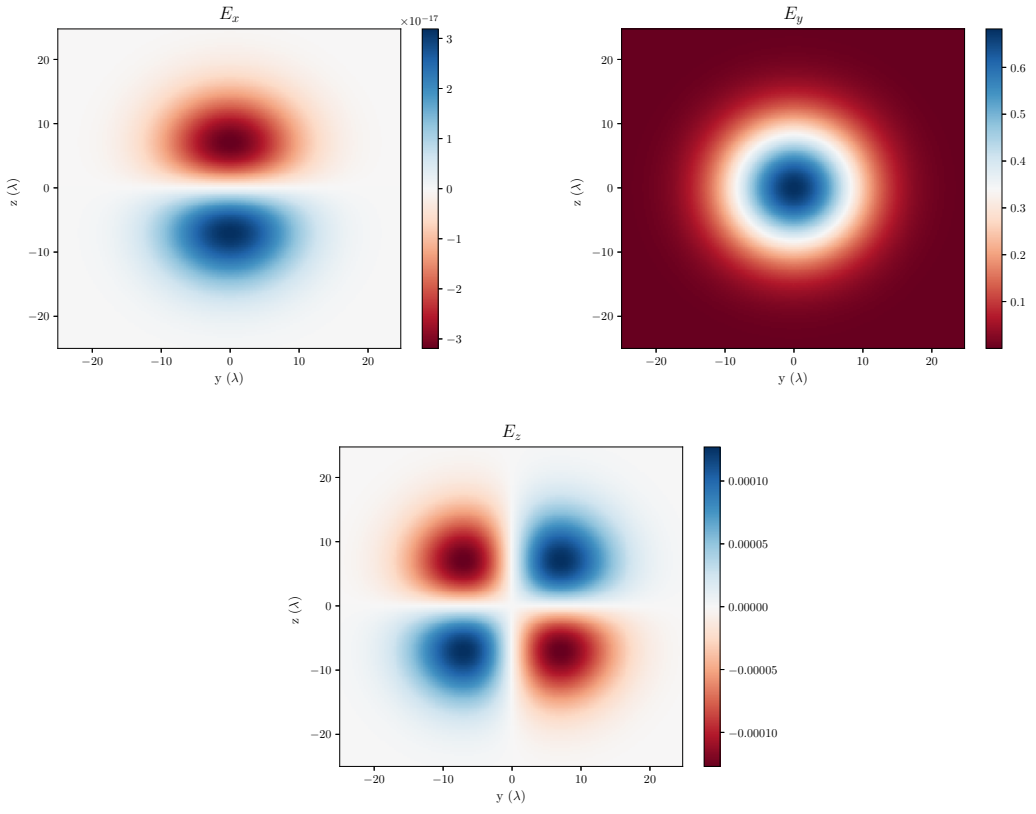

Figure 3.4: : The electric field components for a continuous laser beam with x axis as the beam axis, and polarization along y axis. The figures show the contour plots of the fields of a laser beam at the focus $(0, 0, 0)$, with wavelength $\lambda = 0.8\mu$m and waist radius $w_0 = 8\mu$m.

It is to be noted that the conventions used in the code are different from that reported in Sec. 3.3. In the code, the propagation axis is along x and polarization is along y, such that the electric and magnetic field components in Eq. 3.3 are also changed accordingly.

Figs. 3.4 and 3.5 show the plots of the electric and magnetic field components for a continuous beam ($g(\eta) = 1$). The plots correspond to a beam centered at the focus in a plane perpendicular to the beam axis. The results are as expected and in good agreement with the corresponding esults in Ref. [150], on which the implementation is based.

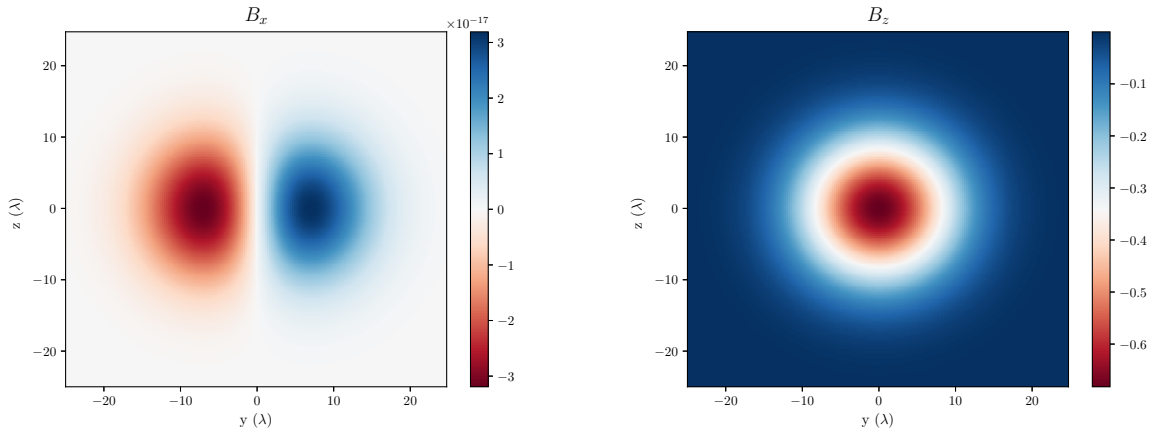

Figure 3.5: : The magnetic field components for a continuous laser beam with x axis as the beam axis, and polarization along y axis. The figures show the contour plots of the fields of a laser beam at the focus $(0, 0, 0)$, with wavelength $\lambda = 0.8\mu$m and waist radius $w_0 = 8\mu$m.

The above plots verify the correct implementation of the fields in our code.

3.4.5 The scattering routine

If a scattering event occurs, then the momenta of the photons is to be changed, based on the scattering angle found from the solution of the sampling equation 3.49. Some details of the kinematics and transformations performed for this purpose in the code are mentioned below.

The initial momenta $\mathbf{k}_1, \mathbf{k}_2$ and energies ω_1, ω_2 of the incoming photons in the laboratory frame are known. Since scattering is performed in the CoM frame, the above are Lorentz transformed from laboratory to CoM frame. By definition of the CoM frame, the momenta of the two photons are $\mathbf{k}$ and $-\mathbf{k}$. Both share the energy equally, each having energy $\omega_{\rm cm}$. However for the sake of clarity and generality, the quantities in CoM will be denoted by the superscript “”’, and the transformation equations for both particles will be shown.

This was also done in the code to ensure correct computation, and have a general routine.

$$\begin{aligned}\mathbf{k}_1' &= \mathbf{k}_1 + \frac{(\gamma_{\rm cm}-1)}{\beta_{\rm cm}^2}(\boldsymbol{\beta}_{\rm cm}\cdot\mathbf{k}_1)\boldsymbol{\beta}_{\rm cm} - \gamma_{\rm cm}\boldsymbol{\beta}_{\rm cm}\omega_1 \\ \mathbf{k}_2' &= \mathbf{k}_2 + \frac{(\gamma_{\rm cm}-1)}{\beta_{\rm cm}^2}(\boldsymbol{\beta}_{\rm cm}\cdot\mathbf{k_1})\boldsymbol{\beta}_{\rm cm} - \gamma_{\rm cm}\boldsymbol{\beta}_{\rm cm}\omega_2\end{aligned} \tag{3.52}$$

In the above, $\gamma_{\rm cm} = 1/\sqrt{1-\beta_{\rm cm}^2}$ is the CoM frame Lorentz factor, and the velocity of the CoM frame in units of speed of light c is

$$\boldsymbol{\beta}_{\rm cm} = \frac{\mathbf{k_1}+\mathbf{k_2}}{\omega_1+\omega_2} \tag{3.53}$$

The above transformation equation corresponds to an arbitrary direction of $\beta_{\rm cm}$ with respect to the laboratory frame, as opposed to the "standard configuration" where $\beta_{\rm cm}$ is parallel to the propagation direction of the moving frame (see Ref. [189]). The energies are transformed as

$$\begin{aligned}\omega_1' &= \gamma_{\rm cm}(\omega_1 - \mathbf{k}_1\cdot\boldsymbol{\beta}_{\rm cm}) \\ \omega_2' &= \gamma_{\rm cm}(\omega_2 - \mathbf{k}_2\cdot\boldsymbol{\beta}_{\rm cm})\end{aligned} \tag{3.54}$$

Now, it is convenient to rotate the momentum in CoM such that it is aligned with the propagation direction (x in our case). This simplifies the calculation of momenta after scattering.

The rotation matrix for performing this "active transformation" is

$$R = \begin{pmatrix} \cos\theta_{\rm R} & \sin\theta_{\rm R}\cos\phi_{\rm R} & \sin\theta_{\rm R}\sin\phi_{\rm R} \\ -\sin\theta_{\rm R} & \cos\theta_{\rm R}\cos\phi_{\rm R} & \cos\theta_{\rm R}\sin\phi_{\rm R} \\ 0 & -\sin\phi_{\rm R} & \cos\phi_{\rm R}\end{pmatrix}$$

$$R\begin{pmatrix} k_{1'x} \\ k_{1'y} \\ k_{1'z}\end{pmatrix} = \begin{pmatrix} k_1 \\ 0 \\ 0\end{pmatrix} \tag{3.55}$$

Here $\theta_{\rm R}$ and $\phi_{\rm R}$ are the polar and azimuthal angles of the momentum vector in a spherical coordinate system, where the polar angle is measured with respect to the propagation axis. In principle, only the inverse rotation matrix R^{-1} is needed in the code for finding the final scattered momentum in CoM frame. One does not need to perform the above transformation first.

Once the scattering angle θ in the CoM frame is known, only the direction of momentum in CoM changes. Thus, expressing $\mathbf{k}_1'$ in spherical coordinates the final momentum is given by

$$\mathbf{k}_3' = (k_1', 0, 0) \longrightarrow (k_1'\cos\theta, k_1'\sin\theta\cos\phi, k_1'\sin\theta\sin\phi) \tag{3.56}$$

where now the scattered momentum in CoM frame $\mathbf{k}'_3$ has been introduced. Finally, the scattered momentum is obtained in its original orientation by performing the inverse rotation

$$\mathbf{k}'_3 = R^{-1} \begin{pmatrix} k'_1 \cos\theta \\ k'_1 \sin\theta \cos\phi \\ k'_1 \sin\theta \sin\phi \end{pmatrix} \tag{3.57}$$

Similarly, by definition of CoM frame $\mathbf{k}'_4 = -\mathbf{k}'_3$ is obtained, with the energies in CoM being invariant ($\omega'_3 = \omega'_1$, $\omega'_4 = \omega'_1$).

Following this, the final energies ω_3, ω_4 and momenta $\mathbf{k}_3$, $\mathbf{k}_4$ are obtained in the laboratory frame by inverse Lorentz transformations as follows.

$$\begin{aligned} \omega_3 &= \gamma_{\rm cm}(\omega'_3 + \mathbf{k}'_3 \cdot \boldsymbol{\beta}_{\rm cm}) \\ \omega_4 &= \gamma_{\rm cm}(\omega'_4 + \mathbf{k}'_4 \cdot \boldsymbol{\beta}_{\rm cm}) \end{aligned} \tag{3.58}$$

$$\begin{aligned} \mathbf{k}_3 &= \mathbf{k}'_3 + \frac{(\gamma_{\rm cm} - 1)}{\beta^2_{\rm cm}} (\boldsymbol{\beta}_{\rm cm} \cdot \mathbf{k}'_3)\boldsymbol{\beta}_{\rm cm} + \gamma_{\rm cm}\boldsymbol{\beta}_{\rm cm}\omega'_3 \\ \mathbf{k}_4 &= \mathbf{k}'_4 + \frac{(\gamma_{\rm cm} - 1)}{\beta^2_{\rm cm}} (\boldsymbol{\beta}_{\rm cm} \cdot \mathbf{k'}_4)\boldsymbol{\beta}_{\rm cm} + \gamma_{\rm cm}\boldsymbol{\beta}_{\rm cm}\omega'_4 \end{aligned} \tag{3.59}$$

3.4.6 Analytical estimates

The basic structure and working of the code was explained upto now. However, nothing has been mentioned about any realistic choice of parameters or observables. It is thus instructive to perform some analytical estimates based on the form of the cross-section, which will lead to deducing an optimal parameter region.

(i) First, as already mentioned, the relevant region of interest is below the pair-production threshold to avoid any background process.

(ii) Second, as can be seen from the analytical approximation of the cross-section in the low energy region in Eq. 3.18, $\sigma \propto \omega^6_{\rm cm}$. Thus, it would be preferable to stay in a region such that $\omega_{\rm cm}$ is not extremely low.

(iii) Third, the most relevant observable in the laboratory would be the angle of scattering. Thus, it will be instructive to see how the cross-section transforms from the CoM to laboratory frame.

(iv) Since the idea is to use a γ and a laser beam, the maximum possible energies of the γ beam will be constrained to presently possible values in the laboratory. This will throw light on the laser beam parameters, since the most relevant quantity contributing to the probability of this process, apart from maintaining a high $\omega_{\rm cm}$, will be the number density of the laser photons.

Let's first talk about the energies in the CoM frame. This is obtained form the invariant Mandelstam variable s, i.e. $\omega_{\rm cm} = \sqrt{s}/2 = \sqrt{\omega_1 \omega_2}$ for a head-on collision. Thus, for a fixed $\omega_{\rm cm}$, and for a fixed laser photon energy ω_2, the required γ photon energy is $\omega_1 = \omega_{\rm cm}^2/\omega_2$. Following is a table listing the values of ω_1 and $\gamma_{\rm cm}$ (defined in the previous section) for two fixed values of $\omega_{\rm cm}$ of 0.4 and 0.9 (in units of $m_e c^2$), by varying the corresponding laser photon energies.

ω_2 (eV)	Min. $\omega_{\rm cm} = 0.4$ mc^2		Max. $\omega_{\rm cm} = 0.9$ mc^2	
	$\sigma_{\rm min} \sim 5 \times 10^{-34}$ (cm^2)		$\sigma_{\rm max} \sim 7 \times 10^{-32}$ (cm^2)	
	ω_1 (GeV)	$\gamma_{\rm cm}$	ω_1 (GeV)	$\gamma_{\rm cm}$
1.55	27.0	7.0×10^4	136.5	1.5×10^5
10×1.55	2.7	6.6×10^3	14.0	1.5×10^4
20×1.55	1.3	3.3×10^3	7.0	7.4×10^3
30×1.55	0.9	2.2×10^3	4.5	5.0×10^3
40×1.55	0.7	1.6×10^3	3.4	4.0×10^3
50×1.55	0.5	1.3×10^3	2.7	3.0×10^3

From the above we can immediately make some estimates.

- It is evident that a higher harmonic laser is needed, because for an optical laser (1.55 eV), the required energy for γ photon lies between 27 - 136 GeV, which is not practical. So, for instance consider the more practically achievable case for 10^{th} harmonic ($\sim$ 15.5 eV).

- Now, for a γ beam generated by compton-backscattering an electron beam from a strong laser pulse, consider practically achievable parameters for the electron and corresponding γ beam. Thus, $N_\gamma \sim N_{e^-}$ 10^9.

- For utilising this γ beam, it needs to be rid of electrons by deflecting them with a magnetic field. Thus, after considering 10 cm propagation, one can estimate the spot area to be $S_h = \pi w_0^2 \times 10^4$ cm^2 $\sim 10^{-6}$ cm^2.

- Employing the formula in Eq. 3.48, the number of laser photons and hence total required laser pulse energy can be estimated for obtaining 1 event per shot.

- Thus for the above two values of $\omega_{\rm cm} = 0.4, 0.9$, the required number of laser photons are $\sim 10^{18}$ and $\sim 10^{16}$ corresponding to a laser pulse energy of $E_{\rm laser} = 7.5$J or 75mJ, respectively. This already supplies us the requirements on the laser number density needed to significantly raise the probability of occurrence of a scattering event.

Now that we know of the requirements on laser and γ beam energies, it is also instructive to see, how the angular distribution of scattered photons looks in CoM and laboratory frame. Now, even if $\omega_{\rm cm}$ and laser photon number density is n_2 high, such that an event occurs, the significant obervable quantity would be the scattering angles of the γ photons. For such a γ beam, the angle of emission is confined to a cone of $\sim 1/\gamma_{e^-}$, γ_{e^-} corresponding to the relativistic factor of the electron beam which emits the γ photons. Thus, it is important that the final scattering angles are larger than $1/\gamma_{e^-}$, such that if an event occurs, it can be clearly distinguished and detected.

Following this last point, a good idea can be gained by looking at the angular distribution of the scattered photons in the CoM and laboratory frames. For this, we first re-write the analytical expression 3.60 for the differential cross-section in the CoM frame with denoting all quantities with a subscript "cm".

$$\begin{aligned} d\sigma_{\rm cm} &= \frac{139}{2(4\pi^2)(90)^2}\alpha^2 r_e^2 \left(\frac{\hbar\omega_{\rm cm}}{mc^2}\right)^6 (3+\cos\,\theta_{\rm cm})^2 \sin\theta_{\rm cm} d\theta_{\rm cm} d\phi \\ &= \frac{139}{2(4\pi^2)(90)^2}\alpha^2 r_e^2 \left(\frac{\hbar\omega_{\rm cm}}{mc^2}\right)^6 \left(9\cos\theta_{\rm cm} + 2\cos^3\theta_{\rm cm} + \frac{\cos^5\theta_{\rm cm}}{5}\right)(2\pi) d\cos\theta_{\rm cm} \end{aligned} \tag{3.60}$$

Since, the cross-section is an invariant quantity, it can be transformed to the labratory frame by denoting all relevant quantities by the subscript "L" as follows

$$\begin{aligned} \frac{d\sigma}{d\Omega_{\rm L}} d\Omega_{\rm L} &= \frac{d\sigma}{d\Omega_{\rm cm}} d\Omega_{\rm cm} \\ \frac{d\sigma}{d\Omega_{\rm L}} &= \frac{d\sigma}{d\Omega_{\rm cm}} \frac{d\Omega_{\rm cm}}{d\Omega_{\rm L}} \\ \frac{d\Omega_{\rm cm}}{d\Omega_{\rm L}} &= \frac{d\cos\theta_{\rm cm}}{d\cos\theta_{\rm L}} \end{aligned} \tag{3.61}$$

Now assuming a standard configuration (for instance in a head-on collision of two photons), the transformation of angles is given as [186]

$$\begin{aligned} \cos\theta_{\rm cm} &= \frac{\cos\theta_{\rm L} - \beta_{\rm cm}}{1 - \beta_{\rm cm}\cos\theta_{\rm L}} \\ \frac{d\cos\theta_{\rm cm}}{d\cos\theta_{\rm L}} &= \frac{1-\beta_{\rm cm}^2}{(1-\beta_{\rm cm}\cos\theta_{\rm L})^2} \end{aligned} \tag{3.62}$$

The differential cross-section in the laboratory frame thus follows after using Eq. 3.62 in Eq. 3.61.

$$\begin{aligned} \frac{d\sigma}{d\Omega_{\rm L}} = \frac{139}{2(4\pi^2)(90)^2}\alpha^2 r_e^2 \left(\frac{\hbar\omega_{\rm cm}}{mc^2}\right)^6 (1-\beta_{\rm cm}^2) \times \\ \left[\frac{9}{(1-\beta_{\rm cm}\cos\theta_{\rm L})^2} + \frac{(\cos\theta_{\rm L}-\beta_{\rm cm})^4}{(1-\beta_{\rm cm}\cos\theta_{\rm L})^6} + \frac{6(\cos\theta_{\rm L}-\beta_{\rm cm})^2}{(1-\beta_{\rm cm}\cos\theta_{\rm L})^4}\right] \end{aligned} \tag{3.63}$$

From the above equations, when expressed in terms of $\gamma_{\rm cm}$ instead of $\beta_{\rm cm}$, it can be understood that, for a fixed $\omega_{\rm cm}$, $\gamma_{\rm cm}$ decreases on increasing the laser photon energy ω_2. In this case, the probability of large angle scattering in the laboratory increases. The asymmetry in energy of the two photons can thus be exploited to increase the above probability.

3.5 Our proposal

Having gained insight regarding the required region of interest, where an event can be measurable, we provide the parameters for an experimental setup, employing an asymmetric photon-photon collider in vacuum, using realistically achievable parameters. Following is a short description of the experimental and subsequent simulation parameters.

- The γ beam is generated via non-linear Compton backscattering in the collision of a relativistic electron beam with an intense laser pulse. Following are the electron beam and γ beam parameters used in my supervisor's code to generate the beam. These parameters are easily achievable in facilities like FACET-II [148]

  Electron beam : A 0.96 nC electron beam corresponding to 6×10^9 electrons, with a Gaussian energy distribution with a mean energy of 13 GeV and a standard deviation of 13 MeV. The longitudinal and spatial distributions are also Gaussian with a 20μm and 5μm standard deviation respectively. The angular spread of the beam is 23.6μrad. Cylindrical symmetry is assumed about the beam propagation axis.

- **Scattering laser** : The laser interacting with the electron beam has the following parameters
  Normalised peak amplitude $a_0 = 10$ corresponding to a peak intensity $I_0 \approx 2.2\times10^{20}$ W/cm^2
  Waist radius $w_0 = 3\mu$m (tightly focussed)
  Laser wavelength $\lambda = 0.8\mu$m
  Pulse duration (FWHM of the intensity) $\tau = 30$ fs

- **High harmonic laser** : The following are the parameters chosen based on the estimates made in the previous section for the harmonic laser used for collision with the γ beam.
  Photon energy $\omega_2 = 20$ eV
  Laser wavelength $\lambda = 0.062\mu$m

Laser waist radius $w_0 = 8\mu$m
Repetition rate = 10 Hz
Single pulse energy = 1 mJ.
Pulse duration (FWHM of the intensity) $\tau = 50$ fs
The choice of this harmonic is made in order to increase ω_{cm} as much as possible, while still remaining below the pair-production threshold. The above mentioned high-harmonic parameters can in principle be achieved specially with high-harmonic generation using Xenon gas [145], for which the cut-off in the harmonic spectrum is at 20eV. In principle, we do not need to get rid of the other harmonics generated, but for the purpose of our work, we choose the above parameters. Moreover, the high-harmonic generation process can be scaled in order to achieve the required parameters. For more accurate details on this aspect, and the actual experimental scenario for high-harmonic generation, the references pertaining to high-harmonic sources mentioned in Chapter 1 are helpful.

For the design and orientation of our proposed experimental setup, refer to Fig. 3.6.

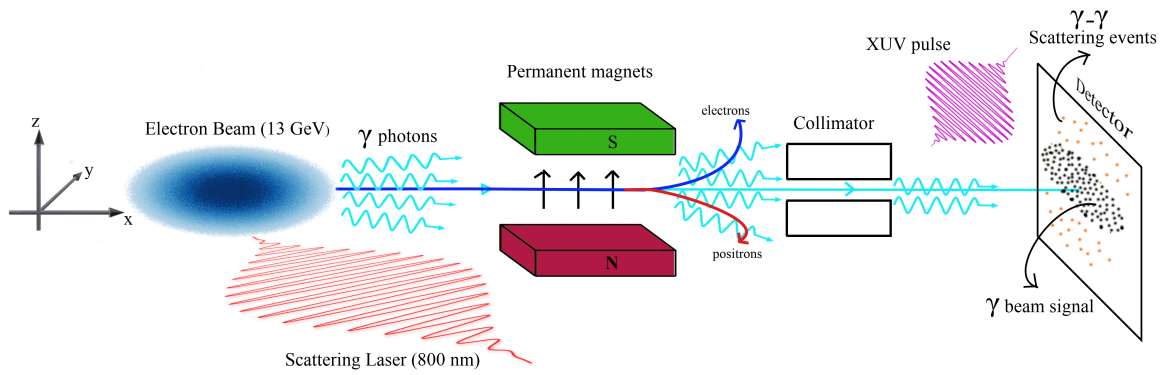

Figure 3.6: : Geometry of the experimental setup.

3.5.1 Simulation results

Based on the above mentioned physical parameters of the γ and laser beam, we now specify the the orientation of the initial beam based on the schematic of the setup, and some simulation parameters used for performing the final Monte-Carlo simulations.

In the schematic, the electron beam propagation axis is along $+x$ axis, with the scattering laser, with linearly polarized electric fields in the x-y plane. At the collision, high energy γ photons are emitted, which also have the possibility to produce e^--e^+ pairs. In order to have a pure γ beam, the beam is let to propagate some distance through a magnetic field, such that all electrons and positrons are removed, leaving only a pure γ beam. This then propagates through a collimator, such that only the photons in a given spot radius are allowed to pass through. These photons then collide with the high-harmonic (XUV) pulse propagating in the z-x plane. Finally, at the detector, only the photons that have angles in the x-y and x-z planes greater than the initial γ beam can be identified as a clear signature of scattering events. The simulation parameters are as follows.

- The initially generated γ beam was input and propagated ballistically by a distance of 15 cm.
- Only the photons within a 9μm spot radius were selected (corresponding to the final photons after passing through a collimator).
- This acted as the initial γ beam for the Monte-Carlo simulations.
- At $t = 0$, the peak of the γ beam and harmonic laser pulse is separated equidistantly from the laser focus (at origin). This means that the peak of both the beams are separated by a distance of 70μm from the focus.
- The γ beam propagates along x and the laser is incident at an angle of 10°.
- The total time of the simulation corresponds to 140μm/c seconds such that the peaks of both beams reach the laser focus at the same time, and then completely cross each other in the remaining time.
- Below, we report the cumulative results for 1 day and 1 week of operation, respectively. For a 1 mJ XUV laser, operating at 10Hz repetion rate, this corresponds to effective pulse energies of 864 J and 6048 J respectively. However, the plots below show a case of a longer pulse duration of $\sim$ 314 fs (FWHM of intensity), and a correspondingly larger pulse energy of 6.28 mJ, which corresponds to effective pulse energies of 5426 J and 37981 J,respectively.

It is important to note based on the above mentioned parameters and orientation of the setup, that the important angles as observables after scattering are those with respect to the beam propagation (x) axis in the x-z plane and those in the x-y plane. These are defined as $\psi_\gamma = \tan^{-1}(k_z/k_x)$ and $\eta_\gamma = \tan^{-1}(k_y/k_x)$. Thus, if an event occurs, only the photons that have angles larger than the initial angle ψ_γ can be detected. The initial distribution of the γ photons is reported in Fig. 3.7.

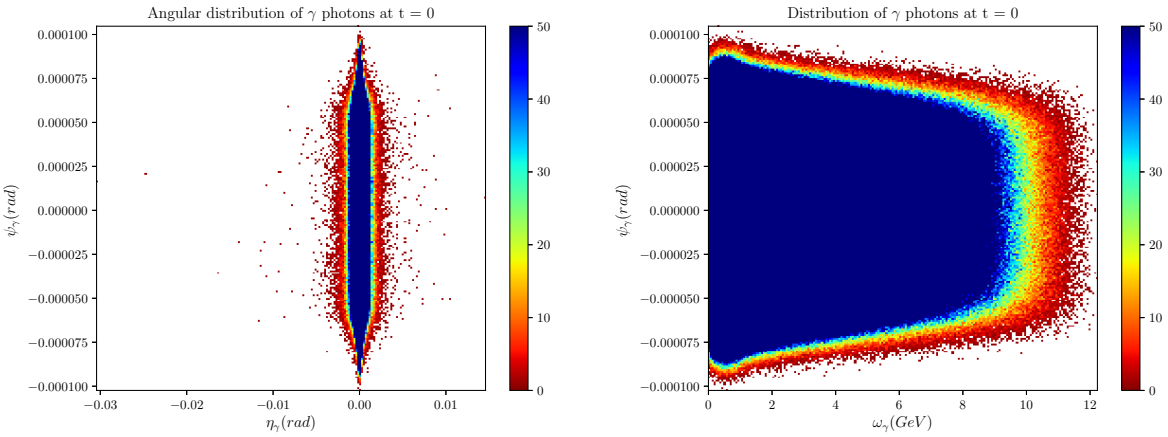

Figure 3.7: : The distribution of the initial γ photons with respect to the angles η_γ and ψ_γ (left); and with respect to the energies ω_γ and angles ψ_γ (right) for a beam propagating along $+x$ axis.

The distribution of the scattered photons over a period of one day and one week of operation is reported below

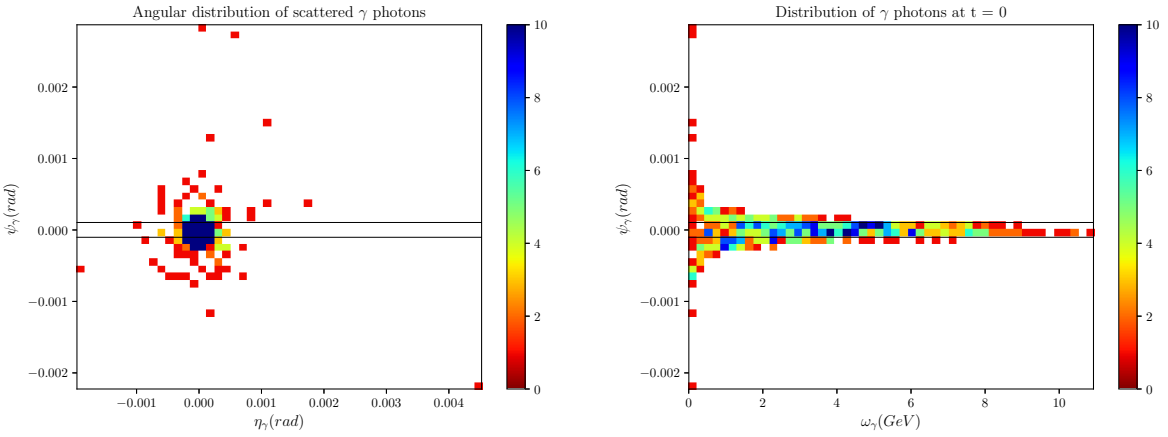

Figure 3.8: : The distribution of the scattered γ photons with respect to the angles η_γ and ψ_γ (left); and with respect to the energies ω_γ and angles ψ_γ (right). The black horizontal lines enclose the region corresponding to the initial range of the angles ψ_γ within which scattered photons cannot be measured or distinguished as signal. The results correspond to one day of operation.

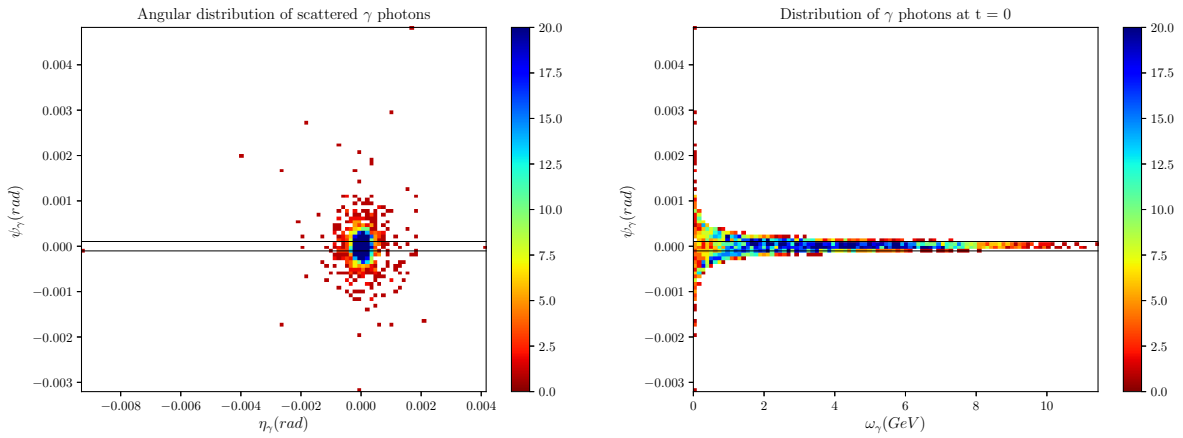

Figure 3.9: : The distribution of the scattered γ photons with respect to the angles η_γ and ψ_γ (left); and with respect to the energies ω_γ and angles ψ_γ (right). The black horizontal lines enclose the region corresponding to the initial range of the angles ψ_γ within which scattered photons cannot be measured or distinguished as signal. The results correspond to 1 week of operation

In conclusion we provided a description of the Monte-Carlo code along with its tests to verify all different modules separately. We provided some estimates on the laser and γ beam parameter requirements, following which we proposed an experimental setup. We finally reported some Monte-Carlo simulation results based on the chosen parameters and setup.

4 Summary and Outlook

The development of intense short-pulse lasers and the availability of high energy sources of radiation have played and instrumental role in the both the projects in this thesis. Not, only this they have opened up a deeper avenue for fundamental research, and technological advancements, resulting in a wide range of research, industrial or medical applications.

In Chapter 1, we emphasized on the significance and development of lasers by providing a brief history of their development. We introduced two fields of work falling under the interaction of light with matter, and light with light, and provided an overview and motivation of the specific area of research, falling under either interaction regime. The first part of this Chapter, introduced some concepts of laser-plasma interaction, and laser-driven ion acceleration mechanisms. In the second part we introduced the yet undetected, purely quantum electrodynamic (QED) process of elastic scattering of two real photons in vacuum, and briefly reviewed the efforts towards detecting this process.

In Chapter 2, we specifically talked about laser-driven ion acceleration in the light-sail regime. Since, the Particle-in-Cell method is an extremely significant tool for self-consistently modeling plasmas, and in specifically widely used for simulating laser-plasma interaction dynamics, we first introduced the reader to the basic properties and modeling of plasmas under the kinetic description, wherein we described the Maxwell-Vlasov system of equations. The power of solving the Maxwell-Vlasov system of equations by using finite-sized particles (the Particle-in-Cell (PIC) method), was then highlighted. We further gave a basic theoretical background of the different ion acceleration mechanisms in the radiation pressure dominated regime, which brought us to the mechanism of great interest to us - the light-sail regime, which is extremely favourable for the production of quasi-monoenergetic, high energy beams. Such laser-driven ion beams have however, not been produced in the laboratory because of the laser pulse triggering transverse instabilities mainly the Rayleigh-Taylor-like instability, which damage the target. We showed that the obtained ion energy per nucleon and the growth of the instability are intimately linked, and proposed ways to go beyond the existing light-sail model by employing pulse tailoring techniques to mitigate the instability. This was supported by 1D and 2D PIC simulations using the open source PIC code SMILEI [70], where we employed optimal laser-target parameter matching, by employing a train of short intense pulses to suppress the instability growth, thereby enhancing the quality of the ion energy spectrum. Further

more, we employed target-tailoring techniques to achieve a smooth transition from hole-boring to the light-sail regime, using a double-layered target, which is useful for not only suppressing the instability but also increasing the energy gain. Moreover, finite spot-size effects and pre-plasma or pre-pulse effects were also taken into account, and was found to not destroy the desirable features of the ion energy spectrum. We therefore, proposed a way to obtain high energy and high quality ion beams, using realistically achievable laser and target parameters. Such laser-driven ion beams, if successfully produced will be of significant contribution towards ion beam therapy.

In Chapter 3, we introduced the purely QED process of the elastic scattering of real photons in vacuum. Our motivation for this work is evident as this is one prediction of QED that has not yet been directly observed. We propose an experiment to directly detect the photon-photon scattering process by employing an asymmetric photon-photon collider in vacuum. This comprises of a γ beam which can be generated in in facilities such as FACET-II [148], and a high harmonic laser source, or a Free Electron Laser (FEL). The high energy of the γ photons coupled with the large laser photon flux, significantly enhances the probability of scattering events. Moreover, one photon source is highly controllable and tunable, which makes it possible to optimize the conditions for enhancing the scattering probability.

In order to propose this setup, we performed Monte-Carlo simulations on a self-written code in Fortran. The code for generating the γ beam was written by my supervisor, the final data of which was utilised in the Monte-Carlo code. We proceeded towards explaining the structure and working of the code, by first giving detailed background on the expressions for the scattering amplitudes and cross-section of this process. We further modeled the fields of the laser beam beyond the paraxial approximation based on [150]. These two background sections served as essential starting points for building the code. Finally, we also made some analytical estimates, and proceeded with a summary of the proposed experimental setup. The Monte-Carlo simulations using this realistic setup provided results indicating the hope that detecting this extremely rare process, would not elude us forever.

Another aspect of the work on light-light interaction, which has not been covered in this thesis is the prospect to detect the linear Breit-Wheeler pair-production process, a clear signature of which has also not been observed to date. This serves as the future potential of the setup proposed in this work, which in principle can also be employed in this case if the energies in the γ or laser source are such that the center-of-momentum energy exceeds the pair-production threshold. In our proposed clean experimental environment, the possibility of detecting the linear Breit-Wheeler process will also be increased as any other competing pair-production processes like the Trident or Bethe-Heitler pair produc-

tion will be greatly suppressed. Moreover, the above Monte-Carlo code for the elastic scattering of two real photons, can be improved to include also the cross-section for the linear Breit-Wheeler process, with a further potential to be added as an external QED module to existing open source PIC codes, which do not have these processes included.

Bibliography

[1] M. Planck, "Über das Gesetz der Energieverteilung im Normalspectrum," Annalen der Physik **309**, 553–563 (1901).

[2] A. Einstein, "Über einen die Erzeugung und Verwandlung des Lichtes betreffenden heuristischen Gesichtspunkt," Annalen der Physik **322**, 132–148 (1905).

[3] A. Einstein, "Zur Quantentheorie der Strahlung," Phys. Z. **18**, 121–128 (1917).

[4] H. Kopfermann and R. Ladenburg, "Experimental proof of 'Negative Dispersion'," Nature **122**, 438–439 (1928).

[5] J. P. Gordon, H. J. Zeiger, and C. H. Townes, "Molecular Microwave Oscillator and New Hyperfine Structure in the Microwave Spectrum of NH_3," Phys. Rev. **95**, 282–284 (1954).

[6] J. P. Gordon, H. J. Zeiger, and C. H. Townes, "The Maser - New Type of Microwave Amplifier, Frequency Standard, and Spectrometer," Phys. Rev. **99**, 1264–1274 (1955).

[7] A. L. Schawlow and C. H. Townes, "Infrared and Optical Masers," Phys. Rev. **112**, 1940–1949 (1958).

[8] T. H. Maiman, "Stimulated Optical Radiation in Ruby," Nature **187**, 493–494 (1960).

[9] J. Nuckolls, L. Wood, A. Thiessen, and G. Zimmerman, "Laser Compression of Matter to super-high densities: Thermonuclear (CTR) applications." Nature (London) 239: No. 5368, 139-42(15 Sep 1972). .

[10] V. V. Apollonov, P. B. Corkum, R. S. Taylor, A. J. Alcock, and H. A. Baldis, "20-J nanosecond-pulse CO_2 laser system based on an injection-mode-locked oscillator," Opt. Lett. **5**, 333–335 (1980).

[11] R. Carlson, J. Carpenter, D. Casperson, R. Gibson, R. Godwin, R. Haglund, J. Hanlon, E. Jolly, and T. Stratton, "Helios: A 15 TW carbon dioxide laser-fusion facility," IEEE Journal of Quantum Electronics **17**, 1662–1678 (1981).

[12] H. G. Ahlstrom, "Laser fusion experiments, facilities, and diagnostics at Lawrence Livermore National Laboratory," Appl. Opt. **20**, 1902–1924 (1981).

[13] K. Yamada, Y. Inada, Y. Izawa, Y. Kato, J. Kuroda, T. Sasaki, T. Yamanaka, O. Ebisu, Y. Mizumoto, and M. Monma, "Laser fusion facility 'GEKKO IV' - 4 TW four beam phosphate glass laser system," Osaka University Technology Reports **29**, 159–168 (1979).

[14] D. Strickland and G. Mourou, "Compression of amplified chirped optical pulses," Optics Communications **55**, 447 – 449 (1985).

[15] N. Sarukura, Y. Ishida, and H. Nakano, "Generation of 50-fsec pulses from a pulse-compressed, cw, passively mode-locked Ti:sapphire laser," Opt. Lett. **16**, 153–155 (1991).

[16] P. F. Moulton, "Spectroscopic and laser characteristics of Ti:Al_2O_3," J. Opt. Soc. Am. B **3**, 125–133 (1986).

[17] C. Danson, C. Haefner, J. Bromage, T. Butcher, J.-C. Chanteloup, E. Chowdhury, A. Galvanauskas, L. Gizzi, J. Hein, D. Hillier, N. Hopps, Y. Kato, E. Khazanov, R. Kodama, G. Korn, R. Li, Y. Li, J. Limpert, J. Ma, and J. Zuegel, "Petawatt and exawatt class lasers worldwide," High Power Laser Science and Engineering **7** (2019).

[18] "Extreme light infrastructure," `http://www.eli-laser.eu/` (2014).

[19] "Apollon," `https://portail.polytechnique.edu/luli/en/cilex-apollon/apollon` (2014).

[20] "Exawatt center for extreme light studies," `https://xcels.iapras.ru/` (2014).

[21] "VULCAN laser website," `https://www.clf.stfc.ac.uk/Pages/Vulcan.aspx`.

[22] "Atlas laser website," `https://www.cala-laser.de/en/instruments/light-sources.html#c2`.

[23] "Hercules laser website," `https://cuos.engin.umich.edu/researchgroups/hfs/facilities/hercules-petawatt-laser/`.

[24] "Extreme Light Infrastructure Whitebook," `https://eli-laser.eu/media/1019/eli-whitebook.pdf`.

[25] P. Gibbon, *Short Pulse Laser Interactions with Matter* (Imperial College Press, 2005).

[26] M. Protopapas, C. H. Keitel, and P. L. Knight, "Atomic physics with super-high intensity lasers," Reports on Progress in Physics **60**, 389–486 (1997).

[27] A. Macchi, *A Superintense Laser-Plasma Interaction Theory Primer* (Springer, 2013).

[28] P. Woodward, "A method of calculating the field over a plane aperture required to produce a given polar diagram," J. Inst. Electric. Eng. **93**, 1554–1558 (1947).

[29] J. D. Lawson, "Lasers and accelerators," IEEE Transactions on Nuclear Science **26**, 4217–4219 (1979).

[30] E. Esarey, C. B. Schroeder, and W. P. Leemans, "Physics of laser-driven plasma-based electron accelerators," Rev. Mod. Phys. **81**, 1229–1285 (2009).

[31] V. Malka, "Laser plasma accelerators," Physics of Plasmas **19**, 055501 (2012).

[32] Y. I. Salamin and C. H. Keitel, "Analysis of electron acceleration in a vacuum beat wave," Journal of Physics B: Atomic, Molecular and Optical Physics **33**, 5057–5076 (2000).

[33] Y. I. Salamin and C. H. Keitel, "Subcycle high electron acceleration by crossed laser beams," Applied Physics Letters **77**, 1082–1084 (2000).

[34] S. X. Hu and A. F. Starace, "Gev electrons from Ultraintense Laser Interaction with Highly Charged Ions," Phys. Rev. Lett. **88**, 245003 (2002).

[35] Q. Kong, Y. K. Ho, J. X. Wang, P. X. Wang, L. Feng, and Z. S. Yuan, "Conditions for electron capture by an ultraintense stationary laser beam," Phys. Rev. E **61**, 1981–1984 (2000).

[36] T. Tajima and J. M. Dawson, "Laser electron accelerator," Phys. Rev. Lett. **43**, 267–270 (1979).

[37] H. Daido, M. Nishiuchi, and A. S. Pirozhkov, "Review of laser-driven ion sources and their applications," Reports on Progress in Physics **75**, 056401 (2012).

[38] R. A. Snavely, M. H. Key, S. P. Hatchett, T. E. Cowan, M. Roth, T. W. Phillips, M. A. Stoyer, E. A. Henry, T. C. Sangster, M. S. Singh, S. C. Wilks, A. MacKinnon, A. Offenberger, D. M. Pennington, K. Yasuike, A. B. Langdon, B. F. Lasinski, J. Johnson, M. D. Perry, and E. M. Campbell, "Intense High-Energy Proton Beams from Petawatt-Laser Irradiation of Solids," Phys. Rev. Lett. **85**, 2945–2948 (2000).

[39] M. Borghesi, J. Fuchs, S. V. Bulanov, A. J. MacKinnon, P. K. Patel, and M. Roth, "Fast Ion Generation by High-Intensity Laser Irradiation of Solid Targets and Applications," Fusion Science and Technology **49**, 412–439 (2006).

[40] A. Macchi, M. Borghesi, and M. Passoni, "Ion acceleration by superintense laser-plasma interaction," Rev. Mod. Phys. **85**, 751–793 (2013).

[41] J. M. Dawson, "Particle simulation of plasmas," Rev. Mod. Phys. **55**, 403–447 (1983).

[42] U. Linz and J. Alonso, "Laser-driven ion accelerators for tumor therapy revisited," Phys. Rev. Accel. Beams **19**, 124802 (2016).

[43] M. Borghesi, S. Kar, R. Prasad, F. K. Kakolee, K. Quinn, H. Ahmed, G. Sarri, B. Ramakrishna, B. Qiao, M. Geissler, S. Ter-Avetisyan, M. Zepf, G. Schettino, B. Stevens, M. Tolley, A. Ward, J. Green, P. S. Foster, C. Spindloe, A. Gallegos, P. Robinson, D. Neely, D. C. Carroll, O. Tresca, X. Yuan, M. Quinn, P. McKenna, N. Dover, C. Palmer, J. Schreiber, Z. Najmudin, I. Sari, M. Kraft, M. Merchant, J. C. Jeynes, K. Kirkby, F. Fiorini, D. Kirby, and S. Green, "Ion source development and radiobiology applications within the LIBRA project," (2011), vol. 8079, pp. 171 – 176.

[44] "Interstellar Vehicle Propelled by Terrestrial Laser Beam," Nature **211**, 22–23 (1966).

[45] "Lightsail," `https://www.planetary.org/sci-tech/lightsail`.

[46] "Breakthrough Starshot Initiative," `https://breakthroughinitiatives.org/initiative/3`.

[47] T. Esirkepov, M. Borghesi, S. V. Bulanov, G. Mourou, and T. Tajima, "Highly Efficient Relativistic-Ion Generation in the Laser-Piston Regime," Phys. Rev. Lett. **92**, 175003 (2004).

[48] T. V. Liseykina, M. Borghesi, A. Macchi, and S. Tuveri, "Radiation pressure acceleration by ultraintense laser pulses," Plasma Phys. Control. Fusion **50**, 124033 (2008).

[49] M. Tamburini, F. Pegoraro, A. D. Piazza, C. H. Keitel, and A. Macchi, "Radiation reaction effects on radiation pressure acceleration," New Journal of Physics **12**, 123005 (2010).

[50] M. Tamburini, T. V. Liseykina, F. Pegoraro, and A. Macchi, "Radiation-pressure-dominant acceleration: Polarization and radiation reaction effects and energy increase in three-dimensional simulations," Phys. Rev. E **85**, 016407 (2012).

[51] A. Macchi, S. Veghini, T. V. Liseykina, and F. Pegoraro, "Radiation pressure acceleration of ultrathin foils," New J. Phys. **12**, 045013 (2010).

[52] A. P. L. Robinson, M. Zepf, S. Kar, R. G. Evans, and C. Bellei, "Radiation pressure acceleration of thin foils with circularly polarized laser pulses," New J. Phys. **10**, 013021 (2008).

[53] O. Klimo, J. Psikal, J. Limpouch, and V. T. Tikhonchuk, "Monoenergetic ion beams from ultrathin foils irradiated by ultrahigh-contrast circularly polarized laser pulses," Phys. Rev. ST Accel. Beams **11**, 031301 (2008).

[54] E. Ott, "Nonlinear Evolution of the Rayleigh-Taylor Instability of a Thin Layer," Phys. Rev. Lett. **29**, 1429–1432 (1972).

[55] F. Pegoraro and S. V. Bulanov, "Photon Bubbles and Ion Acceleration in a Plasma Dominated by the Radiation Pressure of an Electromagnetic Pulse," Phys. Rev. Lett. **99**, 065002 (2007).

[56] C. A. J. Palmer, J. Schreiber, S. R. Nagel, N. P. Dover, C. Bellei, F. N. Beg, S. Bott, R. J. Clarke, A. E. Dangor, S. M. Hassan, P. Hilz, D. Jung, S. Kneip, S. P. D. Mangles, K. L. Lancaster, A. Rehman, A. P. L. Robinson, C. Spindloe, J. Szerypo, M. Tatarakis, M. Yeung, M. Zepf, and Z. Najmudin, "Rayleigh-Taylor Instability of an Ultrathin Foil Accelerated by the Radiation Pressure of an Intense Laser," Phys. Rev. Lett. **108**, 225002 (2012).

[57] B. Eliasson, "Instability of a thin conducting foil accelerated by a finite wavelength intense laser," New Journal of Physics **17**, 033026 (2015).

[58] A. Sgattoni, S. Sinigardi, L. Fedeli, F. Pegoraro, and A. Macchi, "Laser-driven Rayleigh-Taylor instability: Plasmonic effects and three-dimensional structures," Phys. Rev. E **91**, 013106 (2015).

[59] M. Tamburini, A. Di Piazza, T. V. Liseykina, and C. H. Keitel, "Plasma-Based Generation and Control of a Single Few-Cycle High-Energy Ultrahigh-Intensity Laser Pulse," Phys. Rev. Lett. **113**, 025005 (2014).

[60] S. S. Bulanov, A. Brantov, V. Y. Bychenkov, V. Chvykov, G. Kalinchenko, T. Matsuoka, P. Rousseau, S. Reed, V. Yanovsky, D. W. Litzenberg, K. Krushelnick, and

A. Maksimchuk, "Accelerating monoenergetic protons from ultrathin foils by flat-top laser pulses in the directed-coulomb-explosion regime," Phys. Rev. E **78**, 026412 (2008).

[61] M. Chen, A. Pukhov, T. P. Yu, and Z. M. Sheng, "Enhanced Collimated GeV Monoenergetic Ion Acceleration from a Shaped Foil Target Irradiated by a Circularly Polarized Laser Pulse," Phys. Rev. Lett. **103**, 024801 (2009).

[62] S. V. Bulanov, T. Esirkepov, P. Migliozzi, F. Pegoraro, T. Tajima, and F. Terranova, "Neutrino oscillation studies with laser-driven beam dump facilities," Nucl. Inst. Meth. Phys. Res. A **540**, 25–41 (2005).

[63] S. Kar, K. F. Kakolee, B. Qiao, A. Macchi, M. Cerchez, D. Doria, M. Geissler, P. McKenna, D. Neely, J. Osterholz, R. Prasad, K. Quinn, B. Ramakrishna, G. Sarri, O. Willi, X. Y. Yuan, M. Zepf, and M. Borghesi, "Ion Acceleration in Multispecies Targets Driven by Intense Laser Radiation Pressure," Phys. Rev. Lett. **109**, 185006 (2012).

[64] S. Steinke, P. Hilz, M. Schnürer, G. Priebe, J. Bränzel, F. Abicht, D. Kiefer, C. Kreuzer, T. Ostermayr, J. Schreiber, A. A. Andreev, T. P. Yu, A. Pukhov, and W. Sandner, "Stable laser-ion acceleration in the light sail regime," Phys. Rev. ST Accel. Beams **16**, 011303 (2013).

[65] Z. M. Zhang, X. T. He, Z. M. Sheng, and M. Y. Yu, "High-energy monoenergetic protons from multistaged acceleration of thin double-layer target by circularly polarized laser," Physics of Plasmas **18**, 023110 (2011).

[66] X. F. Shen, B. Qiao, H. X. Chang, W. L. Zhang, H. Zhang, C. T. Zhou, and X. T. He, "Maintaining stable radiation pressure acceleration of ion beams via cascaded electron replenishment," New J. Phys. **19**, 033034 (2017).

[67] M. Chen, N. Kumar, A. Pukhov, and T.-P. Yu, "Stabilized radiation pressure dominated ion acceleration from surface modulated thin-foil targets," Phys. Plasmas **18**, 073106 (2011).

[68] L. Masse, "Stabilizing Effect of Anisotropic Thermal Diffusion on the Ablative Rayleigh-Taylor Instability," Phys. Rev. Lett. **98**, 245001 (2007).

[69] Y. Wan, C. H. Pai, C. J. Zhang, F. Li, Y. P. Wu, J. F. Hua, W. Lu, C. Joshi, W. B. Mori, and V. Malka, "Physical mechanism of the electron-ion coupled transverse instability in laser pressure ion acceleration for different regimes," Phys. Rev. E **98**, 013202 (2018).

[70] "Smilei," `http://www.maisondelasimulation.fr/smilei/` (2014).

[71] J. Derouillat, A. Beck, F. Pérez, T. Vinci, M. Chiaramello, A. Grassi, M. Flé, G. Bouchard, I. Plotnikov, N. Aunai, J. Dargent, C. Riconda, and M. Grech, "Smilei : A collaborative, open-source, multi-purpose particle-in-cell code for plasma simulation," Computer Physics Communications **222**, 351 – 373 (2018).

[72] J. Kepler, *Ad Vitellionem Paralipomena, Quibus Astronomiae Pars Optica Traditur* (C. Marnius & heirs of J. Aubrius, Frankfurt/M., 1604).

[73] A. M. Smith, "Johannes Kepler, Optics. Paralipomena to Witelo & Optical Part of Astronomy. English Translation by William H. Donahue. Sante Fe: Green Lion Press, 2000." British Journal for the History of Science **35**, 213–250 (2002).

[74] S. P. Thompson, *Treatise on Light in which are explained the cause of that which occurs in reflection, & in refraction. And particularly in the strange refraction of Iceland crystal.* (University of Chicago Press, Chicago, Macmillan, London, 1912).

[75] K. Schaposchnikow, "Über Zusammenstöße von Lichtquanten," Zeitschrift für Physik **33**, 706–709 (1925).

[76] L. Rosenfeld and E. E. Witmer, "Über die Hohlraumstrahlung und die Lichtquantenhypothese," Zeitschrift für Physik **47**, 517–521 (1928).

[77] O. Halpern, "Scattering Processes Produced by Electrons in Negative Energy States," Phys. Rev. **44**, 855–856 (1933).

[78] P. A. M. Dirac and R. H. Fowler, "The quantum theory of the electron," Proceedings of the Royal Society of London. Series A, Containing Papers of a Mathematical and Physical Character **117**, 610–624 (1928).

[79] H. Euler and B. Kockel, "Über die Streuung von Licht an Licht nach der Diracschen Theorie," Naturwissenschaften **23**, 246–247 (1935).

[80] H. Euler, "Über die Streuung von Licht an Licht nach der Diracschen Theorie," Annalen der Physik **418**, 398–448 (1936).

[81] A. Achieser, "Über die Streuung von Licht an Licht," Phys. Z. Sowjetunion **11**, 263–283 (1937).

[82] R. Karplus and M. Neuman, "Non-Linear Interactions between Electromagnetic Fields," Phys. Rev. **80**, 380–385 (1950).

[83] R. Karplus and M. Neuman, "The Scattering of Light by Light," Phys. Rev. **83**, 776–784 (1951).

[84] B. De Tollis, "Dispersive approach to photon-photon scattering," Il Nuovo Cimento (1955-1965) **32**, 757–768 (1964).

[85] B. De Tollis, "The scattering of photons by photons," Il Nuovo Cimento (1955-1965) **35**, 1182–1193 (1965).

[86] V. B. Berestetskii, E. M. Lifshitz, and L. P. Pitaevskii, *Quantum Electrodynamics*, vol. 4 (Butterworth-Heinemann, 1982), 2nd ed.

[87] K. Scharnhorst, "Photon-photon scattering and related phenomena. Experimental and theoretical approaches: The early period," (2019).

[88] S. I. Vavilov, "Remarks on the empirical accuracy of the optical superposition principle [engl. transl. of zh. russk. fiz.-khim. obshch., ch. fiz. 60(1928)555]," (2017).

[89] A. K. Das, "On Collisions of Photons," Phys. Rev. **37**, 94–95 (1931).

[90] C. C. Farr and C. J. Banwell, "Velocity of propagation of light in vacuo in a transverse magnetic field," Proceedings of the Royal Society of London. Series A, Containing Papers of a Mathematical and Physical Character **137**, 275–282 (1932).

[91] V. I. Ritus, "Quantum effects of the interaction of elementary particles with an intense electromagnetic field," Journal of Soviet Laser Research **6**, 497–617 (1985).

[92] G. Jikia and A. Tkabladze, "Photon-photon scattering at the photon linear collider," Physics Letters B **323**, 453 – 458 (1994).

[93] K. O. Mikaelian, "Detection of elastic light-by-light scattering at SLAC," Physics Letters B **115**, 267 – 269 (1982).

[94] E. Lundström, G. Brodin, J. Lundin, M. Marklund, R. Bingham, J. Collier, J. T. Mendonça, and P. Norreys, "Using High-Power Lasers for Detection of Elastic Photon-Photon Scattering," Phys. Rev. Lett. **96**, 083602 (2006).

[95] J. Lundin, L. Stenflo, G. Brodin, M. Marklund, and P. K. Shukla, "Circularly polarized waves in a plasma with vacuum polarization effects," Physics of Plasmas **14**, 064503 (2007).

[96] B. King, A. Di Piazza, and C. H. Keitel, "A matterless double slit," Nature Photonics **4**, 92–94 (2010).

[97] G. Y. Kryuchkyan and K. Z. Hatsagortsyan, "Bragg Scattering of Light in Vacuum Structured by Strong Periodic Fields," Phys. Rev. Lett. **107**, 053604 (2011).

[98] T. Heinzl, B. Liesfeld, K.-U. Amthor, H. Schwoerer, R. Sauerbrey, and A. Wipf, "On the observation of vacuum birefringence," Optics Communications **267**, 318 – 321 (2006).

[99] B. King, A. Di Piazza, and C. H. Keitel, "Double-slit vacuum polarization effects in ultraintense laser fields," Phys. Rev. A **82**, 032114 (2010).

[100] S. Bragin, S. Meuren, C. H. Keitel, and A. Di Piazza, "High-Energy Vacuum Birefringence and Dichroism in an Ultrastrong Laser Field," Phys. Rev. Lett. **119**, 250403 (2017).

[101] A. Di Piazza, K. Z. Hatsagortsyan, and C. H. Keitel, "Enhancement of vacuum polarization effects in a plasma," Physics of Plasmas **14**, 032102 (2007).

[102] T. Inada, T. Yamaji, S. Adachi, T. Namba, S. Asai, T. Kobayashi, K. Tamasaku, Y. Tanaka, Y. Inubushi, K. Sawada, M. Yabashi, and T. Ishikawa, "Search for photon-photon elastic scattering in the X-ray region," Physics Letters B **732**, 356 – 359 (2014).

[103] T. Yamaji, T. Inada, T. Yamazaki, T. Namba, S. Asai, T. Kobayashi, K. Tamasaku, Y. Tanaka, Y. Inubushi, K. Sawada, M. Yabashi, and T. Ishikawa, "An experiment of X-ray photon-photon elastic scattering with a Laue-case beam collider," Physics Letters B **763**, 454 – 457 (2016).

[104] T. Takahashi, G. An, Y. Chen, W. Chou, Y. Huang, W. Liu, W. Lu, J. Lv, G. Pei, S. Pei, C. P. Shen, B. Sun, and C. Zhang, "Light-by-light scattering in a photon-photon collider," The European Physical Journal C **78**, 893 (2018).

[105] M. Marklund and P. K. Shukla, "Nonlinear collective effects in photon-photon and photon-plasma interactions," Rev. Mod. Phys. **78**, 591–640 (2006).

[106] A. Di Piazza, C. Müller, K. Z. Hatsagortsyan, and C. H. Keitel, "Extremely high-intensity laser interactions with fundamental quantum systems," Rev. Mod. Phys. **84**, 1177–1228 (2012).

[107] R. R. Wilson, "Scattering of 1.3^3 MeV Gamma-Rays by an Electric Field," Phys. Rev. **90**, 720–721 (1953).

[108] M. Schumacher, I. Borchert, F. Smend, and P. Rullhusen, "Delbrück scattering of 2.75 MeV photons by lead," Physics Letters B **59**, 134 – 136 (1975).

[109] S. Z. Akhmadaliev, G. Y. Kezerashvili, S. G. Klimenko, V. M. Malyshev, A. L. Maslennikov, A. M. Milov, A. I. Milstein, N. Y. Muchnoi, A. I. Naumenkov, V. S. Panin, S. V. Peleganchuk, V. G. Popov, G. E. Pospelov, I. Y. Protopopov, L. V. Romanov, A. G. Shamov, D. N. Shatilov, E. A. Simonov, and Y. A. Tikhonov, "Delbrück scattering at energies of 140-450 MeV," Phys. Rev. C **58**, 2844–2850 (1998).

[110] S. Z. Akhmadaliev, G. Y. Kezerashvili, S. G. Klimenko, R. N. Lee, V. M. Malyshev, A. L. Maslennikov, A. M. Milov, A. I. Milstein, N. Y. Muchnoi, A. I. Naumenkov, V. S. Panin, S. V. Peleganchuk, G. E. Pospelov, I. Y. Protopopov, L. V. Romanov, A. G. Shamov, D. N. Shatilov, E. A. Simonov, V. M. Strakhovenko, and Y. A. Tikhonov, "Experimental Investigation of High-Energy Photon Splitting in Atomic Fields," Phys. Rev. Lett. **89**, 061802 (2002).

[111] R. Lee, A. Maslennikov, A. Milstein, V. Strakhovenko, and Y. Tikhonov, "Photon splitting in atomic fields," Physics Reports **373**, 213 – 246 (2003).

[112] D. d'Enterria and G. G. da Silveira, "Observing Light-by-Light Scattering at the Large Hadron Collider," Phys. Rev. Lett. **111**, 080405 (2013).

[113] G. Aaboud, M.and Aad, B. *et al.* Abbott, and A. T. L. A. S. Collaboration, "Evidence for light-by-light scattering in heavy-ion collisions with the ATLAS detector at the LHC," Nature Physics **13**, 852–858 (2017).

[114] A. Collaboration, "Measurement of light-by-light scattering and search for axion-like particles with 2.2 nb^{-1} of Pb+Pb data with the ATLAS detector," (2020).

[115] G. Breit and J. A. Wheeler, "Collision of Two Light Quanta," Phys. Rev. **46**, 1087–1091 (1934).

[116] D. L. Burke, R. C. Field, G. Horton-Smith, J. E. Spencer, D. Walz, S. C. Berridge, W. M. Bugg, K. Shmakov, A. W. Weidemann, C. Bula, K. T. McDonald, E. J. Prebys, C. Bamber, S. J. Boege, T. Koffas, T. Kotseroglou, A. C. Melissinos, D. D. Meyerhofer, D. A. Reis, and W. Ragg, "Positron Production in Multiphoton Light-by-Light Scattering," Phys. Rev. Lett. **79**, 1626–1629 (1997).

[117] C. Bamber, S. J. Boege, T. Koffas, T. Kotseroglou, A. C. Melissinos, D. D. Meyerhofer, D. A. Reis, W. Ragg, C. Bula, K. T. McDonald, E. J. Prebys, D. L. Burke, R. C. Field, G. Horton-Smith, J. E. Spencer, D. Walz, S. C. Berridge, W. M. Bugg, K. Shmakov, and A. W. Weidemann, "Studies of nonlinear QED in collisions of 46.6 GeV electrons with intense laser pulses," Phys. Rev. D **60**, 092004 (1999).

[118] O. J. Pike, F. Mackenroth, E. G. Hill, and S. J. Rose, "A photon-photon collider in a vacuum hohlraum," Nature Photonics **8**, 434–436 (2014).

[119] X. Ribeyre, E. d'Humières, O. Jansen, S. Jequier, V. T. Tikhonchuk, and M. Lobet, "Pair creation in collision of γ-ray beams produced with high-intensity lasers," Phys. Rev. E **93**, 013201 (2016).

[120] D. H. Bilderback, P. Elleaume, and E. Weckert, "Review of third and next generation synchrotron light sources," Journal of Physics B: Atomic, Molecular and Optical Physics **38**, S773–S797 (2005).

[121] S. Corde, K. Ta Phuoc, G. Lambert, R. Fitour, V. Malka, A. Rousse, A. Beck, and E. Lefebvre, "Femtosecond x rays from laser-plasma accelerators," Rev. Mod. Phys. **85**, 1–48 (2013).

[122] T. G. Blackburn, "Radiation reaction in electron-beam interactions with high-intensity lasers," Reviews of Modern Plasma Physics **4**, 5 (2020).

[123] `https://lightsources.org/lightsources-of-the-world/`.

[124] C. P. Ridgers, C. S. Brady, R. Duclous, J. G. Kirk, K. Bennett, T. D. Arber, A. P. L. Robinson, and A. R. Bell, "Dense Electron-Positron Plasmas and Ultraintense γ rays from Laser-Irradiated Solids," Phys. Rev. Lett. **108**, 165006 (2012).

[125] D. J. Stark, T. Toncian, and A. V. Arefiev, "Enhanced Multi-MeV Photon Emission by a Laser-Driven Electron Beam in a Self-Generated Magnetic Field," Phys. Rev. Lett. **116**, 185003 (2016).

[126] T. W. Huang, C. M. Kim, C. T. Zhou, C. M. Ryu, K. Nakajima, S. C. Ruan, and C. H. Nam, "Tabletop laser-driven gamma-ray source with nanostructured double-layer target," Plasma Physics and Controlled Fusion **60**, 115006 (2018).

[127] T. W. Huang, C. M. Kim, C. T. Zhou, M. H. Cho, K. Nakajima, C. M. Ryu, S. C. Ruan, and C. H. Nam, "Highly efficient laser-driven Compton gamma-ray source," New Journal of Physics **21**, 013008 (2019).

[128] W.-M. Wang, Z.-M. Sheng, P. Gibbon, L.-M. Chen, Y.-T. Li, and J. Zhang, "Collimated ultrabright gamma rays from electron wiggling along a petawatt laser-irradiated wire in the QED regime," Proceedings of the National Academy of Sciences **115**, 9911–9916 (2018).

[129] M. Jirka, O. Klimo, Y.-J. Gu, and S. Weber, "Enhanced photon emission from a double-layer target at moderate laser intensities," Scientific Reports **10**, 8887 (2020).

[130] J.-X. Li, K. Z. Hatsagortsyan, B. J. Galow, and C. H. Keitel, "Attosecond Gamma-ray Pulses via Nonlinear Compton Scattering in the Radiation-Dominated Regime," Phys. Rev. Lett. **115**, 204801 (2015).

[131] M. Vranic, T. Grismayer, S. Meuren, R. A. Fonseca, and L. O. Silva, "Are we ready to transfer optical light to gamma-rays?" Physics of Plasmas **26**, 053103 (2019).

[132] L. L. Ji, A. Pukhov, E. N. Nerush, I. Y. Kostyukov, B. F. Shen, and K. U. Akli, "Energy partition, γ-ray emission, and radiation reaction in the near-quantum electrodynamical regime of laser-plasma interaction," Physics of Plasmas **21**, 023109 (2014).

[133] M. Jirka, O. Klimo, S. V. Bulanov, T. Z. Esirkepov, E. Gelfer, S. S. Bulanov, S. Weber, and G. Korn, "Electron dynamics and γ and e^-e^+ production by colliding laser pulses," Phys. Rev. E **93**, 023207 (2016).

[134] M. Tamburini, A. Di Piazza, and C. H. Keitel, "Laser-pulse-shape control of seeded QED cascades," Scientific Reports **7**, 5694 (2017).

[135] A. Benedetti, M. Tamburini, and C. H. Keitel, "Giant collimated gamma-ray flashes," Nature Photonics **12**, 319–323 (2018).

[136] F. Del Gaudio, T. Grismayer, R. A. Fonseca, W. B. Mori, and L. O. Silva, "Bright γ rays source and nonlinear Breit-Wheeler pairs in the collision of high density particle beams," Phys. Rev. Accel. Beams **22**, 023402 (2019).

[137] V. Yakimenko, S. Meuren, F. Del Gaudio, C. Baumann, A. Fedotov, F. Fiuza, T. Grismayer, M. J. Hogan, A. Pukhov, L. O. Silva, and G. White, "Prospect of Studying Nonperturbative QED with Beam-Beam Collisions," Phys. Rev. Lett. **122**, 190404 (2019).

[138] M. Tamburini and S. Meuren, "Efficient High-Energy Photon Production in the Supercritical QED Regime," (2020).

[139] A. Sampath, X. Davoine, S. Corde, L. Gremillet, M. Sangal, C. H. Keitel, R. Ariniello, J. Cary, H. Ekerfelt, C. Emma, F. Fiuza, H. Fujii, M. Gilljohann, M. Hogan, C. Joshi, A. Knetsch, O. Kononenko, V. Lee, M. Litos, K. Marsh, Z. Nie, B. O'Shea, J. R. Peterson, P. S. M. Claveria, D. Storey, Y. Wu, X. Xu, C. Zhang, and M. Tamburini, "Extremely Dense Gamma-Ray Pulses in Electron Beam-Multifoil Collisions," (2020).

[140] U. Stamm, "Extreme ultraviolet light sources: State of the art, future developments, and potential applications," (2003).

[141] F. Ferrari, F. Calegari, M. Lucchini, C. Vozzi, S. Stagira, G. Sansone, and M. Nisoli, "High-energy isolated attosecond pulses generated by above-saturation few-cycle fields," Nature Photonics **4**, 875–879 (2010).

[142] A. Ozawa, Z. Zhao, M. Kuwata-Gonokami, and Y. Kobayashi, "High average power coherent vuv generation at 10 mhz repetition frequency by intracavity high harmonic generation," Opt. Express **23**, 15107–15118 (2015).

[143] C. M. Heyl, C. L. Arnold, A. Couairon, and A. L'Huillier, "Introduction to macroscopic power scaling principles for high-order harmonic generation," Journal of Physics B: Atomic, Molecular and Optical Physics **50**, 013001 (2016).

[144] C. M. Heyl, H. Coudert-Alteirac, M. Miranda, M. Louisy, K. Kovacs, V. Tosa, E. Balogh, K. Varjú, A. L'Huillier, A. Couairon, and C. L. Arnold, "Scale-invariant nonlinear optics in gases," Optica **3**, 75–81 (2016).

[145] A. Nayak, I. Orfanos, I. Makos, M. Dumergue, S. Kühn, E. Skantzakis, B. Bodi, K. Varju, C. Kalpouzos, H. I. B. Banks, A. Emmanouilidou, D. Charalambidis, and P. Tzallas, "Multiple ionization of argon via multi-XUV-photon absorption induced by 20-GW high-order harmonic laser pulses," Phys. Rev. A **98**, 023426 (2018).

[146] B. Senfftleben, M. Kretschmar, A. Hoffmann, M. Sauppe, J. TÃ$\frac{1}{4}$mmler, I. Will, T. Nagy, M. J. J. Vrakking, D. Rupp, and B. SchÃ$\frac{1}{4}$tte, "Highly non-linear ionization of atoms induced by intense high-harmonic pulses," Journal of Physics: Photonics **2**, 034001 (2020).

[147] S. Haessler, F. Böhle, M. Bocoum, M. Ouillé, J. Kaur, D. Levy, L. Daniault, A. Vernier, J. Faure, and R. Lopez-Martens, "Relativistic high-harmonic generation and correlated electron acceleration from plasma mirrors at 1 kHz repetition rate," (2020).

[148] V. Yakimenko, L. Alsberg, E. Bong, G. Bouchard, C. Clarke, C. Emma, S. Green, C. Hast, M. J. Hogan, J. Seabury, N. Lipkowitz, B. O'Shea, D. Storey, G. White, and G. Yocky, "FACET-II facility for advanced accelerator experimental tests," Phys. Rev. Accel. Beams **22**, 101301 (2019).

[149] "Deutsches elektronen-synchrotron (desy)„" `https://photon-science.desy.de/facilities`.

[150] Y. I. Salamin, G. R. Mocken, and C. H. Keitel, "Electron scattering and acceleration by a tightly focused laser beam," Phys. Rev. ST Accel. Beams **5**, 101301 (2002).

[151] Y. I. Salamin, "Fields of a Gaussian beam beyond the paraxial approximation," Applied Physics B **86**, 319 (2006).

[152] K. T. McDonald, "Gaussian Laser Beams and Particle Acceleration," (1995).

[153] M. Sangal and M. Tamburini, "High-Energy and High-Quality Ion beams in Light Sail Acceleration," (2020).

[154] F. F. Chen, *Introduction to Plasma Physics and Controlled Fusion* (Springer, 2016).

[155] J. Callen, *Fundamental Processes in Plasmas.*

[156] P. Gibbon, "Physics of high-intensity laser-plasma interactions," La Rivista del Nuovo Cimento **35**, 607–644 (2012).

[157] A. Pukhov, "Particle-In-Cell Codes for Plasma-based Particle Acceleration," Vol. 1: Proceedings of the 2014 CAS-CERN Accelerator School: Plasma Wake Acceleration (2016).

[158] Kane Yee, "Numerical solution of initial boundary value problems involving Maxwell's equations in isotropic media," IEEE Transactions on Antennas and Propagation **14**, 302–307 (1966).

[159] J. P. Boris, "Relativistic plasma simulation-optimization of a hybrid code," Proc. 4th Conf. Num. Sim. Plasmas pp. 3–67 (1970).

[160] J. Maxwell, *A Treatise on electricity and magnetism*, vol. 2 (Macmillan, London).

[161] A. Macchi and C. Benedetti, "Ion acceleration by radiation pressure in thin and thick targets," Nuclear Instruments and Methods in Physics Research Section A: Accelerators, Spectrometers, Detectors and Associated Equipment **620**, 41 – 45 (2010). COULOMB09.

[162] A. P. L. Robinson, P. Gibbon, M. Zepf, S. Kar, R. G. Evans, and C. Bellei, "Relativistically correct hole-boring and ion acceleration by circularly polarized laser pulses," Plasma Physics and Controlled Fusion **51**, 024004 (2009).

[163] A. Macchi, F. Cattani, T. V. Liseykina, and F. Cornolti, "Laser Acceleration of Ion Bunches at the Front Surface of Overdense Plasmas," Phys. Rev. Lett. **94**, 165003 (2005).

[164] A. Macchi, S. Veghini, and F. Pegoraro, ""Light Sail" Acceleration Reexamined," Phys. Rev. Lett. **103**, 085003 (2009).

[165] X. Zhang, B. Shen, L. Ji, W. Wang, J. Xu, Y. Yu, and X. Wang, "Instabilities in interaction of circularly polarized laser pulse and overdense target," Phys. Plasmas **18**, 073101 (2011).

[166] Y. Wan, C. Pai, C. J. Zhang, F. Li, Y. P. Wu, J. F. Hua, W. Lu, Y. Q. Gu, L. O. Silva, C. Joshi, and W. B. Mori, "Physical Mechanism of the Transverse Instability in Radiation Pressure Ion Acceleration," Phys. Rev. Lett. **117**, 234801 (2016).

[167] V. Khudik, S. A. Yi, C. Siemon, and G. Shvets, "The analytic model of a laser-accelerated plasma target and its stability," Physics of Plasmas **21**, 013110 (2014).

[168] M. Grech, S. Skupin, A. Diaw, T. Schlegel, and V. T. Tikhonchuk, "Energy dispersion in radiation pressure accelerated ion beams," New J. Phys. **13**, 123003 (2011).

[169] K. Markey, P. McKenna, C. M. Brenner, D. C. Carroll, M. M. Günther, K. Harres, S. Kar, K. Lancaster, F. Nürnberg, M. N. Quinn, A. P. L. Robinson, M. Roth, M. Zepf, and D. Neely, "Spectral Enhancement in the Double Pulse Regime of Laser Proton Acceleration," Phys. Rev. Lett. **105**, 195008 (2010).

[170] M. Chen, A. Pukhov, T.-P. Yu, and Z.-M. Sheng, "Radiation reaction effects on ion acceleration in laser foil interaction," Plasma Physics and Controlled Fusion **53**, 014004 (2010).

[171] M. Chen, A. Pukhov, Z. M. Sheng, and X. Q. Yan, "Laser mode effects on the ion acceleration during circularly polarized laser pulse interaction with foil targets," Phys. Plasmas **15**, 113103 (2008).

[172] N. Naumova, T. Schlegel, V. T. Tikhonchuk, C. Labaune, I. V. Sokolov, and G. Mourou, "Hole boring in a DT Pellet and Fast-Ion Ignition with Ultraintense Laser Pulses," Phys. Rev. Lett. **102**, 025002 (2009).

[173] T.-P. Yu, A. Pukhov, G. Shvets, and M. Chen, "Stable Laser-Driven Proton Beam Acceleration from a Two-Ion-Species Ultrathin Foil," Phys. Rev. Lett. **105**, 065002 (2010).

[174] C. Thaury, F. Quéré, J.-P. Geindre, A. Levy, T. Ceccotti, P. Monot, M. Bougeard, F. Réau, P. d'Oliveira, P. Audebert *et al.*, "Plasma mirrors for ultrahigh-intensity optics," Nature Physics **3**, 424–429 (2007).

[175] J. Braenzel, A. A. Andreev, K. Platonov, M. Klingsporn, L. Ehrentraut, W. Sandner, and M. Schnürer, "Coulomb-Driven Energy Boost of Heavy Ions for Laser-Plasma Acceleration," Phys. Rev. Lett. **114**, 124801 (2015).

[176] D. Neely, P. Foster, A. Robinson, F. Lindau, O. Lundh, A. Persson, C.-G. Wahlström, and P. McKenna, "Enhanced proton beams from ultrathin targets driven by high contrast laser pulses," Appl. Phys. Lett. **89**, 021502 (2006).

[177] T. Ceccotti, A. Lévy, H. Popescu, F. Réau, P. D'Oliveira, P. Monot, J. P. Geindre, E. Lefebvre, and P. Martin, "Proton Acceleration with High-Intensity Ultrahigh-Contrast Laser Pulses," Phys. Rev. Lett. **99**, 185002 (2007).

[178] F. Wagner, S. Bedacht, A. Ortner, M. Roth, A. Tauschwitz, B. Zielbauer, and V. Bagnoud, "Pre-plasma formation in experiments using petawatt lasers," Opt. Express **22**, 29505–29514 (2014).

[179] P. Varmazyar, S. Mirzanejhad, and T. Mohsenpour, "Effect of pre-plasma on the ion acceleration by intense ultra-short laser pulses," Laser and Particle Beams **36**, 226–231 (2018).

[180] A. Henig, S. Steinke, M. Schnürer, T. Sokollik, R. Hörlein, D. Kiefer, D. Jung, J. Schreiber, B. M. Hegelich, X. Q. Yan, J. Meyer-ter Vehn, T. Tajima, P. V. Nickles, W. Sandner, and D. Habs, "Radiation-Pressure Acceleration of Ion Beams Driven by Circularly Polarized Laser Pulses," Phys. Rev. Lett. **103**, 245003 (2009).

[181] A. Sgattoni, S. Sinigardi, and A. Macchi, "High energy gain in three-dimensional simulations of light sail acceleration," Applied Physics Letters **105**, 084105 (2014).

[182] A. Macchi, T. V. Liseikina, S. Tuveri, and S. Veghini, "Theory and simulation of ion acceleration with circularly polarized laser pulses," Comptes Rendus Physique **10**, 207 – 215 (2009). Laser acceleration of particles in plasma.

[183] S. I. Abarzhi, "Nonlinear three-dimensional Rayleigh-Taylor instability," Phys. Rev. E **59**, 1729–1735 (1999).

[184] S. I. Abarzhi, "Review of nonlinear dynamics of the unstable fluid interface: conservation laws and group theory," Physica Scripta **T132**, 014012 (2008).

[185] S. Sinigardi, G. Turchetti, P. Londrillo, F. Rossi, D. Giove, C. De Martinis, and M. Sumini, "Transport and energy selection of laser generated protons for postacceleration with a compact linac," Phys. Rev. ST Accel. Beams **16**, 031301 (2013).

[186] L. D. Landau and E. M. Lifshitz, *The Classical Theory of Fields*, vol. 2 (Butterworth-Heinemann), 4th ed.

[187] V. N. Baier, V. M. Katkov, and V. M. Strakhovenko, *Electromagnetic Processes at High Energies in Oriented Single Crystals* (World Scientific, Singapore„ 1998).

[188] T. G. Blackburn, D. Seipt, S. S. Bulanov, and M. Marklund, "Radiation beaming in the quantum regime," Phys. Rev. A **101**, 012505 (2020).

[189] J. D. Jackson, *Classical Electrodynamics*, vol. 2 (John Wiley & Sons, 1998), 3rd ed.

Acknowledgements

This work would probably not have come to fruition had it not been for some integral beings in my life. First and foremost, I would like to dedicate my thesis to my mother Mrs. Deepa Sangal and my father Sr. Advocate Bharat Sangal, who have always supported me through thick and thin, and did not let any stone unturned in doing so all the way from my home in India, during the course of my stay here in Heidelberg, Germany. I cannot thank them enough for their love and support. I express my heartfelt gratitude to my partner, my beloved, Vivekanandhan Viswanathan, who besides providing me with utmost emotional support, also played the role of my mentor. Himself being a neuroscientist, and a perfectionist, he played an important part towards improving my reasoning skills and made me a better thinker. Moreover, Dr. Archana Sampath, my closest friend and colleague at MPIK made this journey filled with moments of joy and laughter, besides being always there in times of need. I am fortunate to have met her and worked with her. Dr. Mrityunjay Kundu, at the Institute for Plasma Research in Gujarat, India, under whose supervision I did my Masters' thesis project, has been the key reason behind motivating me to pursue further research. I thank him for his guidance. Dr. Harish Charan also deserves a special mention, who went out of his way to help me arrive on this path.

I would like to express my deepest thanks to my supervisor Prof. Christoph H. Keitel for providing me with the opportunity to work under his supervision. I am grateful to Dr. Matteo Tamburini, who guided me significantly through the past years towards the completion of this dissertation. Moreover, I thank all the administrative staff at the Max Planck Institute of Nuclear Physics (MPIK) for making our working conditions comfortable.

I also take this opportunity to thank Prof. Jan M. Pawlowski for having agreed to be the referee for my dissertation. I am thankful also to Dr. Robert Moshammer and Prof. Werner Aeschbach for having consented to being part of my doctoral examination committee.

My friends and colleagues at MPIK have served as sources of support and inspiration all throughout. A special mention to all my present office colleagues and those who had been at some point in the past. Dr. Sergei Kobzak, Daniel Bakucz Canário, Dr. Halil Cakir, Dr. Sergey Bragin have stood by me through these trying times, for which I am

extremely thankful. Dr. Ujjwal Sinha, who always saw the best in me, served as a pillar of support and encouragement throughout. I thank him for his teachings and advice. Besides, I also thank all my other colleagues and friends Dr. Shikha Bhadoria, Dr. Suo Tang, Dr. Yue-Yue Chen, Kamil Dzikowski for having made my experience at MPIK a memorable one.

Finally, I thank all my friends back in India, specially Devyani Agrawal, Prapti Devliyal, Mohit Gurnani, Piyush Kumar, Raja Raam, Harsh Srivastava and Prabhat Singh Negi for their friendship, love and support. I also thank my teachers in India, with a special gratitude to Dr. T.D. Senguttuvan and Smt. Mala Murali.

Lastly, I once again thank my parents, and take this opportunity to thank my soon to be new family, Mr. G. Viswanathan Iyer and Mrs. Suganya Viswanathan, and Dr. Annapoorani Viswanathan. Everyone that I mentioned, and probably forgot to mention, played a significant part in helping me through this difficult, yet fruitful, journey.